



HAL
open science

Etude numérique des propriétés optiques de nanostructures uniques et périodiques : des nano-antennes aux méta-matériaux à transmission

Tahseen Al-Aridhee

► **To cite this version:**

Tahseen Al-Aridhee. Etude numérique des propriétés optiques de nanostructures uniques et périodiques : des nano- antennes aux méta-matériaux à transmission. Optics / Photonic. Université de Franche-Comté, 2016. English. NNT : 2016BESA2004 . tel-01383487

HAL Id: tel-01383487

<https://theses.hal.science/tel-01383487>

Submitted on 18 Oct 2016

HAL is a multi-disciplinary open access archive for the deposit and dissemination of scientific research documents, whether they are published or not. The documents may come from teaching and research institutions in France or abroad, or from public or private research centers.

L'archive ouverte pluridisciplinaire **HAL**, est destinée au dépôt et à la diffusion de documents scientifiques de niveau recherche, publiés ou non, émanant des établissements d'enseignement et de recherche français ou étrangers, des laboratoires publics ou privés.

SPIM

Thèse de Doctorat

UFC

école doctorale sciences pour l'ingénieur et microtechniques
UNIVERSITÉ DE FRANCHE-COMTÉ

Numerical study of optical
properties of single and periodic
nanostructures: From nanoantenna
to enhanced transmission
metamaterials

■ TAHSEEN ALARIDHEE

SPIM

Thèse de Doctorat

UFC

école doctorale sciences pour l'ingénieur et microtechniques
UNIVERSITÉ DE FRANCHE-COMTÉ

THÈSE présentée par

TAHSEEN ALARIDHEE

pour obtenir le

Grade de Docteur de

l'Université de Franche-Comté

Spécialité : **Photonics optics**

Numerical study of optical properties of single and periodic nanostructures: From nanoantenna to enhanced transmission metamaterials

Soutenu le 16 June 2016 devant le Jury :

FABRICE DEVAUX	Président du jury	Professeur, UFC, Besançon
OMAR LAMROUS	Rapporteur	Professeur, UMMT, Tizi-Ouzou Algérie
ALEXANDRE VIAL	Rapporteur	Professeur, UTT, Troyes
ANNE-LAURE FEHREMBACH	Examineur	Maître de conférences, AMU, Aix-Marseille
MAXIME JACQUOT	Examineur	Maître de conférences HDR, UFC, Besançon
JÉRÉMIE TORRES	Examineur	Maître de conférences HDR, UM2, Montpellier
SYLVAIN LECLER	Examineur	Maître de conférences HDR, US, Strasbourg
FADI BAIDA	Directeur de thèse	Professeur, UFC, Besançon

ACKNOWLEDGMENTS

I would like to extend my thanks to: the "Iraqi Ministry of Higher Education & Scientific Research" for financing my studies, my thesis supervisor Mr. Fadi Baida for accepting me in his research team, for sharing his knowledge and the Franche-Comté University computing center: "Mesocentre de calcul de Franche-Comté" for providing me with the necessary resources.

Mr. Fabrice Devaux, for presiding the thesis jury, and all the jury members.

I am grateful to everyone with whom I worked during this period (administrative staff, PhD students, FEMTO-ST members or researchers) and in generally everyone in the FEMTO-ST Institute that I have had the opportunity to know over these years.

Finally, my deepest appreciation and gratitude however go to my most wonderful family: my parents, my sisters, my brothers, my sons and my beloved wife.

CONTENTS

1	GENERAL INTRODUCTION	1
2	MODELING OPTICAL RESPONSE OF METALLIC NANO-PARTICLES	7
2.1	Introduction	7
2.2	State of the art on optical properties of metal nanoparticles	7
2.3	Modern concept of surface plasmons	13
2.3.1	Classification of Plasmon resonance	13
2.4	Optical response of metallic NPs	16
2.4.1	Mie theory: Analytical model for spheres	16
2.4.1.1	Mie formulations	16
2.4.2	Absorption, scattering and extinction efficiencies with Mie	19
2.5	Finite Difference Time Domain FDTD method	20
2.6	Exploitation of Maxwell equations	21
2.6.1	Finite differences	23
2.6.2	Yee algorithm	24
2.6.3	Criteria of stability for FDTD code	26
2.7	Boundary conditions	27
2.7.1	Perfectly Matched Layer (PML)	27

2.8	Metal dispersion models	28
2.8.1	Drude model	29
2.8.2	Drude-Lorentz model (DL)	29
2.8.3	Drude Critical Points (DCP)	30
2.8.4	Description of permittivity for metals	31
2.9	Total field/Scattered field technique (TF/SF)	33
2.9.1	TF/SF in one-dimensional	33
2.9.2	TF/SF in two-dimensional	35
2.9.3	Model validation of 2D TF/SF	37
2.9.4	TF/SF Demonstration in three-dimensional	38
2.10	Modeling the optical response: FDTD-TF/SF validation	42
2.10.1	Framework of scattering of light	42
2.10.2	Comparison numerical result with analytic result	45
2.11	Contour Path Technique (CPT)	46
2.11.1	Implementation of CPT in FDTD code	49
2.12	Absorption, scattering and extinction properties of Bowtie and Diabolo nano-antennas	52
2.12.1	Effect of the material on the optical response of DA	55
2.12.2	Effect of the host medium on the optical response of DA	57
2.12.3	Effect of the length	57
2.12.4	Effect of gap size	58
2.12.5	Effect of the metal thickness	60

2.13 Conclusion	60
3 OPTICAL TRANSMISSION PROPERTIES THROUGH SUB-WAVELENGTH ANNULAR APERTURES ARRAY (AAA)	63
3.1 Introduction	63
3.2 State of the art on the transmission through nanoapertures	64
3.3 Reason for choosing AAA	68
3.3.1 Types of waveguides	69
3.3.2 Dispersion diagram of the guided mode	69
3.3.3 TEM guided mode	71
3.4 Theoretical study of the excitation of <i>TEM</i> guided mode through AAA structure	75
3.4.1 Classification of the EM modes within AAA	77
3.5 Simulations results	79
3.5.1 Influence of gap ($R_o - R_i$)	79
3.5.2 Influence of the metal thickness	81
3.5.3 Influence of the period	82
3.6 The measured and simulated transmission of AAA	83
3.6.1 Brief details of the sample fabrication	83
3.6.2 Comparison between theory and experiment	83
3.7 Conclusion	85
4 TRANSMISSION PROPERTIES OF SLANTED ANNULAR APERTURE ARRAYS (SAAA)	89
4.1 A historical overview of the characterization and fabrication of SAAA structure	91

4.2	Comparison between AAA and SAAA	96
4.3	Influence of angle of inclination on the transmission spectra	98
4.4	Influence of angle of incidence	99
4.5	Influence of the azimuthal angle	101
4.6	Analytic treatment	103
4.6.1	Central symmetry of the transmission in SAAA.	105
4.6.2	Transmission spectra of an arbitrary SAAA.	105
4.6.3	Giant energy deviation	106
4.7	Conclusion	108
5	General Conclusion	109
I	Appendices	139
A		141
A.1	Dissipation of Energy	141
B		145
B.1	145
B.1.1	From the scattering matrix to the transmittivity	146
B.1.2	Properties of the scattering matrix	147
B.1.3	Properties of the eigenvalues	149
B.1.4	Resonant behavior of the eigenvalues	151

LIST OF DEFINITIONS

NPs	Nanoparticles
LSPRs	Localized Surface Plasmon Resonances
PSP	Propagating Surface Plasmon
SPR	Surface Plasmon Resonance
SPs	Surface Plasmons
SERS	Surface-Enhanced Raman Scattering
EOT	Extraordinary Optical Transmission
ET	Enhanced Transmission
MDM	Metallic Dielectric Metallic
HSV	Harmonics Spherical Vector
ETM	Enhanced Transmission Metamaterials
FDTD	Finite Difference Time domain method
PML	Perfectly Matched Layer
BOR	Body-Of-Revolution
TFSF	Total Field Scattering Field
CPT	Contour Path Technique
TE	Transverse Electric
TM	Transverse Magnetic
TEM	Transverse Electric Magnetic
DL	Drude-Lorentz model
DCP	Drude Critical Points
NAs	Nanoantennas
DA	Diabolo Antenna
BA	Bowtie Antenna
AAA	Annular Aperture Arrays
SAAA	Slanted Annular Aperture Arrays
CFL	Courant, Friedrich and Lewy
FTR	Frustrated Total Reflexion
PEC	Perfect Electron Conductor
FSS	Frequency Selective Surface
SFM	Split-Field Method
FIB	Focused Ion Beam

GENERAL INTRODUCTION

Metal nanoparticles (NPs) and their interaction with light have been acquiring great significance since antiquity. The first application viewed, was as the most well-known, the Lycurgus cup dating back to the fourth century, was displayed by the British Museum in London. Moreover, the popular stained glass windows adorning the cathedral of Chartres were manufactured by the inclusion of metal powders at the beginning of the 13th. Certainly, it was not known and proven then that these infinite color palettes obtained from metal nanoparticles existed because of the excitation of a Plasmon resonance.

The optical properties of metals NPs started to be studied systematically by Faraday who managed to synthesize colloidal gold solutions by the reduction of gold salts [1]. He demonstrated that the coloring of colloidal suspensions was intimately related to the role of the size and morphology of the metal grains in the light scattering process. In the absence of a theoretical framework, it was not possible to interpret these observations except through the Faraday intuition. At the end of the 19th century, the first theoretical treatment on the scattering of light by particles with subwavelength scale was achieved by Rayleigh [2]. The latter analyzed the diffusion of light by diluted gases, and his theory demonstrated that at high frequencies, light is scattered more efficiently by air molecules than at low frequencies. This interpretation provided the origin of the physical phenomena such as the yellow color of the sun and the blueness of the sky. In 1908, Mie succeeded to model the first full analytical solution of Maxwells' equations to describe the scattering and absorption spectra of a homogenous sphere [3]. His model shows that the spectra observed of metal nanoparticles have an intense resonance in the near-UV-visible. This resonance attributed to the interaction between light and the free conduction band electron of the metal that leads to produce an electron oscillation around the particle surface [3, 4, 5].

Since Mie's work, his analytical model provided an exact solution characterizing the

scattering of light by spherical form only. At that time, there was a little attention on the treatment of the effects of varying shape of particles in their optical properties because this parameter was not controlled yet. In 1912, Gan [6] was able to predict scattering cross-sections (different colors) of colloidal solution of ellipsoidal geometries with different aspect ratios. With reference to the case of the cup of Lycurgus, the observation of such intense colors were due to light scattering by the tiny metal present in the glass. In our present day, these resonances represent the coupling of collective oscillation of the conduction electrons in metal with an incident light which is known as Localized Surface Plasmon Resonance (LSPR).

It is not until several decades later, that research teams' attention has recently given rise in metal nanoparticle due to the discovery of surface enhanced Raman scattering (SERS) in 1974 [7, 8, 9]. The fascinating phenomenon (Raman emission enhancement) arises from adsorption of molecules on a metal surface and/or thanks to so-called surface plasmons (SPs) of roughened metals. This SP is another important element that will be involved in our topic as a bounded mode of a single interface or of a multilayer metallic structures.

On the experimental and theoretical sides, modern rapid advances were made in the fabrication and characterization on the nanoscale level for more than two decades. Several computational methods such as Finite Difference Time Domain FDTD [10] have been proposed for predicting the electromagnetic fields around the illuminated individual nanoparticles. This method supports a suitable systematic and general approach for determining the optical responses of plasmonic nanostructures.

Overall, we can see that SP can appear through the excitation of **two main kinds of** : (a) excitation of Localized Surface Plasmon Resonance (LSPR) mode which can resonate locally through a direct interaction between finite metal nanoparticles and light, and (b) the Propagating Surface Plasmons (PSPs) modes which supports the possibility of guiding of light in subwavelength metallic structures (i.e infinite thin films in the case of plasmonic wave-guides).

Localized surface plasmon resonance LSPR is a major phenomenon that controls the tunability of absorption and scattering spectra as well as the strong local field of metallic NPs [11, 12]. This means, it is highly sensitive to size parameters, morphology, shape as well as the environment [11, 12]. Therefore, NPs with anisotropic shapes are of great interest because of their considerable enhancement and polarization-dependent properties [12]. Anisotropic metal NPs are currently considered as the most desirable in the development of nano-optics. Plasmonic mode produces fascinating phenomena

through concentration of light into nanoscale volumes. Given this sense, metal NPs are considered as optical antennas due to their similar functionality as the antennas in the radio and telecommunication ranges [13].

Quite recently, great attention has been paid to tailoring of confinement properties through designing metal structures that are able to greatly magnify local electromagnetic fields. In fact, there are many applications that take their usefulness from the interaction of the matter with enhanced light. For example, a "good" optical antenna is characterized by efficient plasmonic properties and differs from one to another in terms of performance.

Controlling the plasmonic properties (local field enhancement and spectrally resonance wavelength) of different types of nanoantennas have been demonstrated in recent years [14, 15, 16, 17]. A successful new nanoantenna emerged in our team providing a highly confined and enhanced field at the visible region in a small metal gap of the called diabolo nanoantenna [18]. The study of the effects of various aspects of the latter have recently been discussed and presented. However, a detailed systematically study on this structure of its strong hotspot in terms of optical properties (scattering and absorption) is still lacking. From this point, the first part of this thesis seeks to provide the information needed for optimum choice of a such diabolo nanoantenna through the examination of the effects of its geometrical parameters (gap, length and thickness) and the dielectric constant of the host medium. All that previously mentioned as regards to the optical properties result from the excitation of LSPR on a single nanoparticle.

The second kind of plasmonic mode which is propagating surface plasmon PSP will be under the scope as another important part of this work. The first observation of surface plasmon SP was performed in the middle of the twentieth century when a metal was subjected to a beam of electron where an oscillation of surface plasma was created [19, 20]. In 1902, the sudden variation in the intensity of the diffracted light was recorded by Wood [21] when he illuminated a metal grating with polychromatic light. After, Wood's observation, an attempt had been emerged to suggest a physical interpretation of the phenomenon [22]. It is not until 1941 that Fano [23] in his theory, has associated these anomalies with the excitation of electromagnetic surface waves on the diffraction grating. These anomalies on the spectrum correspond to the propagating surface plasmon PSP which represent the coupling between the collective oscillation of free surface charges of the metal and light. These SPs propagate along the interface between metal and dielectric and have acquired their importance through the strong confinement of the electromagnetic field in the vicinity of the metal-dielectric interface. In the late 1960s, the excitation of surface plasmons SPs based on the attenuated-total-reflection method was reported by Otto, Raether and Kretschmann [24, 25]. Two decades after the discovery

of Wood, enhancement of light produced locally by excitation of SP has been gaining importance in the present days due to its vital role in nanophotonics. One of the most interesting examples in recent development of plasmonic can be found in the phenomenon of Extraordinary Optical Transmission (EOT) of light through subwavelength apertures in metal plates.

Great effort has been devoted to the study of the excitation of SPs on periodic nanostructures. This is mainly due to the observation made by T.W. Ebbesens team of an extraordinary optical transmission (EOT), which inevitably revolutionized the field of nano-optics and opened a wide range of applications from spectral filtering to nanoantennas via single molecule spectroscopy [26]. This large transmission through subwavelength apertures pierced in an opaque metal film is linked to surface plasmon resonance (SPR) modes at the dielectric/metal interfaces and/or to plasmonic guided modes inside the apertures [26, 27, 28]. Although most of the works on EOT are based on SPR, guided modes offer a better efficiency and the advantage of increasing the transmission peak [29].

Many constructions have been theoretically proposed and experimentally designed to this phenomenon. Among the possible configurations of the cavities, Annular Aperture Arrays (AAAs) [30] are the most motivating structures because they can considerably increase the light transmission compared with cylindrical or rectangular apertures [31]. The coaxial apertures present higher values of the cutoff wavelength of its fundamental guided mode, namely the Transverse Electric (TE_{11}) mode. However, this bi-connexe section waveguide supports as well a more interesting plasmonic guided mode which has cutoff-less wavelength: the Transverse Electric and Magnetic (TEM) mode. Consequently, the AAA have become an interesting candidate for the Enhanced Transmission (ET) in the visible range.

Given the above interesting reasons associated with the optical properties to address, this thesis includes the improvement of an existing FDTD algorithm by integrating the called Total Field/Scattering Field (TF/SF) and Contour Path Technique (CPT). The TF/SF technique allows determining the absorption and scattering efficiencies of any geometry (eliminates restrictions in Mie theory). Whereas the CPT is able to reduce the staircase effect arising from the spatial meshing of such object.

After a general overview, the second chapter in this manuscript starts with some details of the previous studies performed on the nanoparticles (NPs) and their optical responses (scattering and absorption) with different shapes. Thereafter, a brief review of the concept of surface plasmons together with the classification of the electronic oscil-

lations into LSP and PSP are presented. The optical response of metal nanoparticles associated with Mie theory is addressed. The latter section will be followed by the important numerical tool needed to achieve the goal of this work which is the FDTD method including our development of a homemade code through adapting the TF/SF as well as the CP techniques. The validation of this modified code will be implemented in comparison with the analytic solution. In view of this, a comparison between two different configurations of nanoantenna will be conducted to show the effect of shape on the optical response of a diabolo nanoantenna and how this structure yields to an effective cross section that is larger than its actual size when it interacts with light. Study of the absorption and scattering efficiencies by diabolo nanoantenna for different metal types is performed.

As stated in the context of our interest in the PSP excitation, Chapter 3 is dedicated to the characterization of the transmission through AAAs configuration and its significant fundamental aspects that are accompanied, such as the excitation of some guided modes. In the beginning, we give an overview of the state of the art on the Extraordinary Optical Transmission (EOT). It will be followed by a brief description of the fundamental waveguide theory. The last section is devoted to theoretical study of the excitation of TEM guided mode through AAAs involving the investigation of the effects of the array size and the metal thickness on ET. This chapter also sheds light on the comparison of the transmission measurements that was conducted in the context of an earlier thesis with our simulation results.

Due to interesting reasons associated with the excitation of the *TEM* mode, the study of the transmission properties of the previously proposed and modified AAA structure, which is a Slanted AAA, will be the main scope of chapter 4. We will recall a brief overview about the characterization and fabrication of the SAAA structure. Firstly, we will carry out a comparison between the transmission of an AAA and a SAAA structures having the same film thickness. Then, numerical and analytical demonstrations of some intrinsic properties of the structure will be discussed. This theoretical study will examine the influence of angle of inclination which is the distinguishing mark in SAAA structure on the transmission response. Other geometrical parameters such as angle of incidence, the azimuthal angle, and their influences in two cases of TE- and TM-polarization on transmission spectra, will be discussed. At the end of this chapter, we address an analytic treatment together with our numerical results showing the very important characteristics on transmission of this structure such as giant energy deviation over very small distances (smaller than the wavelength). Finally, the conclusion of the main theoretical results of the current work will be summarized with the most important remarks and the perspectives

in chapter 5.

MODELING OPTICAL RESPONSE OF METALLIC NANO-PARTICLES

2.1/ INTRODUCTION

In this chapter, a state of the art on nanoparticles (NPs) and their optical response supported by Localized Surface Plasmon resonances LSPRs is presented. In this overview, we address different studies including several types of isotropic (spherical) and anisotropic NPs such as Bowtie and Diabolo nano-antennas. This part will be followed by a more detailed description of the Mie theory that can address basically isotropic NPs through the determination of their absorption and scattering efficiencies. FDTD algorithm was adapted to such studies by developing the Total field/Scattered field (TF/SF) technique. This allows to determine the efficiencies of any geometrical NPs shape. A comparison with Mie theory is first done to validate our code after including the Contour Path Technique (CPT) to faithfully reduce the staircase effect arising from the FDTD spatial meshing. A systematic study on the optical properties of diabolo nanoantenna will be presented at the end of this chapter.

2.2/ STATE OF THE ART ON OPTICAL PROPERTIES OF METAL NANOPARTICLES

A considerable attention has been paid to the topic of optical properties of nano-sized metallic nanoparticles. When light interacts with metal nanoparticles, a high enhancement of the electromagnetic field at their surfaces can occur. This phenomenon arises thanks to the excitation of local plasmon resonance. Since the first indication by Gustav

2.2. STATE OF THE ART ON OPTICAL PROPERTIES OF METAL NANOPARTICLES

Mie in 1908 [3], this resonance is attributed to the interaction between light and the free conduction band electron of the metal that leads to produce an electron oscillation around the particle surface [5, 11]. Recently, this phenomenon is known as the localized surface plasmon resonance (LSPR) [12]. The wavelength resonance of plasmonic oscillation is particularly dependent on permittivity of the material (i.e. the plasma frequency of the metal) [11] not only, but also on the size, shape of the particle, as well as the dielectric constant of the host medium. The plasmon resonances of such nanostructure can be tuned over wide range of wavelengths, by adjusting the properties of any nanoparticle. [12].

Mie theory is the first study characterizing the scattering and absorption spectra of spherical particles. After discovering of the Surface-Enhanced Raman Scattering (SERS) effect [7, 8, 9], a renewed attention from research teams has been expanded to the metal nanoparticles due to recent rapid advances in fabrication and characterization at the nanoscale. Thereafter, a large number of publications have been devoted to the study of high enhancement of the electric field on the metal nanoparticles surface including many applications. A very interesting paper description of recent progress in the theory of nanoparticle optical properties, particularly methods for solving Maxwells equations for light scattering from particles of arbitrary shape in a complex environment can be found in references [12, 32]. In that work, the qualitative features of dipole and quadrupole plasmon resonances for spherical particles are presented. The determination of far-field properties extinction and scattering cross-sections, local fields, and other optical properties for nonspherical particles is discussed by means of analytical and numerical methods. Moreover, another form of nanoparticle (triangular prisms) is numerically modeled. Several publications have been published in recent years documenting the theoretical study in order to understand the phenomena of the surface plasmon mode in metal nanostructures. Localized Surface Plasmon Resonance LSP, its local electric field and scattering cross section on several shapes of nanoparticles were also evaluated by the FDTD (finite difference time domain) method in [33, 34, 35, 36]. As explained in those references, the effective cross-section can be greater than the actual structure area at the resonance frequency and as mentioned above that scattering factor is sensitive to geometry. Thus, it can be exploited to increase the strength interaction with incident field. In [34], the optical response spectra, local electromagnetic fields and induced charge densities at the surfaces of the nanostructures (uniform single nanoshells, nanoshells with surface defects, and nanoshells with shape distortions from a spherical geometry) are investigated using the finite difference time domain method FDTD. The quasistatic approach to particles of arbitrary shape compact metal is quantitatively described the light scattering from the lowest resonance mode [37]. Another study has been suggested by Hao et al.

in reference [38] to determine the intense localized field at the particle surface of more complex shapes via the numerical methods. In the literature, several papers have been published to demonstrate the scattering efficiencies and optical resonance wavelengths of NPs for biological imaging and biomedicine applications [39, 40, 41, 42, 43]. In the context of LSP-based applications in biomedicine, Kessentini and Barchiesi [43] studied the absorption efficiency of set of NPs (nanorods, nanoshell and hollow nanosphere) in order to get the highest efficient among them, for using in necrosis of cancer cells, in photothermal therapy. In that study, the Mie theory, the Discrete Dipole Approximation (DDA) were used and they showed that for the shallow cancer therapy, the hollow nanosphere seems to be efficient than the other NPs (see Fig. 2.1)

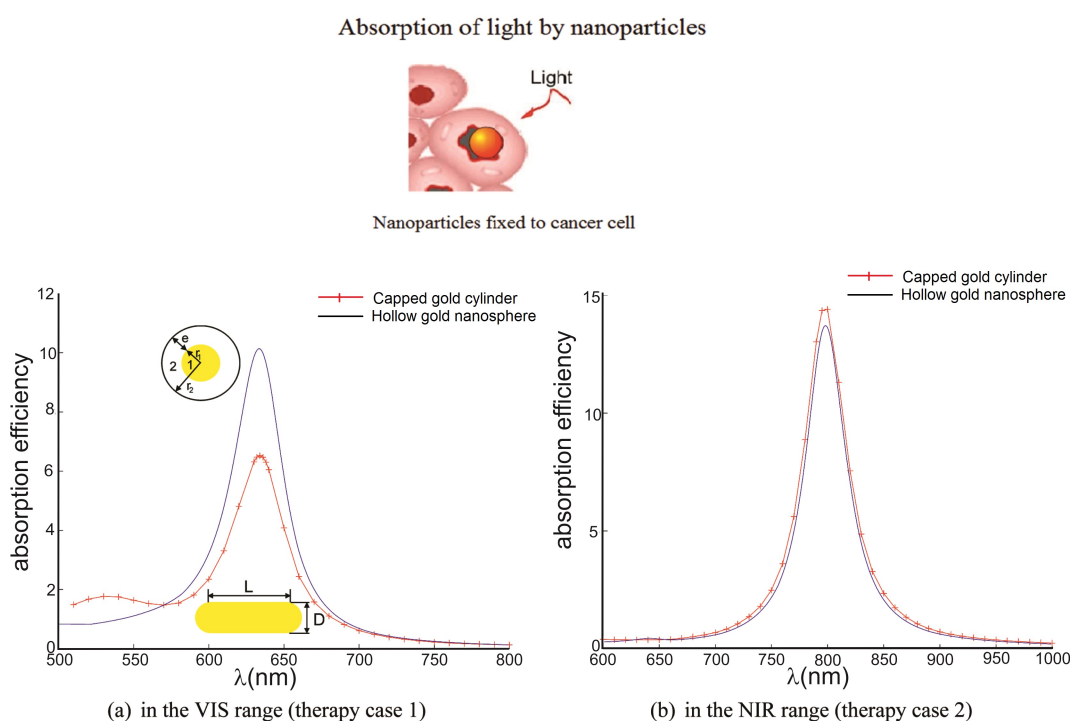


Figure 2.1: Absorption efficiency by capped cylinder and hollow nanosphere in (a) VIS range and (b) NIR range. The DDA method is used to get the spectra of capped cylinder and Mie theory is used to get spectra of hollow nanosphere. Ref. [43].

A review paper published by Myroshnychenko et al. [36] in 2008, discusses the theoretical methods for predicting and understanding the optical response of gold nanoparticles. Another interesting study in this issue has also been published in [14] and [44]. In those papers, some interesting nanostructure geometries, including nanocubes and nanobars displayed a characteristic enhanced and tunable plasmon resonances (see figure 2.2) are studied.

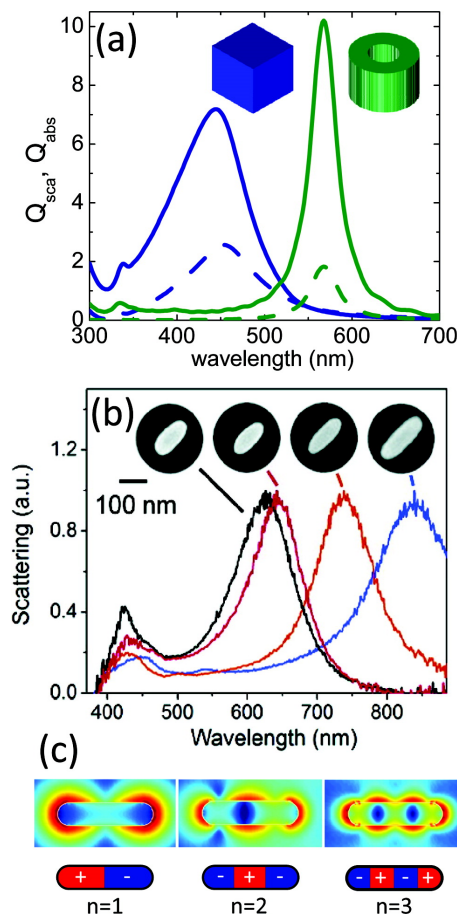


Figure 2.2: (a) Calculated absorption (solid lines) and scattering (dashed lines) efficiencies for a cubic (blue) and a ring (green) shaped silver NP. The particles have similar dimensions, both the side of the cube and the diameter of the ring are 50 nm. (b) Experimental measurement of scattering spectra of silver nanobars. (c) Electric field intensity enhancement corresponding to the three lowest longitudinal LSPRs. Note that, the color map of the field amplitude scale from 0.1 (blue) to 100 (red). The bottom sketches depict the instantaneous charge distributions for three plasmonic resonances. Ref. [14].

In the context of LSPRs, the ability of concentrating the light into nanoscale volumes provided by plasmonic mode leads to turn-on large local enhancements of electromagnetic energy. This phenomenon makes to recall the fundamental of antennas working in the radio and telecommunication systems, although at optical spectrum [45, 46, 47, 48, 49, 50, 51, 52, 13, 53]. Given this sense, metal NPs can behave as nanoantennas in the optical range. The highly confined and enhanced electromagnetic field in the optical frequency region, resulting from pairs of nanoantennas with a small gap between them or by nanoantennas with particular shapes, makes these structures the focus of researchers' attention. One of the understandable examples of the enhanced light with metal nanoparticles is the surface-enhanced Raman spectroscopy [54, 55, 56] which is a Raman emission (Raman scattering signal) of molecules adsorbed onto or near

a roughened noble metal under certain condition that can be extremely enhanced and show a surprisingly high interaction cross section. LSPRs are particularly very promising candidate to design antennas operating for many applications such as enhanced nonlinear effects, spectroscopic analysis, imaging and identification of nanoscale amounts of substances and single molecules and nanorefractometry [13, 53, 57, 58, 59].

In recent years, research into plasmonic properties of different types of antennas has become very common. In [60], it was found that the FDTD calculated and experimentally measured extinction efficiencies of the optical antennas are influenced by antenna shape, length, and sharpness upon the intensity of the optical fields. Several authors [14, 15, 16, 17, 36, 61, 62, 63, 64, 65, 66, 67, 68, 69, 70, 71, 72, 73] have demonstrated the two main mechanisms that can be observed at plasmon resonance excited in metal NPs; the absorption and scattering. In optical nanoantennas domain, the researchers are looking for design an efficient antenna characterized by a large cross section and a large localized field enhancement. This structure has the possibility to concentrate EM energy from the incident field with high efficiency. Therefore, this leads to transfer maximum quantity of energy into small volumes in the vicinity of the nanoantenna. As an example, simple idea that emerged to obtain a good performance was inspired from a nanobar optical antenna and consists of separating it in two parts thereby creating a gap along its long axis. Thus, the enhancement of the field then can be stronger without any reducing in the effective cross section of in the original form. This proposition has been studied by Ghenuche et al. [74], through the plasmonic mode properties. It was found that, the luminescence that occurs between the two arms (enhancement squeezed at the gap of antenna) is much larger than the one of a gapless antenna with the same whole length. Thus, the concept of plasmonic gap becomes essential for the design of nanoantenna.

Another structure, based on the above idea, is the bowtie antenna. The physical properties of this configuration are intriguing due to their extremely strong response and the tunable resonance in its nanojunction gap [61, 63, 70, 75, 76, 77, 78, 79, 80, 81]. The super performance of bowtie antenna led to explore a new characteristic by connecting their two apexes metal triangles in a narrow waist metal bar. Therefore the resulting geometry for this arrangement is then called diabolo antenna. The highly amplification of local magnetic charge accumulation at the tips is then converted into a high electric current through the metal junction (inductive effect). The latter generates a high, magnetic field coiled around the metal gap. The first study on diabolo nanoantenna was performed in our team in 2011 by Grosjean et al. [18]. In that work, it was found that the strong magnetic hotspot generating in metal gap of the diabolo nanoantenna can be explained through the Babinet theorem which is a relation between the electric and magnetic fields

2.2. STATE OF THE ART ON OPTICAL PROPERTIES OF METAL NANOPARTICLES

of an aperture in an infinity thin perfectly conducting film and its complement. The determination of the electric field properties of the latter provides spectroscopic and spatial approach to the optical magnetic field of metal film of finite thickness and vice versa. The first numerical results showed a 2900-fold enhancement of the magnetic field at a wavelength of 2540 nm (see figure 2.3). Reference [18] analyzes and discusses various aspects of diablo nanoantenna. Nevertheless, there are still some interesting and relevant points to be addressed.

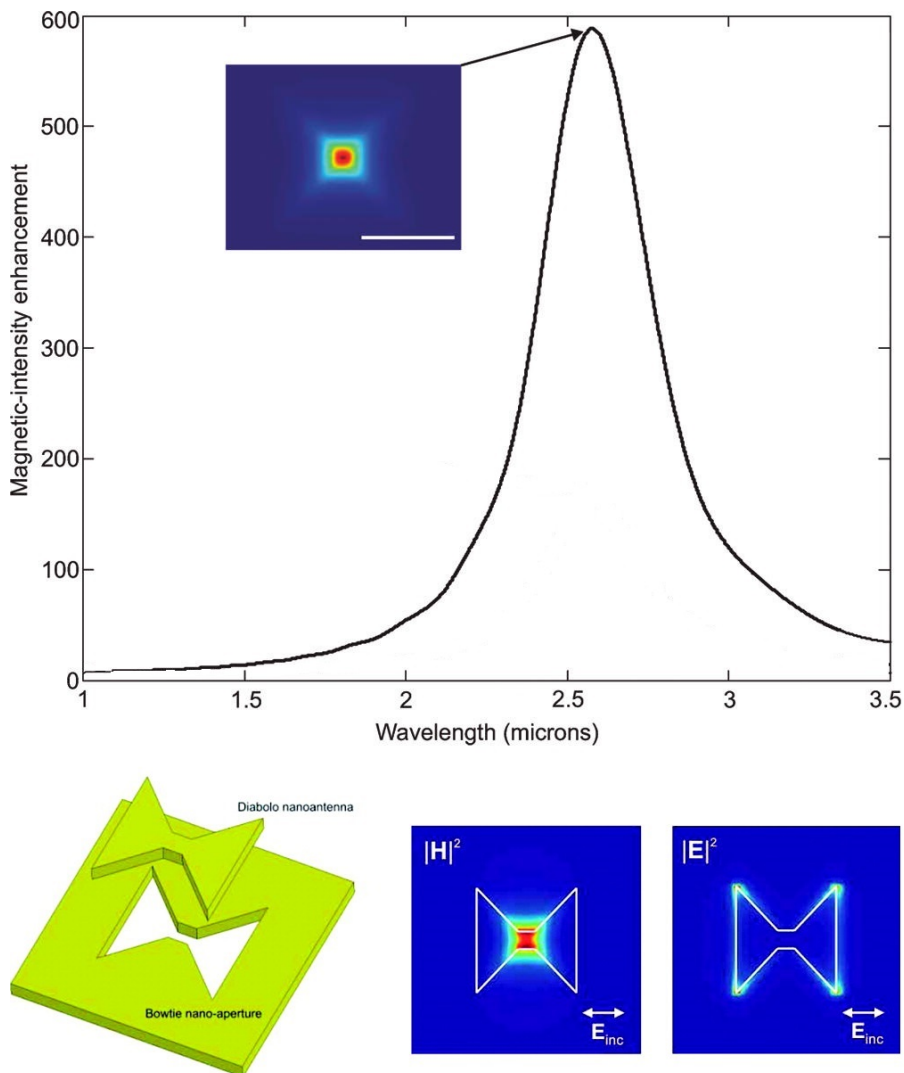


Figure 2.3: Plasmonic resonance in diablo nanoantenna and its near-field enhancement. The hot spot is due the strong magnetic field. Ref. [18].

This chapter is an attempt to show the potential and characteristics of localized surface plasmon resonance LSPR properties of nanoparticles NPs. More specifically, we focus on determining the localized energy enhancement factor in term of optical response

(scattering and absorption) of diabolito nanoantenna and the effects of their geometrical parameters (gap, length and thickness) and dielectric constant of the host medium. This object is the interest of the research team in our laboratory due to its potential applications in the optical domain.

To this end, we have to address and recall the background of this topic such as Mie theory which provides analytical solutions for spheroid forms. This step is necessary to validate our numerical tool by comparing it with those results obtained from the Mie theory. Subsequently, we prepare our numerical tool to facilitate our job using finite time difference domain FDTD method. We sought to extend an existing algorithm in order to contribute in the theoretical modeling of NPs of any shape. It is worth to be mentioned that the simulation for absorption and scattering requires adapting the so-called total field scattered field technique TF/SF in our code. This latter is previously used in literature but it was not available in our team.

2.3/ MODERN CONCEPT OF SURFACE PLASMONS

This section introduces the various concepts related to the excitation of plasmon. The two kind of propagating and localized surface plasmons will be introduced. These two plasmon resonances are directly involved in the optical responses of the structures that will be studied in this work: localized SP in NPs or nano-antennas and propagating SP in the case of enhanced transmission through metamaterial. We will not make an exhaustive study in this area, but we will briefly present surface plasmons and the main points that we need in this manuscript.

2.3.1/ CLASSIFICATION OF PLASMON RESONANCE

The essential component of plasmon resonance is a metal, due to the excitation of surface plasmon SP modes which are electromagnetic waves coupled to the collective oscillations of conductive electrons in the metal. The plasmonic metal nanostructures can be classified based on the supported plasmonic modes. As mentioned before, there are two categories of electronic fluctuations which are Propagating Surface Plasmons (PSPs) and Localized Surface Plasmons (LSPs) [52, 82, 83].

In the case of PSPs, the existence of the negative/positive charges along the metal surface leads to a propagating electronic density wave in a direction parallel to the

metal/dielectric interface. A TM polarized electromagnetic wave is generally needed to induce this kind of SPRs. In this case, the magnetic excitation field H is perpendicular to the incidence plane (xz) as shown in Fig.2.4(a). The dielectric permittivity function of the metal and the wavelength of the exciting radiation affects on the propagating length [84]. One of the basic concepts associated to PSPs, is the dispersion relation which is of fundamental interest for understanding the coupling of light to PSPs. The confined EM modes can be supported on a modest system such as an infinite flat metal-dielectric interface. The dispersion relation for the plasmonic modes carried by the latter is a solution of Maxwell equations under the convenient boundary conditions that gives the frequency-dependent SP wave-vector, k_{SP} as:

$$k_{SP} = k_o \sqrt{\frac{\epsilon_m \epsilon_s}{\epsilon_m + \epsilon_s}} \quad (2.1)$$

where $k_o = \omega/c$ is the modulus of free-space wavevector, ϵ_s and ϵ_m represent the frequency-dependent permittivity of the metal and the dielectric material respectively. In general description, when we consider a silver metal and $\epsilon_m = 1$, according to Eq. 2.1 and at SP resonance, the ϵ_s must has both negative and complex (the latter, due to absorption in metal). At red wavelength, the permittivity of Ag metal decreases and approaches $-\epsilon_m$ causing the real part of the denominator in Eq. 2.1 to vanish, resulting $k_{SP} \cong 1.03k_o$. This increase leads to the concentration of EM energy into subwavelength volumes at the metallic-dielectric interface. The PSPs can be also excited on periodic arrays of subwavelength holes in optically thick metallic that can provide the enhanced transmission [26]. More details on PSPs are given in chapter 3.

In the case of nonpropagating excitation of surface plasmons (i.e. direct interaction of metal NPs with light), the electronic oscillations occur locally around the nanoparticle (see Fig. 2.4(b)), the corresponding surface oscillation is then called localized surface plasmon resonance LSPR. The induced dipoles in LSPR vary their direction in the external field every half period, which composes a nonpropagating oscillations mode. In the LSPR, the confined electronic oscillations enhance the local field distribution at the surface of the NPs. The remarkable property in plasmonic modes can simply realize in the polarizability, α_p , of a spherical metallic NP. An accurate expression for α_p outside a nanosphere of radius, R surrounded by dielectric medium, can be written taking into consideration electrostatic (Rayleigh) [2] approximation as:

$$\alpha_p = 4\pi R^3 \frac{\epsilon_m - \epsilon_s}{\epsilon_m + 2\epsilon_s} \quad (2.2)$$

As the same way to what occurs for k_{SP} in the flat shape, α_p shows a strong resonant

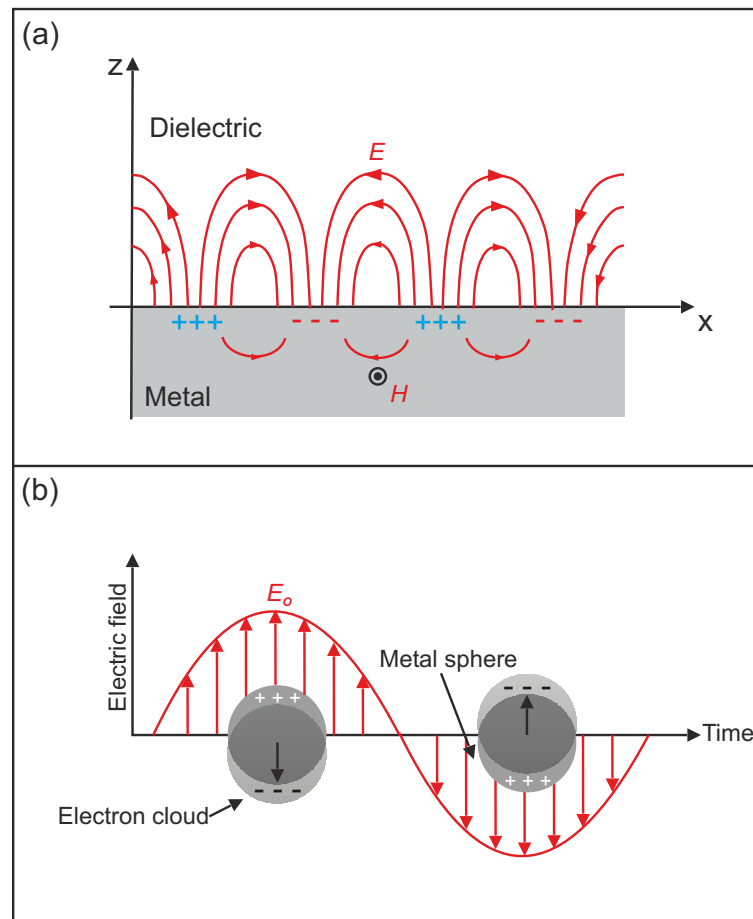


Figure 2.4: Schematic illustration of the two types of plasmonic nanostructures. (a) The excitation of free electrons leads to create a propagating surface plasmon (PSP). This mode propagate along the surface of the metal nanostructure. (b) The surface charges are locally oscillated around the metal nanoparticles. This is known as a localized surface plasmon resonance (LSPR). Refs. [82, 83, 52].

behavior for smaller metal permittivities, diverging for frequencies governing by the poles of the polarizability, given by $\epsilon_s = -2\epsilon_m$. In comparison with flat geometry, the consequences of the polarizability can be understood as the presence of resonance in the NP response at incident fields corresponding those of the plasmonic modes provided by the NP. Equation 2.2 is valid to spherical geometries in electrostatic system, but in metal particles of any shape and size, the study of LSPRs can be explored by full electrodynamic calculations based on numerical approaches.

2.4/ OPTICAL RESPONSE OF METALLIC NPS

To understand the optical response of resonant metallic structures, we need to have an accurate description of the electromagnetic modes function of the geometrical parameters and the dispersion properties of the particles under study. The most common method to this issue is based on analytical solutions of Maxwells equations that can only be obtained for simple geometries, such as spheres. For the latter, the solutions is given through the Mie theory. Consequently, we will firstly describe this analytical model for better understanding the occurrence of localized surface plasmon resonances LSPRs, by calculating the extinction, scattering, and absorption cross sections. For reasons related to the limitations of this model, it is necessary to use rigorous computational approaches qualified for dealing with more complex geometries. Therefore, the next step in this chapter will be intended to introduce the principle of Finite Difference Time Domain method (FDTD) with little detail allows the realization of calculations of optical response of nano-objects for any shapes and sizes.

2.4.1/ MIE THEORY: ANALYTICAL MODEL FOR SPHERES

The optical response can be predicated analytically through solving the Maxwells equations for spherically symmetric particles based on Mie theory [3]. This theory fully describes the effects of retardation, including radiative damping and higher-order multipole resonances. In addition, it is appropriate for the particle size of the order or much smaller than the wavelength λ of the incident field. Mie theory provides expressions giving absorption, scattering and extinction spectra of spherical metal NPs. This step allows to validate our numerical method through comparing the result obtained by this latter with those obtained from analytical solution.

2.4.1.1/ MIE FORMULATIONS

The full details on this theory can be found in the Bohren textbook (see Ch.4 in reference. [5]). Here, we recall the basic steps down to the final formulations. Mie theory is the exact analytical solution of Maxwells equations for the spheroid forms that allows determination of the scattered and absorbed fields to deduce the extinction one. According to the spherical symmetry of the problem, the spherical coordinate system is chosen to describe the electromagnetic fields by developing it on the basis of vector functions,

called Harmonics Spherical Vector (HSV). By using the Helmholtz equations for the E and H fields, their zero divergence and boundary conditions on the sphere surface, we can express the three electromagnetic fields, internal, scattered and incident one in the HSV basis. Let's consider the case of sphere with radius R , complex electric permittivity $\varepsilon = n_s^2$ embedded in dielectric medium of permittivity $\varepsilon_m = n_m^2$ and illuminated by a monochromatic (wavelength λ) plane wave.

Let's define on a set of useful dimensionless parameters:

$$m = \frac{n_s}{n_m}, \quad x = \frac{2\pi R}{\lambda}, \quad (2.3)$$

The expansion coefficients of the scattered field (a_n) and (b_n) are obtained by applying the relations of continuity of the tangential components of the electric field and magnetic field at the surface of the particle. In the conditions of orthogonality of HSV, the extinction (Q_{ext}), scattering (Q_{sca}) and absorption (Q_{abs}) cross-sections normalized to the physical cross section (πR^2) are given by the following formulas:

$$Q_{ext} = \frac{2}{x^2} \sum_{n=1}^{\infty} (2n+1) \Re[a_n + b_n] \quad (2.4)$$

$$Q_{sca} = \frac{2}{x^2} \sum_{n=1}^{\infty} (2n+1) (|a_n|^2 + |b_n|^2) \quad (2.5)$$

$$Q_{abs} = Q_{ext} - Q_{sca} \quad (2.6)$$

where

$$a_n = \frac{m\psi_n(mx)\psi'_n(x) - \psi_n(x)\psi'_n(mx)}{m\psi_n(mx)\xi'_n(x) - \xi_n(x)\psi'_n(mx)} \quad (2.7)$$

$$b_n = \frac{\psi_n(mx)\psi'_n(x) - m\psi_n(x)\psi'_n(mx)}{\psi_n(mx)\xi'_n(x) - m\xi_n(x)\psi'_n(mx)} \quad (2.8)$$

The coefficients, a_n and b_n , are also called Mie coefficients. The electric behavior of the scattered radiation is usually linked to a_n coefficients, whereas the magnetic one is associated with b_n coefficients. In these expressions, ψ_n and ξ_n are the Ricatti-Bessel functions written as:

$$\psi_n(x) = x j_n(x) = \sqrt{\frac{\pi x}{2}} J_{n+\frac{1}{2}} \quad (2.9)$$

$$\xi_n(x) = \psi_n(x) - i\chi_n(x), \quad \chi_n(x) = -xy_n(x) = -\sqrt{\frac{\pi x}{2}} Y_{n+\frac{1}{2}} \quad (2.10)$$

$$\xi_n(x) = \sqrt{\frac{\pi x}{2}} (J_{n+\frac{1}{2}} + iY_{n+\frac{1}{2}}) \quad (2.11)$$

2.4. OPTICAL RESPONSE OF METALLIC NPS

where $J_{n+\frac{1}{2}}$ and $Y_{n+\frac{1}{2}}$ are spherical Bessel-function of first and second order respectively.

Note that J_n and Y_n are solutions of the Bessel differential equation:

$$x^2 \frac{d^2 y}{dx^2} + 2x \frac{dy}{dx} + [x^2 - n(n+1)]y = 0 \quad (2.12)$$

whereas ψ_n and ξ_n are the solutions of the following differential equation:

$$x^2 \frac{d^2 y}{dx^2} + [x^2 - n(n+1)]y = 0 \quad (2.13)$$

ψ_n and ξ_n can be expressed as a sum of sines and cosines function. For example, the first terms read:

$$\psi_0(x) = \sin x \quad (2.14)$$

$$\xi_0(x) = \sin x - i \cos x \quad (2.15)$$

$$\psi_1(x) = \frac{\sin x}{x} - \cos x \quad (2.16)$$

$$\xi_1(x) = \frac{\sin x}{x} - i \left(\frac{\cos x}{x} + \sin x \right) \quad (2.17)$$

In Eqs. 2.4 and 2.5, the sum over n can be restricted to only a few terms. Therefore, the derivatives in Eqs. 2.7 and 2.8 can be expressed as:

$$\psi'_n(x) = \psi_{n-1}(x) - \frac{n}{x} \psi_n(x) \quad (2.18)$$

$$\xi'_n(x) = \xi_{n-1}(x) - \frac{n}{x} \xi_n(x) \quad (2.19)$$

This analytical method allows realizing and analyzing the effects of size, characteristics of material and environment on the electromagnetic scattering and absorption by spherical NPs.

2.4.2/ ABSORPTION, SCATTERING AND EXTINCTION EFFICIENCIES WITH MIE

According to Eq. 2.4, the extinction energy is defined as the total energy removed from the incident field by both scattering and absorption. After the interaction of light with the NPs, the absorption occurs through an inelastic processes that lead to dissipate the photon energy, otherwise the latter induces the electron oscillation in the matter to produce the light scattering. There are two types of scattering due to the nature of the photon emission: the Rayleigh scattering that occurs at the same frequency as the incident light, and the Raman one that has a shifted frequency [42].

Once the Mie coefficients are determined through Eqs. 2.7 and 2.8, we can calculate the extinction, absorption and scattering efficiencies or the electromagnetic fields caused by the spherical particle using Eqs. 2.4 and 2.5. We have developed a MATLAB[®] code to numerically determine these three coefficients.

We have validated our code by making some comparisons with already published results. The spectra for two different sizes of gold sphere particles, $R = 10 \text{ nm}$ and $R = 30 \text{ nm}$, embedded in a medium of $n_m = 1.5$ are shown in Fig. 2.6. As expected, in the case of small radius ($R \ll \lambda$), the polarizability of the sphere exhibits a dipolar resonance at a wavelength for which its permittivity is equal to $-2n_m^2$. In our case this corresponds to $\epsilon_s = -4.5$. According to figure 2.5, this condition is fulfilled for $\lambda \sim 521 \text{ nm}$. This result is in very good agreement with the position of the extinction coefficient maximum of figure 2.6. In addition, the scattering coefficient is so weak, due to the very small sphere volume, so that the extinction cross section is almost obtained by the contribution of the absorption one. For a 30 nm Au nanosphere, the situation is a little bit different due to grow the contribution of the scattering (see figure 2.6(b)). As reported in previous studies, these results can be useful to select the suitable nanoparticles in some applications. For example, it can use the smaller nanoparticles for the photothermal therapy because of light is mainly absorbed by the particles and hence the energy converted to heat, whereas larger one is desirable in imaging applications for example coherent Raman scattering or biological imaging [40].

This analytical method (Mie solutions) allows determining the efficiency of spheres, or ellipsoids form. **To bypass this restriction, it should be necessary to introduce a new method that allows to calculate the extinction and scattering efficiencies for any geometry of nanoparticles (nano-bar, nano-triangle, etc....).** For this purpose, numerical approaches are required. One of the most commonly used is the Finite Difference Time Domain (FDTD) method which has successfully been applied to solve light-matter

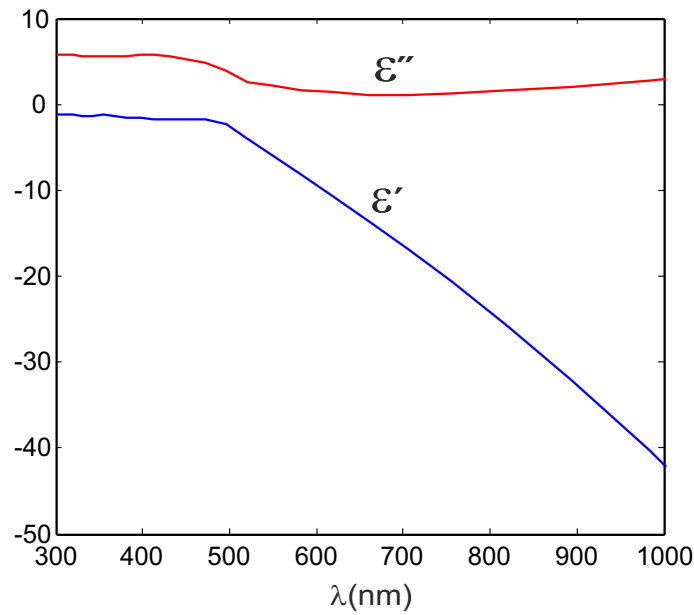


Figure 2.5: Real (blue curve) and imaginary (red curve) parts of the permittivity of gold in the optical region. The experimental data taken from Ref. [85].

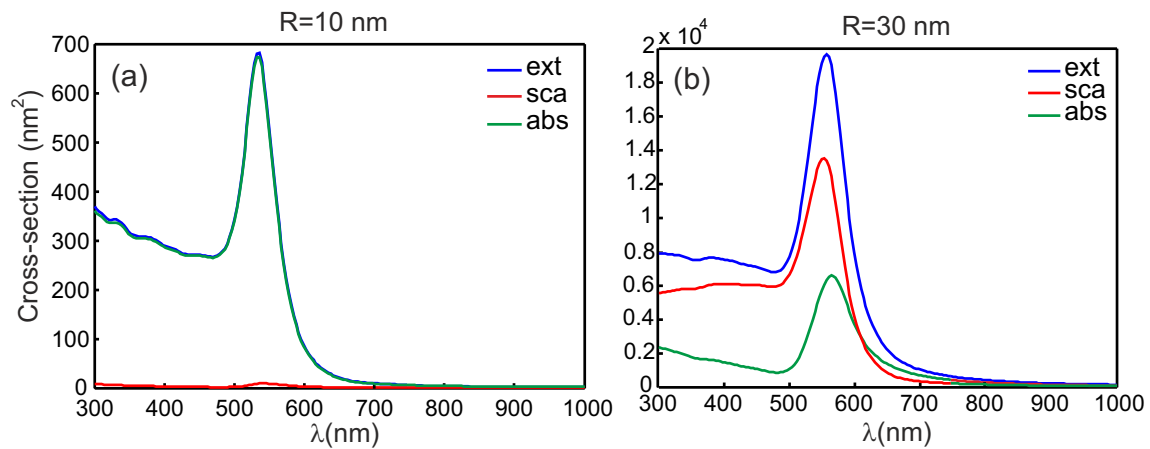


Figure 2.6: Extinction, absorption and scattering cross sections of a sphere made of gold with a radius of (a) 10 nm, (b) 30 nm. In both cases, the refractive index of the environment is 1.5. The dielectric function database are taken from [85].

interaction especially in nano-optics.

2.5/ FINITE DIFFERENCE TIME DOMAIN FDTD METHOD

The Finite Difference Time Domain (FDTD) method is one of the most important computational tools in electromagnetic since Yee suggested it in 1966 [86]. In the FDTD

approach, both space and time are discretized into a regular grid by exploiting the nature of Maxwell's equations in order to determine the E and H fields at different both positions and time-steps [10, 87, 88, 89]. In our laboratory, we use quasi featured homemade FDTD codes, including for example: 2D arbitrary isotropic or anisotropic in Transverse Electric (TE) and Transverse Magnetic (TM) polarizations [90, 91, 92], guided mode solver [27], 3D finite (unique) or infinite (periodic) structures [31, 93] and 2.5D Body Of Revolution-FDTD (BOR-FDTD) [94] in cylindrical coordinates. Furthermore, a dispersive media such as metals in the optical range can be modeled in this method, where the complex permittivity $\varepsilon(\omega)$ should be adapted through the use of analytical models that are then integrated into the FDTD algorithm through different schema as it will be shown in the following.

In this manuscript, after reviewing in outline the principles associated to the understanding of FDTD method, we will present the development of a new simulation tool derived from an existing FDTD code by adapting a new technique called Total Field/Scattered Field (TF/SF). By the latter, our code becomes able to extract the pure scattered field from the incident one and we will show how to detect and monitor those fields to determine the optical responses of NPs.

2.6/ EXPLOITATION OF MAXWELL EQUATIONS

Firstly, we recall the Maxwell equations that are needed to be implemented in the FDTD algorithm in the case of an isotropic ($\overleftarrow{\varepsilon} = \varepsilon$), linear and non dispersive material without sources ($\vec{J} = \vec{0}$). The two curl equations can then be expressed by:

$$\frac{\partial \vec{H}}{\partial t} = -\frac{1}{\mu} \overrightarrow{\nabla} \times \vec{E} \quad (2.20)$$

$$\frac{\partial \vec{E}}{\partial t} = \frac{1}{\varepsilon} \overrightarrow{\nabla} \times \vec{H} \quad (2.21)$$

\vec{E} and \vec{H} are the electric and magnetic fields respectively whereas μ and ε are the magnetic permeability and the dielectric permittivity respectively. After projection of these equations on the three axes of a Cartesian coordinate system \hat{x}, \hat{y} and \hat{z} , one obtains six

scalar relations below:

$$\frac{\partial H_x}{\partial t} = \frac{1}{\mu} \left(\frac{\partial E_y}{\partial z} - \frac{\partial E_z}{\partial y} \right) \quad (2.22)$$

$$\frac{\partial H_y}{\partial t} = \frac{1}{\mu} \left(\frac{\partial E_z}{\partial x} - \frac{\partial E_x}{\partial z} \right) \quad (2.23)$$

$$\frac{\partial H_z}{\partial t} = \frac{1}{\mu} \left(\frac{\partial E_x}{\partial y} - \frac{\partial E_y}{\partial x} \right) \quad (2.24)$$

$$\frac{\partial E_x}{\partial t} = \frac{1}{\varepsilon} \left(\frac{\partial H_z}{\partial y} - \frac{\partial H_y}{\partial z} \right) \quad (2.25)$$

$$\frac{\partial E_y}{\partial t} = \frac{1}{\varepsilon} \left(\frac{\partial H_x}{\partial z} - \frac{\partial H_z}{\partial x} \right) \quad (2.26)$$

$$\frac{\partial E_z}{\partial t} = \frac{1}{\varepsilon} \left(\frac{\partial H_y}{\partial x} - \frac{\partial H_x}{\partial y} \right) \quad (2.27)$$

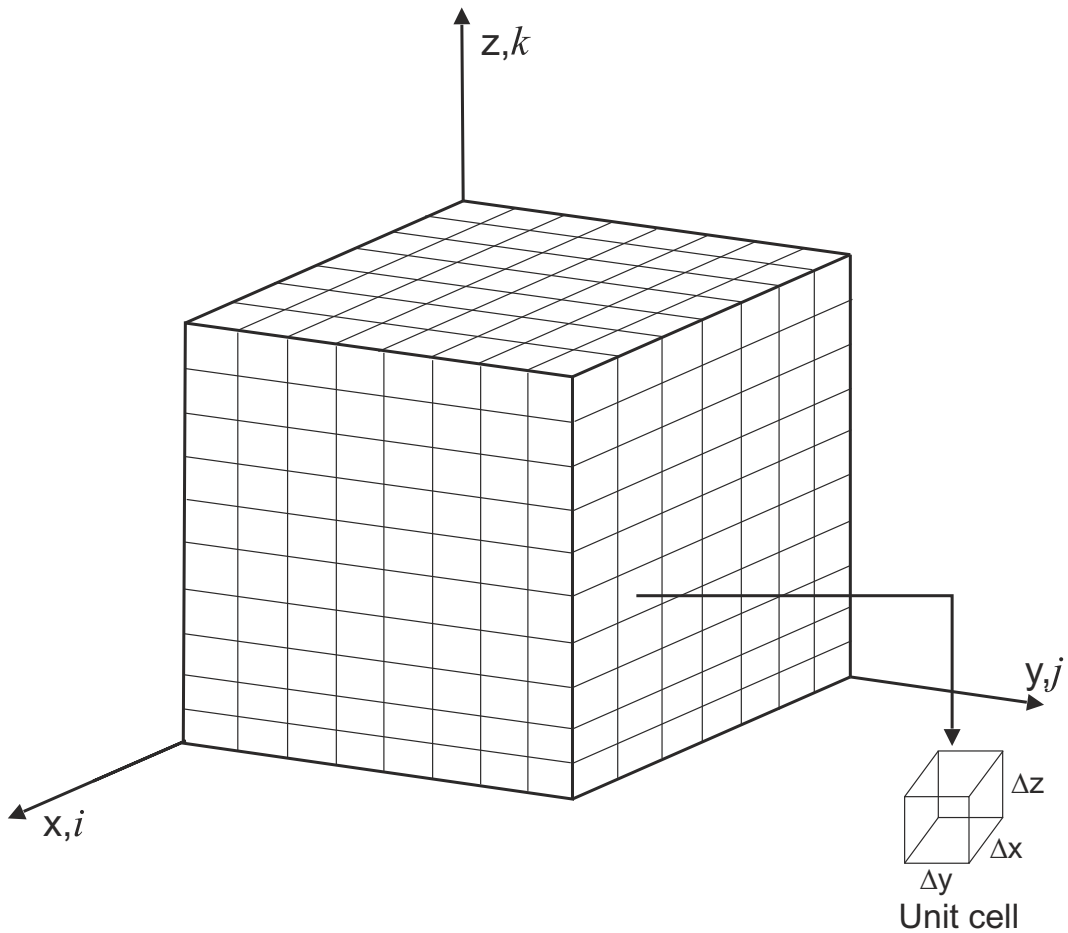


Figure 2.7: An example of windows of FDTD calculation and regular mesh.

These partial differential equations are then discretized both in the space and time in

order to treat them numerically.

2.6.1/ FINITE DIFFERENCES

As seen in Fig. 2.7, the calculation windows is represented as a rectangular parallelepiped and it is divided into $(N_x \times N_y \times N_z)$ cells, one cell has the elementary volume $(\Delta x \times \Delta y \times \Delta z)$ where Δx , Δy and Δz are the spatial discretization steps along the x, y and z directions respectively. It is necessary to define the node in the grid with a triplet integers (i, j, k) , therefore, the coordinates (x_i, y_j, z_k) of a node are fulfilled by:

$$x_i = i \Delta x \quad (2.28)$$

$$y_j = j \Delta y \quad (2.29)$$

$$z_k = k \Delta z \quad (2.30)$$

The discretization of the computational time can be written as Δt . This real time of the EM field evolution is connected to an integer n defining the number of temporal sampling and to this time step by:

$$t = n \Delta t \quad (2.31)$$

The temporal and spatial derivatives for the six components of the field (E_x, E_y, E_z, H_x, H_y and H_z) of Eqs. 2.22–2.27 are approximated from their Taylor expansions through a centered finite difference schema. Let us consider a function f that depends both on time and space so that $f = f(x, t)$. To calculate its spatial derivative at $x = x_i$, we need to express the Taylor expansion of this function at two spatial positions from either side separated by a distance of Δx . Consequently, using the Taylor expansion to the second order for $f = f(x, t)$ at the points $x_i - \frac{\Delta x}{2}$ and $x_i + \frac{\Delta x}{2}$, we get:

$$f(x_i + \frac{\Delta x}{2}) = f|_{x_i} + \frac{\Delta x}{2} \frac{\partial f}{\partial x}|_{x_i} + \frac{(\Delta x)^2}{2!} \frac{\partial^2 f}{\partial^2 x}|_{x_i} + O[(\Delta x)^2] \quad (2.32)$$

$$f(x_i - \frac{\Delta x}{2}) = f|_{x_i} - \frac{\Delta x}{2} \frac{\partial f}{\partial x}|_{x_i} + \frac{(\Delta x)^2}{2!} \frac{\partial^2 f}{\partial^2 x}|_{x_i} + O[(\Delta x)^2] \quad (2.33)$$

where $O[(\Delta x)^2]$ is the error of the expansion. By subtracting 2.33 from 2.32 one and gets the following equation:

$$\frac{\partial f}{\partial x}|_{x_i}^n = \frac{f_{i+\frac{1}{2}}^n - f_{i-\frac{1}{2}}^n}{\Delta x} + O[(\Delta x)^2] \quad (2.34)$$

2.6. EXPLOITATION OF MAXWELL EQUATIONS

where $f_i^n = f(x_i, t_n)$ with $x_i = i\Delta x$. This formula represents the expression of the first spatial derivative of the function f through a centered finite difference schema and shows that error is at the second order. This ensures a very stable numerical schema to the FDTD algorithm.

By the same way, we obtain the same temporal discretization schema through:

$$\left. \frac{\partial f}{\partial t} \right|_{x_i}^n = \frac{f_i^{n+\frac{1}{2}} - f_i^{n-\frac{1}{2}}}{\Delta t} + O[(\Delta t)^2] \quad (2.35)$$

2.6.2/ YEE ALGORITHM

In the Yees scheme, both electric and magnetic fields components are located at different points in a unit cell (see Fig 2.8). The electric field components are determined along the edges of the cell while the magnetic field components are determined at the centers of the cell faces. Therefore, each electric field component is surrounded by four magnetic field components and similarly for each magnetic field component. In Yee scheme, the temporal increment can be produced through a "leapfrog" discretization. The field components \vec{H} (or \vec{E}) are calculated at times odd multiples of the half time-step $\frac{\Delta t}{2}$, whereas the field components \vec{E} (respectively \vec{H}) are updated at the times even multiples of $\frac{\Delta t}{2}$ as shown in figure 2.9. Such a discretization allows estimating the time derivatives by keeping a centered difference schema as for spatial derivatives.

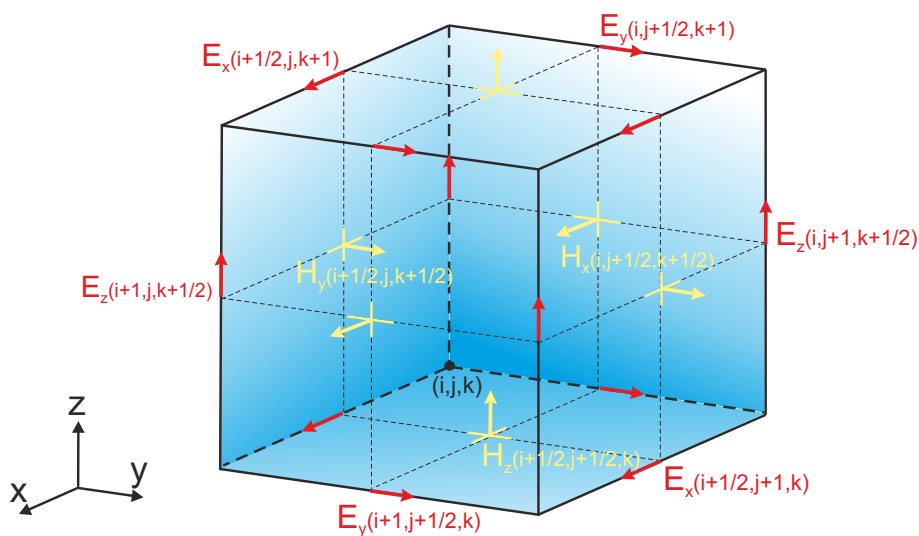


Figure 2.8: Yee cell in three dimensions. Note that the six components of electric and magnetic fields are represented in this cell.

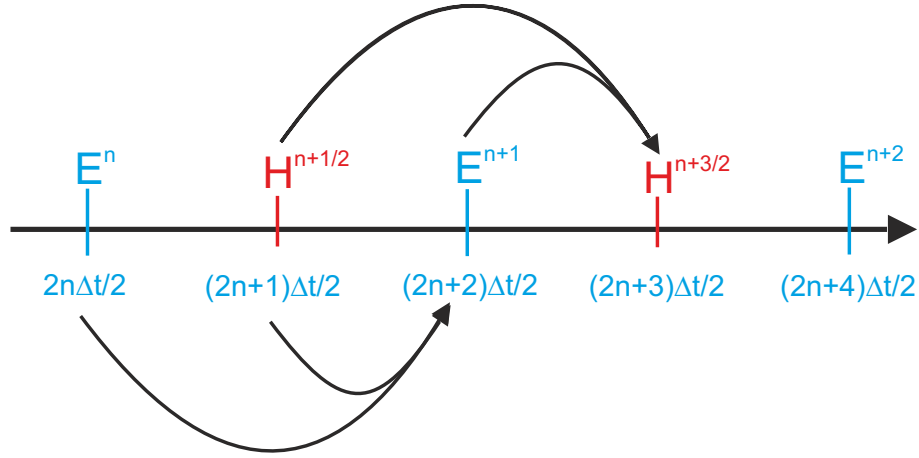


Figure 2.9: Temporal discretization into the Yee scheme.

Consequently, applying the central difference in equations (2.34 and 2.35) through the replacing of the partial derivatives in equations 2.22–2.27, the updated equations of electromagnetic components in the FDTD algorithm depending on the numerical diagram (Yee scheme) are:

$$H_x|_{i,j+\frac{1}{2},k+\frac{1}{2}}^{n+\frac{1}{2}} = H_x|_{i,j+\frac{1}{2},k+\frac{1}{2}}^{n-\frac{1}{2}} - \frac{\Delta t}{\mu_o} \left\{ \left[\frac{E_z|_{i,j+1,k+\frac{1}{2}}^n - E_z|_{i,j,k+\frac{1}{2}}^n}{\Delta y} \right] + \left[\frac{E_y|_{i,j+\frac{1}{2},k}^n - E_y|_{i,j+\frac{1}{2},k+1}^n}{\Delta z} \right] \right\} \quad (2.36)$$

$$H_y|_{i+\frac{1}{2},j,k+\frac{1}{2}}^{n+\frac{1}{2}} = H_y|_{i+\frac{1}{2},j,k+\frac{1}{2}}^{n-\frac{1}{2}} - \frac{\Delta t}{\mu_o} \left\{ \left[\frac{E_x|_{i+\frac{1}{2},j,k+1}^n - E_x|_{i+\frac{1}{2},j,k}^n}{\Delta z} \right] + \left[\frac{E_z|_{i,j,k+\frac{1}{2}}^n - E_z|_{i+1,j,k+\frac{1}{2}}^n}{\Delta x} \right] \right\} \quad (2.37)$$

$$H_z|_{i+\frac{1}{2},j+\frac{1}{2},k}^{n+\frac{1}{2}} = H_z|_{i+\frac{1}{2},j+\frac{1}{2},k}^{n-\frac{1}{2}} - \frac{\Delta t}{\mu_o} \left\{ \left[\frac{E_y|_{i+1,j+\frac{1}{2},k}^n - E_y|_{i,j+\frac{1}{2},k}^n}{\Delta x} \right] + \left[\frac{E_x|_{i+\frac{1}{2},j,k}^n - E_x|_{i+\frac{1}{2},j+1,k}^n}{\Delta y} \right] \right\} \quad (2.38)$$

$$E_x|_{i+\frac{1}{2},j,k}^{n+1} = E_x|_{i+\frac{1}{2},j,k}^n + \frac{\Delta t}{\epsilon} \left\{ \left[\frac{H_z|_{i+\frac{1}{2},j+\frac{1}{2},k}^n - H_z|_{i+\frac{1}{2},j-\frac{1}{2},k}^n}{\Delta y} \right] + \left[\frac{H_y|_{i+\frac{1}{2},j,k-\frac{1}{2}}^n - H_y|_{i+\frac{1}{2},j,k+\frac{1}{2}}^n}{\Delta z} \right] \right\} \quad (2.39)$$

$$E_y|_{i,j+\frac{1}{2},k}^{n+1} = E_y|_{i,j+\frac{1}{2},k}^n + \frac{\Delta t}{\epsilon} \left\{ \left[\frac{H_x|_{i,j+\frac{1}{2},k+\frac{1}{2}}^n - H_x|_{i,j+\frac{1}{2},k-\frac{1}{2}}^n}{\Delta z} \right] + \left[\frac{H_z|_{i-\frac{1}{2},j+\frac{1}{2},k}^n - H_z|_{i+\frac{1}{2},j+\frac{1}{2},k}^n}{\Delta x} \right] \right\} \quad (2.40)$$

$$E_z^{n+1}|_{i,j,k+\frac{1}{2}} = E_z^n|_{i,j,k+\frac{1}{2}} + \frac{\Delta t}{\varepsilon} \left\{ \left[\frac{H_y|_{i+\frac{1}{2},j,k+\frac{1}{2}}^n - H_y|_{i-\frac{1}{2},j,k+\frac{1}{2}}^n}{\Delta x} \right] + \left[\frac{H_x|_{i,j-\frac{1}{2},k+\frac{1}{2}}^n - H_x|_{i,j+\frac{1}{2},k+\frac{1}{2}}^n}{\Delta y} \right] \right\} \quad (2.41)$$

2.6.3/ CRITERIA OF STABILITY FOR FDTD CODE

The FDTD method as in all numerical methods may become unstable if the spatial discretization parameters $\Delta x, \Delta y, \Delta z$ and temporal Δt do not respect certain limitations. Arbitrary values of spatiotemporal discretization can cause to unbounded solutions of the electromagnetic field. Stability matter in evident numerical methods has been analyzed in detail by Courant, Friedrichs and Levy [95] and Von Neumann [96], from a mathematically strict approach. The latter gives stable schemes under a condition called CFL (for Current, Friedrich and Levy) and used in the FDTD method in the case of a uniform mesh [95]:

$$\Delta t \leq \frac{1}{c \sqrt{\frac{1}{(\Delta x)^2} + \frac{1}{(\Delta y)^2} + \frac{1}{(\Delta z)^2}}} \quad (2.42)$$

where c represents the speed of light in vacuum. Furthermore, the transition from continuous forms of Maxwell equations to the discrete numerical approximations can give rise on an intrusive effect called "numerical dispersion". The latter is linked to the fact that numerical pluses are propagated throughout time in the FDTD grid, with a phase velocity less than the actual velocity. The frequency, propagation direction in the grid and the spatial discretization induce the dispersion to vary [95]. Numerical dispersion errors grow with increased signal frequencies making the simulation results unrealistic. To prevent this problem, a mesh refining is required in the FDTD grid, so that the maximum spatial discretization is of the order [10]:

$$\frac{\lambda_{min}}{20} \quad (2.43)$$

where λ_{min} being the minimum wavelength of propagating waves in the FDTD grid. The limit of the spatial discretization given by equation 2.43 corresponds to a relative error on the phase velocity of about 0.2% (see Fig. 2.2, page 50 in Ref. [10]). In our code, we need to fulfill these two criteria in order to be acceptable in the context of our simulations.

2.7/ BOUNDARY CONDITIONS

Providing a finite grid in FDTD computational domain is one of the main challenges. To prevent very large calculation window volume, the latter must be truncated. This obviously requires the using of absorbing boundary conditions in order to avoid parasitical reflections on the window borders. In our code, we used the called Perfectly Matched Layer (PML) boundary conditions [10]. The PML is a loss medium reducing the reflection to the minimum over a broad spectrum and large angles of incidence.

2.7.1/ PERFECTLY MATCHED LAYER (PML)

This technique is one of most widely used technique that was introduced by J.P. Berenger in 1994 [97]. PML technique consists of surrounding the window of calculation by a layer giving rise to no reflection and almost fully absorbing all the propagating electromagnetic fields. Its principle depends on the condition of impedance matching at the interface between two media (main window and PML layer) but here PML medium exhibits both electric (σ) and magnetic (σ^*) conductivities as shown in figure 2.10(a). This impedance matching condition is written as:

$$\frac{\sigma}{\varepsilon} = \frac{\sigma^*}{\mu} \quad (2.44)$$

Consequently, a magnetic conductivity is required to achieve the impedance matching condition whereas, the absorption is required only for components of the fields that propagates perpendicularly to the interface (boundary of window calculation) and not in the parallel direction. This problem has been solved by Berenger via the suggestion of an artificially biaxial absorbing medium [97]. In the direction normal to the interface between the two media, the absorption is not zero while, there is no absorption along the axis parallel to the interface. In the PML medium, there are two artificial waves resulting from the split of the incident field (see figure 2.10(b)): A wave propagating at normal incidence with σ and σ^* different from zero and a second wave that propagates without absorption parallel to the interface direction. Sudden variations in conductivities at this interface introduces numerical spurious reflections due to the discrete representation of the physical problem. However, this effect was accurately optimized by imposing a progressive variation of the conductivities according to a polynomial law given by [97]:

$$\sigma(x_{pml}) = \sigma_{max} \left(\frac{x_{pml}}{l} \right)^n \quad (2.45)$$

where σ_{max} is the maximum conductivity at the FDTD grid truncation boundary including the PML layer, l is the width of the PML, x_{pml} represents the distance between the interface and the cell position inside the PML layer and n is the polynomial order generally fixed to 2 in our code. In chapter 3, where our attention is focused on the periodic structures,

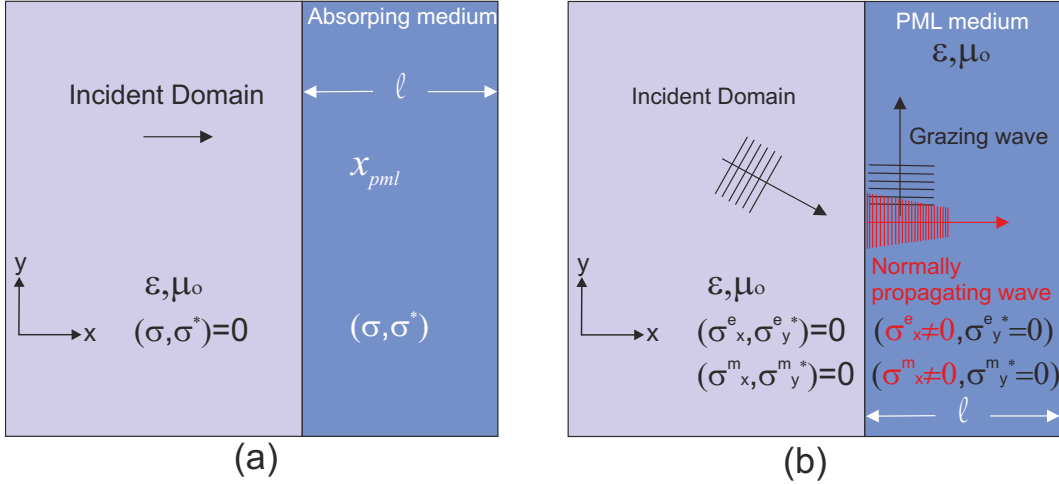


Figure 2.10: (a) Impedance matching principle. (b) Sketch of the PML principle.

the absorbing boundaries conditions are replaced by Floquet-Bloch periodic conditions. However, for a 2D periodic structure, PML are only necessary in the third direction where the structure is finite.

2.8/ METAL DISPERSION MODELS

An accurate study of the light-matter interaction should take into account the dielectric and magnetic properties of all the material involved into this interaction. In optics, homogeneous magnetic materials do not exist so that magnetic properties are independent from the frequency ($\mu_r = 1$). Nevertheless, dielectric properties can highly vary with respect to the illumination wavelength. Even if some dielectrics can be assumed to be non dispersive over a wide spectral range, metals-especially noble ones-exhibit large dispersion in that range. For such materials, equations 2.25 to 2.27 are no more valid due to the permittivity temporal dependency ($\epsilon(\omega) \rightarrow \epsilon(t)$). Calculation of the electric displacement vector is then needed to determine the upgrading schema between the electric \vec{E} and magnetic \vec{H} fields. The constitutive relation between \vec{E} and \vec{D} is then exploited and can only be integrated into the FDTD algorithm providing an analytical expression of the permittivity (linear media). This point was already addressed through the implementation of Debye [98, 99], Drude [100, 101], Drude-Lorentz [102] or, more recently, Drude critical

points models [103, 104].

2.8.1/ DRUDE MODEL

The Drude model of free electron [5, 105] for the dielectric function which, although uses the classical mechanical theory, can well take into account for interband transitions. This model was firstly proposed by P. Drude in 1900 [106], where the idea of a gas of free electrons moving in a static metal ions lattice (between positively charged ionic cores) is considered. Therefore, the electron-electron and/or electron-ion interactions are ignored and the motion of all the electron cloud is hence the average of the movement of individual electrons. Drude dielectric function $\varepsilon(\omega)$ is given by the following equation:

$$\varepsilon(\omega) = \varepsilon_{\infty} - \frac{\omega_D^2}{\omega^2 + i\omega\gamma_D} \quad (2.46)$$

where ω_D is the oscillation frequency of the electron density (often is called plasma frequency), γ_D is the damping coefficient and ε_{∞} is the high-frequency contribution that is usually superior or equal to one.

2.8.2/ DRUDE-LORENTZ MODEL (DL)

The Drude-Lorentz model considers the bound electrons as well as what is taken into account in Drude one. The interband transition of electrons from filled bands to the conduction band plays a crucial role in the optical response. As explained above, alkali metals become transparent when $\omega > \omega_D$ because the transition of electron occurs at this frequencies which provide only small corrections to dielectric constant in the optical domain. In contrast, the others metals (noble metals) do not because the contribution of bound electrons to the dielectric function must be taken into account. Lorentz model described these contributions by adding another term called Lorentzian term $\varepsilon_L(\omega)$ to the Drude dielectric function:

$$\varepsilon_{DL}(\omega) = \varepsilon_D(\omega) + \varepsilon_L(\omega) \quad (2.47)$$

Lorentzian term can be estimate by forced and damped harmonic oscillators. This term is considered as a single oscillator in order to completely describe the permittivity of gold in the optical range compared with the Drude model. The relative dielectric function ε_{DL} is given by:

$$\varepsilon_{DL}(\omega) = \varepsilon_{\infty} - \frac{\omega_D^2}{\omega^2 + i\omega\gamma_D} + \frac{\Delta\varepsilon \Omega_L^2}{(\omega^2 - \Omega_L^2) + i\gamma_L\omega} \quad (2.48)$$

where γ_L and Ω_L represent the spectral width and the strength of the Lorentz oscillator respectively. $\Delta\varepsilon$ is a weighting factor. A. Vial proposed a very accurate algorithm to integrate this analytical model of the permittivity into the FDTD one. Auxilliary Differential Equations (ADE) method is then applied to implement the DL model [103]. Using of the additional Lorentzian term requires the use of the additional intermediate electromagnetic components in the algorithm. Consequently, larger memory space will be needed compared to the case of the Drude model. Meanwhile, multiple oscillators Lorentz terms are generally required to accurately describe the permittivity of noble metals in the optical domain [104].

2.8.3/ DRUDE CRITICAL POINTS (DCP)

In the visible/near-UV region, the contribution of the intraband transitions for some metals become prominent and must be taken into consideration. This can be found in particular in the case of gold. In order to well describe the permittivity metal, more than one Lorentz oscillator must be added to the classical Drude model to estimate these transitions, but the great number of parameters as well as the huge simulation time make this way very hard. To overcome this problem, it is necessary to adopt a reasonable representation of the dielectric function. An innovative method, borrow from parametric critical points model developed for semiconductors, was adapted and implemented in the FDTD algorithm by Vial in 2007 [107]. In fact, this approach is very useful for the description of optical properties of noble metals (gold) for which the electron transition band structure is quite complex. The formula of this model can be well sufficient to describe the optical properties of noble metals. The dielectric function of DCP model is a combination of Drude model and two CP terms:

$$\varepsilon_{DCP}(\omega) = \varepsilon_\infty - \frac{\omega_D^2}{\omega^2 + i\omega\gamma} + \sum_{p=1}^{p=2} G_p(\omega) \quad (2.49)$$

with

$$G_p(\omega) = A_p \Omega_p \left(\frac{e^{i\phi_p}}{\Omega_p - \omega - i\gamma_p} + \frac{e^{-i\phi_p}}{\Omega_p + \omega + i\gamma_p} \right) \quad (2.50)$$

It is clear that the first two terms in Eq. (2.49) correspond to the Drude model, whereas the sum that appears in Eq. (2.50) represents the intraband transition contribution describing by the parameters A_p , Ω_p , ϕ_p and γ_p which are the amplitude, the gap energy divided by Dirac constant, the phase and the broadening of the pole [107] respectively. The validation of the DCP model in our FDTD homemade code was already performed in Ref. [104]. The ADE technique that was used for the DL model is used to handle the DCP one.

2.8.4/ DESCRIPTION OF PERMITTIVITY FOR METALS

In order to accurately implement the dispersive model, we have optimized the parameters for gold and silver metals over a wide spectral range lying from 300 nm to 2000 nm by adjusting them to fit the experimental data of the literature [108]. This optimization is done thanks to a homemade software based on the fitness function Δ as:

$$\Delta = \sum_{\omega} |\varepsilon_{exp}(\omega) - \varepsilon_{model}(\omega)|^2 \quad (2.51)$$

where ω represents the discrete frequency values for which were experimentally calculated permittivities of such metal, ε_{exp} is the tabulated values taken from the literature. Optimized parameters of the three dispersive models described above are given in tables 2.1 and 2.2 for gold and silver respectively. For all models, ε_{∞} is fixed to 1 so that it is not involved in the optimization process. We recognize that this assumption can occasionally (for some other metals) lead to less accurate model. Nevertheless, no negative impact was observed in the case of gold or silver.

Gold	Drude	DL	DCP
ε_{∞}	1.0000	1.0000	1.0000
$\omega_D(s^{-1})$	1.206×10^{16}	1.229×10^{16}	1.234×10^{16}
$\gamma(s^{-1})$	1.312×10^{14}	1.240×10^{14}	1.180×10^{14}
$A_1(\Delta\varepsilon)$		3.6617092	1.921431
$\Omega_1(\Omega_L)(rad \ s^{-1})$		5.935×10^{15}	8.467×10^{14}
$\gamma_1(\gamma_L)(rad \ s^{-1})$		3.134×10^{15}	1.425×10^{15}
$\phi_1(rad)$			-0.785
A_2			1.8570215
$\Omega_2(rad \ s^{-1})$			4.674×10^{15}
$\gamma_2(rad \ s^{-1})$			1.269×10^{15}
$\phi_2(rad)$			-0.785
Δ	12.92	8.66	5.65

Table 2.1: Permittivities of gold for Drude, DL and DCP models are optimized using Δ function over 300 – 2000 nm wavelength range

As may be seen in figure 2.11 and 2.12, there is a good agreement between data of Ref. [109] and the DCP model over the considered spectral range. As it can be shown on figure 2.11, the contribution of the inter-band transition is only taken into account in DL and DCP models. Drude model is then not appropriate in this spectral range (300 – 600 nm). DL and DCP can then be employed over a wider range of wavelengths. Nevertheless, DCP exhibits smaller value of the fitness function and is more suitable. For silver, the same situation is almost seen in figure 2.12, where the permittivity of Ag is

Silver	Drude	DL	DCP
ϵ_∞	1.0000	1.0000	1.0000
$\omega_D(s^{-1})$	1.155×10^{16}	1.154×10^{16}	1.170×10^{16}
$\gamma(s^{-1})$	1.114×10^{14}	8.340×10^{13}	0.9098×10^{14}
$A_1(\Delta\epsilon)$		27.365658	0.2521938
$\Omega_1(\Omega_L)(rad\ s^{-1})$		3.868×10^{15}	6.206×10^{15}
$\gamma_1(\gamma_L)(rad\ s^{-1})$		13.76×10^{16}	4.520×10^{14}
$\phi_1(rad)$			-0.785
A_2			0.9190994
$\Omega_2(rad\ s^{-1})$			1.184×10^{15}
$\gamma_2(rad\ s^{-1})$			3.894×10^{14}
$\phi_2(rad)$			-0.785
Δ	40.63	39.92	12.43

Table 2.2: Permittivities of silver for Drude, DL and DCP models are optimized using Δ function over 300 – 2000 nm wavelength range

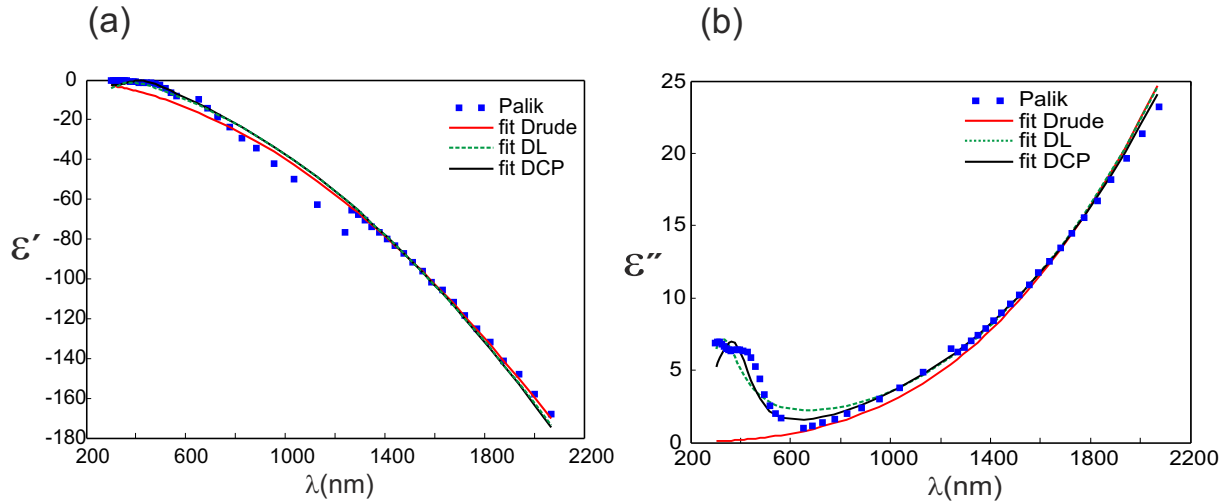


Figure 2.11: Palik data of gold [108] (blue square) and comparison with the fitted permittivities using Drude (solid red curve), DL (dashed green curve) and DCP (solid black curve) models (a) real part (b) imaginary part.

well described in high energy region (300 – 600 nm) using DCP model and its fitness function has also the lower value in comparison with other ones (see in table 2.2). It clearly appears that the improvement in the description of the permittivity using DCP leads us to choose the latter for getting perceptible enhancement in the accuracy of the computation over a wider spectrum.

The following section recalls the background material necessary to construct the technique of total field/scattered field (TF/SF). This technique is useful to determine absorption, extinction and scattering coefficients of any shape NPs.

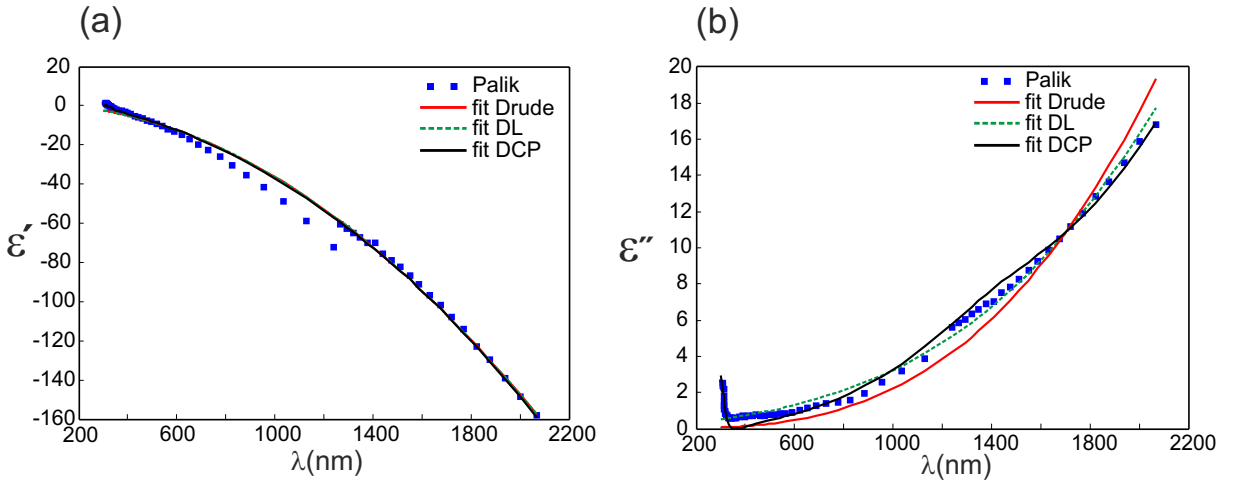


Figure 2.12: Palik data of silver [108] (blue square) and comparison with the fitted permittivities using Drude (solid red curve), DL (dashed green curve) and DC (solid black curve) models (a) real part (b) imaginary part.

2.9/ TOTAL FIELD/SCATTERED FIELD TECHNIQUE (TF/SF)

The TF/SF was firstly described in [110] based on the concept of surfaces of Huygens. As mentioned above, by applying this technique, the absorption (near field), extinction and scattering (far field) spectra from an arbitrary scatterer can be easily calculated. In this section, we verbosely describe the TF/SF techniques in 1D, 2D and 3D and the validation of this technique inside a standard FDTD homemade code as well as the comparison with the corresponding theory will be conducted.

2.9.1/ TF/SF IN ONE-DIMENSIONAL

The figure 2.13 schematically represents the principle of the TF/SF in one-dimensional problem. The computational domain is divided into two zones; total field region and scattered one. The TF zone involves the sum of the incident field and scattered field, whereas only the scattered field exists in the SF zone. By using the property of linearity of Maxwell equations, the total electric and magnetic fields can be written as:

$$\begin{aligned} E_{\text{tot}} &= E_{\text{inc}} + E_{\text{scat}} \\ H_{\text{tot}} &= H_{\text{inc}} + H_{\text{scat}} \end{aligned} \quad (2.52)$$

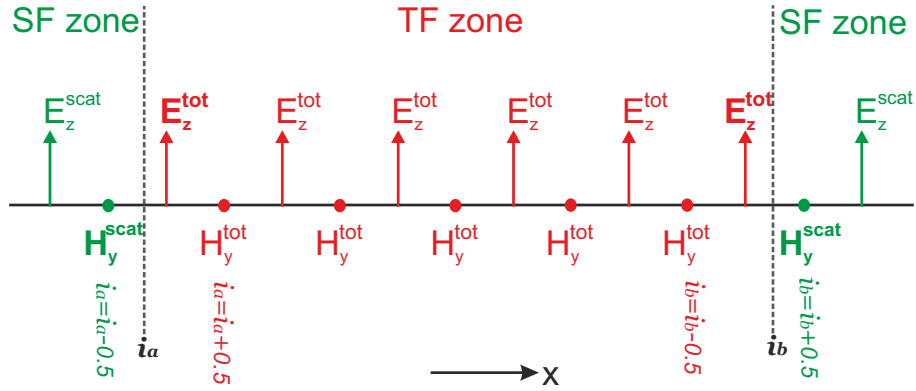


Figure 2.13: Schematic represents the FDTD computational domain including two distinct TF and SF zones in the case of 1D.

Suppose that a uniform plane wave propagates in the $+x$ direction, with the field components E_z and H_y (see Figure 2.13). The FDTD update equations can be derived as previously mentioned in section 2.6 as:

$$E_z|_i^{n+1} = E_z|_i^n - \frac{\Delta t}{\varepsilon \Delta y} [H_y|_{i+1/2}^{n+1/2} - H_y|_{i-1/2}^{n+1/2}] \quad (2.53)$$

$$H_y|_{i+1/2}^{n+1/2} = H_y|_{i+1/2}^{n+1/2} - \frac{\Delta t}{\Delta y} [E_z|_{i+1}^n - E_z|_i^n] \quad (2.54)$$

It is clear that the update equations can be applied to the whole computational domain except at the TF/SF boundaries. At these interfaces, the field components are $E_z|_{i_a}^{n+1}$, $E_z|_{i_b}^{n+1}$, $H_y|_{i_a-1/2}^{n+1/2}$ and $H_y|_{i_a+1/2}^{n+1/2}$. As an example, to determine the E_z in point i_a , we need to subtract the incident field from the total one at each time step through applying the equation 2.53 at TF/SF boundaries. Therefore, the total electric field at i_a can be written as:

$$E_z^{tot}|_{i_a}^{n+1} = E_z^{tot}|_{i_a}^n - \frac{\Delta t}{\varepsilon \Delta y} [H_y^{tot}|_{i_a+1/2}^{n+1/2} - H_y^{scat}|_{i_a-1/2}^{n+1/2}] \quad (2.55)$$

in equation 2.55, there is no consistency due to the appearance of the term H_y^{scat} . This requires that the incident fields only need to be known at the boundary between the total-field region and the scattered-field region. By taking advantage of equation 2.52, the necessary correction have to obtain a consistent update of these electric field nodes by subtracting the incident field from the magnetic total field as is done in the following:

$$E_z^{tot}|_{i_a}^{n+1} = E_z^{tot}|_{i_a}^n - \frac{\Delta t}{\varepsilon \Delta y} [H_y^{tot}|_{i_a+1/2}^{n+1/2} - H_y^{tot}|_{i_a-1/2}^{n+1/2} + H_y^{inc}|_{i_a-1/2}^{n+1/2}] \quad (2.56)$$

equation (2.56) can be expressed in a more compact form as follows:

$$E_z|_{\mathbf{i}_a}^{n+1} = \{E_z|_{\mathbf{i}_a}^{n+1}\} + \frac{\Delta t}{\varepsilon \Delta y} H_y^{inc}|_{\mathbf{i}_a-1/2}^{n+1/2} \quad (2.57)$$

We see in Eq.(2.57) that the field component $\{E_z|_{\mathbf{i}_a}^{n+1}\}$ refers to (Eq.2.53), (i.e. the ordinary FDTD update equation). By the same way, the TF/SF consistency equations can be obtained for the other components, which are given below:

$$E_z|_{\mathbf{i}_b}^{n+1} = \{E_z|_{\mathbf{i}_b}^{n+1}\} - \frac{\Delta t}{\varepsilon \Delta y} H_y^{inc}|_{\mathbf{i}_b+1/2}^{n+1/2} \quad (2.58)$$

$$H_y|_{\mathbf{i}_a-1/2}^{n+1/2} = \{H_y|_{\mathbf{i}_a-1/2}^{n+1/2}\} + \frac{\Delta t}{\Delta y} E_z^{inc}|_{\mathbf{i}_a}^n \quad (2.59)$$

$$H_y|_{\mathbf{i}_b+1/2}^{n+1/2} = \{H_y|_{\mathbf{i}_b+1/2}^{n+1/2}\} - \frac{\Delta t}{\Delta y} E_z^{inc}|_{\mathbf{i}_b}^n \quad (2.60)$$

It becomes clear that the equations (2.53) and (2.54) are in TF and SF zones whereas the equations (2.56–2.60) are to be applied only at the TF/SF boundary. The 1D FDTD code with TF/SF technique was implemented and tested. Nevertheless, the validation of the implementation of this technique will be given in the following for 2D and 3D cases.

2.9.2/ TF/SF IN TWO-DIMENSIONAL

In the problem of two dimensions, the grid is once again divided into a TF zone and a SF zone. The 2D TF/SF is more complicated than 1D TF/SF in the meaning that the incident wave can have arbitrary propagation direction. In our case, we restrict ourselves to TF/SF boundaries which are rectangular. Nonetheless, the implementation details are simplest when the boundary has straight sides. 2D FDTD can be formulated either in *TM* or *TE* polarizations [10]. Figure 2.14 shows a *TM* grid with a rectangular TF/SF boundary. As shown in figure 2.14, we have to know the incident wave component values at E_z the TF/SF boundary and H_y and H_x at grid points just outside it. For example, the electric fields tangential to the TFSF boundary are always in the TF region and hence these nodes will have at least one neighboring magnetic field node that is in the SF region. To obtain a consistent update of these electric field nodes, it is necessary that the correction involves the incident field to correct the values of the neighboring magnetic fields on the outer side of the TFSF boundary. Reciprocally, the magnetic field nodes which are tangential to the TFSF boundary (from the SF zone) must be corrected too. These nodes have one neighboring electric field E_z node which is in TF zone. Consequently, the necessary correction have to obtain a consistent update of these magnetic field nodes by subtracting the incident field from this electric total field. As mentioned in the one dimensional case,

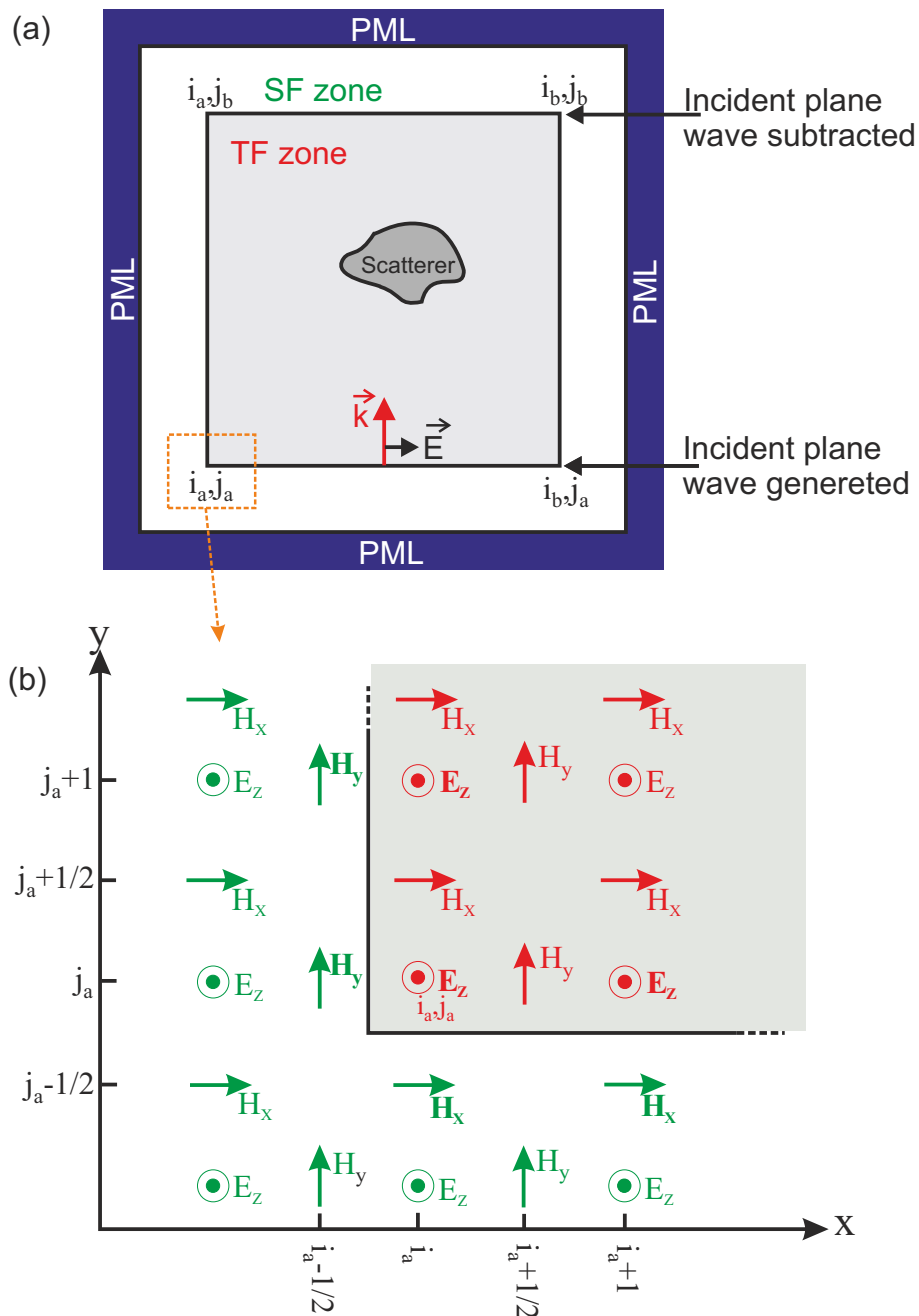


Figure 2.14: Sketch of the simulation for (a) a plan wave hitting a scatterer. The field scattering from the structure is the solitary field in region SF and hit the PML (b) The lower left corner of the FDTD problem space showing the position of nodes for 2D TM_z problem. Note that the bold E and H components indicate the nodes that need to modify the update equations.

to achieve the TF/SF technique, the incident field must be at these specific node and at each time-step. Note that the incident field in TF/SF-FDTD is calculated separately by propagation it inside the homogeneous incident medium.

Generally, the incident beam can propagate along any direction. Nevertheless and for sake of simplicity, we only consider the case where the propagation is in the y -direction. This allows simplifying the field correction at the TF/SF boundary due to a very simple determination of the incident field. In fact, when the propagation direction is along one of the coordinate system axis (here x or y), the schema of incident field updating is reduced to 1D problem. Let us emphasize that this simplification will not limit the validity domain of our FDTD code. In fact, for oblique incidence cases, the illuminated structure is rotated instead of the incident wave itself. In the case of y -propagation incident wave, the formulations of 2D TF/SF-FDTD can be written in a similar way as in 1D TF/SF. In this case, the H_y^{inc} vanishes reducing the corrections the fields at the TF/SF boundaries to:

E_z value at $j = j_a$ and $j = j_b$ for $i \in [i_a, i_b]$:

$$E_z(i, j_a) = E_z(i, j_a) + \frac{\Delta t}{\varepsilon \Delta y} H_x^{inc}(j_a - \frac{1}{2}) \quad (2.61)$$

$$E_z(i, j_b) = E_z(i, j_b) - \frac{\Delta t}{\varepsilon \Delta y} H_x^{inc}(j_b + \frac{1}{2}) \quad (2.62)$$

H_x field only outside $j = j_a$ and $j = j_b$ for $i \in [i_a, i_b]$:

$$H_x(i, j_a - \frac{1}{2}) = H_x(i, j_a - \frac{1}{2}) + \frac{\Delta t}{\Delta y} E_z^{inc}(j_a) \quad (2.63)$$

$$H_x(i, j_b + \frac{1}{2}) = H_x(i, j_b + \frac{1}{2}) - \frac{\Delta t}{\Delta y} E_z^{inc}(j_b) \quad (2.64)$$

H_y field only outside $i = i_a$ and $i = i_b$ for $j \in [j_a, j_b]$:

$$H_y(i_a - \frac{1}{2}, j) = H_y(i_a - \frac{1}{2}, j) - \frac{\Delta t}{\Delta y} E_z^{inc}(j) \quad (2.65)$$

$$H_y(i_b + \frac{1}{2}, j) = H_y(i_b + \frac{1}{2}, j) - \frac{\Delta t}{\Delta y} E_z^{inc}(j) \quad (2.66)$$

2.9.3/ MODEL VALIDATION OF 2D TF/SF

As an illustration, figure (2.15) shows the visualized simulation results obtained in the case of an incident monochromatic plan wave at the wavelength $\lambda = 600$ nm and propagating parallel to the plane xOy axis. In our code FDTD, the computational domain is $(200)^2$ cells with $\Delta x = \Delta y = \lambda/25$ and no scatterer is considered (homogeneous medium). The interface that is represented by the dashed green squares in the computational domain is TF/SF boundaries. The incident wave is TE polarized so that \vec{E} is along the z -direction.

Figures 2.15(a-c) represent the modulus of the electric field in the xOy plane. As shown in Fig. (2.15), there is no scatterer in the computational windows, so there is no visible field in the SF region. We can see in Fig. 2.15(a) initial field is injected from the right side of the TF region. As the field crosses the TF/SF left boundary, a sudden discontinuity occurs due to the fact that the scattered field vanishes. This discontinuity appears both on the left of the TF zone as well as along a portion of the top and bottom of the inner zone, whereas in Fig. 2.15(b) the pulse fills the half of the TF zone. Finally, in figure 2.15(c) the incident wave has faced the right side of the TF zone. Thus, we can verify that without scatterer the field in the SF region is zero even if an initial field is injected into the computational window.

Figure (2.16), shows the modulus of the electric field for the three different time steps as in figure(2.15) but when a dielectric cylinder, with refractive index of $n=2$, is placed into the mesh grid. In figure 2.16(a), the wavefront has just reached the cylinder. It is clear that there is no visible scattering yet meaning a zero field in the SF region. In figure 2.16(b) the interaction of the EM wave with the cylinder takes place. Consequently, a scattered field is generated but it only exists inside the TF zone. Interferences between the incident and the scattered fields occurs especially in front of the cylinder where reflection is efficient. Later, in figure 2.16(c), the non-zero field in the SF zone corresponds to the propagation of the scattered field from the TF zone into the SF one. The PML ABC ensures the non reflection of the scattered field on the computational window borders as it can be seen from figure 2.16(c).

2.9.4/ TF/SF DEMONSTRATION IN THREE-DIMENSIONAL

We have seen in the previous section, the implementation of the TF/SF method in 2D in the case of TM-polarization. In the case of 3-D TF/SF FDTD, the update of the equations also depends on the type of source used in the simulation. To better understand, we introduce the simplest case when a linearly polarized plane wave along the y -direction is considered propagating in the z -direction. In this case, the plane wave has only two non-zero components of the incident field E_y^{inc} and H_x^{inc} (see Fig. 2.17). Furthermore, it is necessary to determine the E and H nodes that are tangential to the TF/SF interface and their neighboring nodes that are on the other side of TF/SF boundary. The update of E and H will be done through the adding or subtracting of the incident field from the neighboring node in order to get consistent equations.

To illustrate the construction, the incident field could be injected on the TF/SF inter-

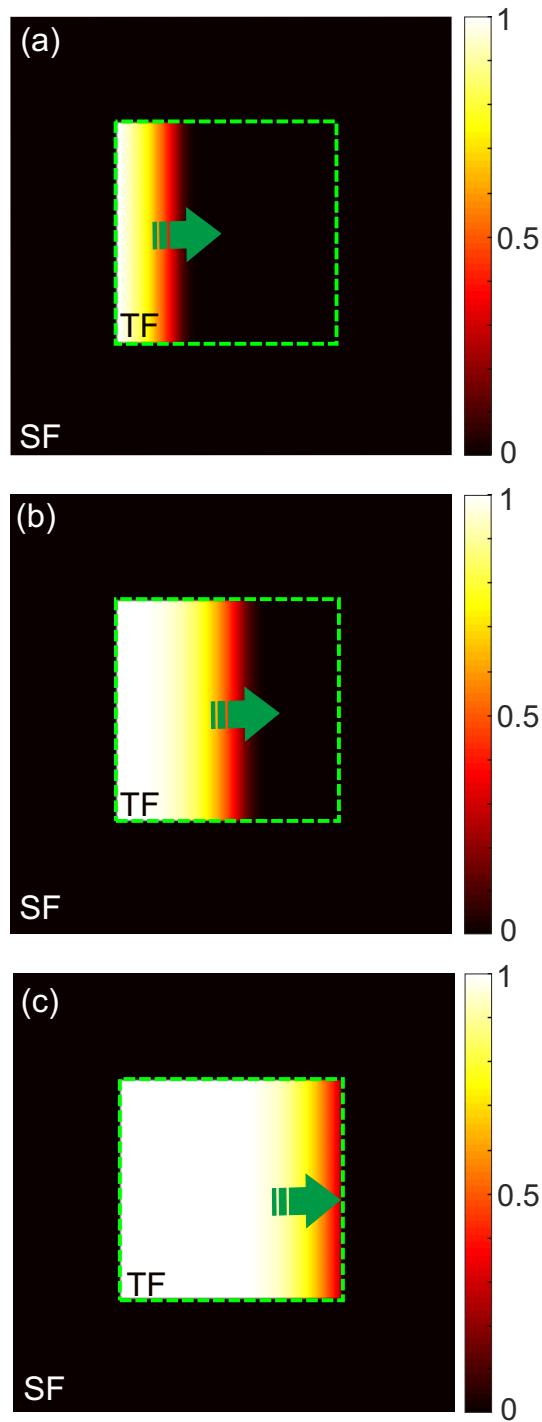


Figure 2.15: E_z field in a computational domain using a TF/SF technique. The modulus of the electric field in xOy plane are taken at time-steps (a) 120, (b) 180, and (c) 270. Note that the $dt = 4.0028 \times 10^{-17}$ s.

face. Moreover, whatever the type of source (incident field), the description of this field at the TF/SF interface should be taken into account and hence should be compatible with the usual behavior of the field in the full grid. The TF/SF boundary has six planes

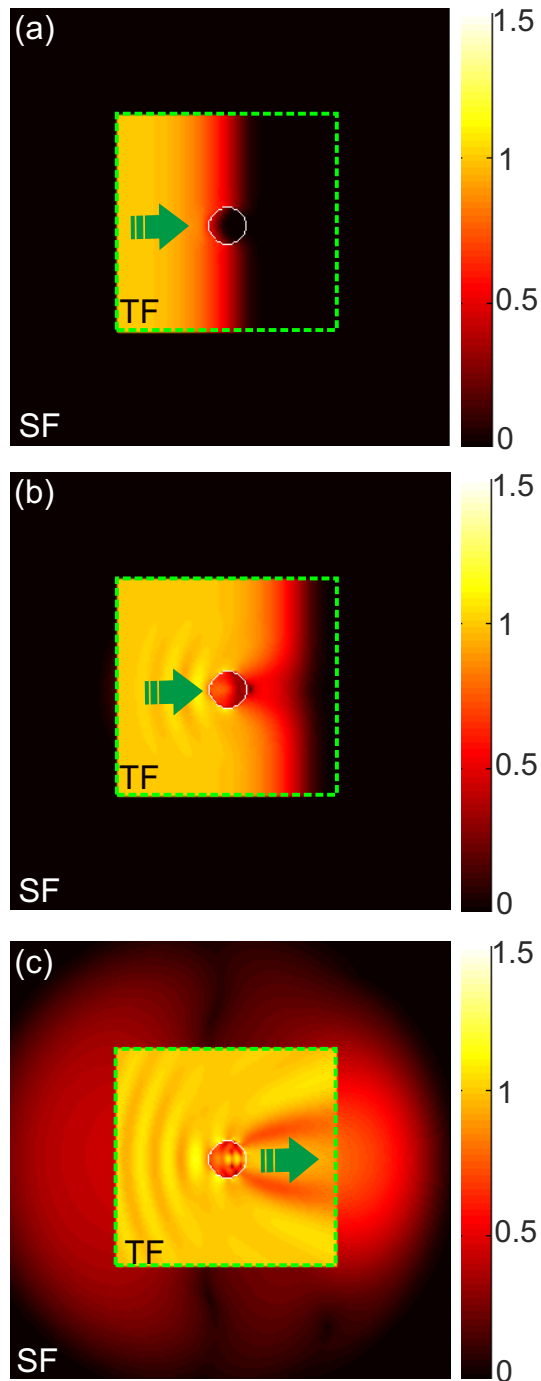


Figure 2.16: E_z field with dielectric cylinder ($n_s = 2$ in a computational domain using a TF/SF technique. The modulus of the electric field in xOy plane are taken at time-steps (a) 180, (b) 240, and (c) 360. $dt = 4.0028 \times 10^{-17}$.

and each one has two components of electric and magnetic fields which are tangential to TF/SF interface. These components should be modified over the TF/SF interface. For this purpose, let us write these consistent equations over the six faces of the parallelepiped that corresponds to the frontier between TF and SF regions according to the notions of

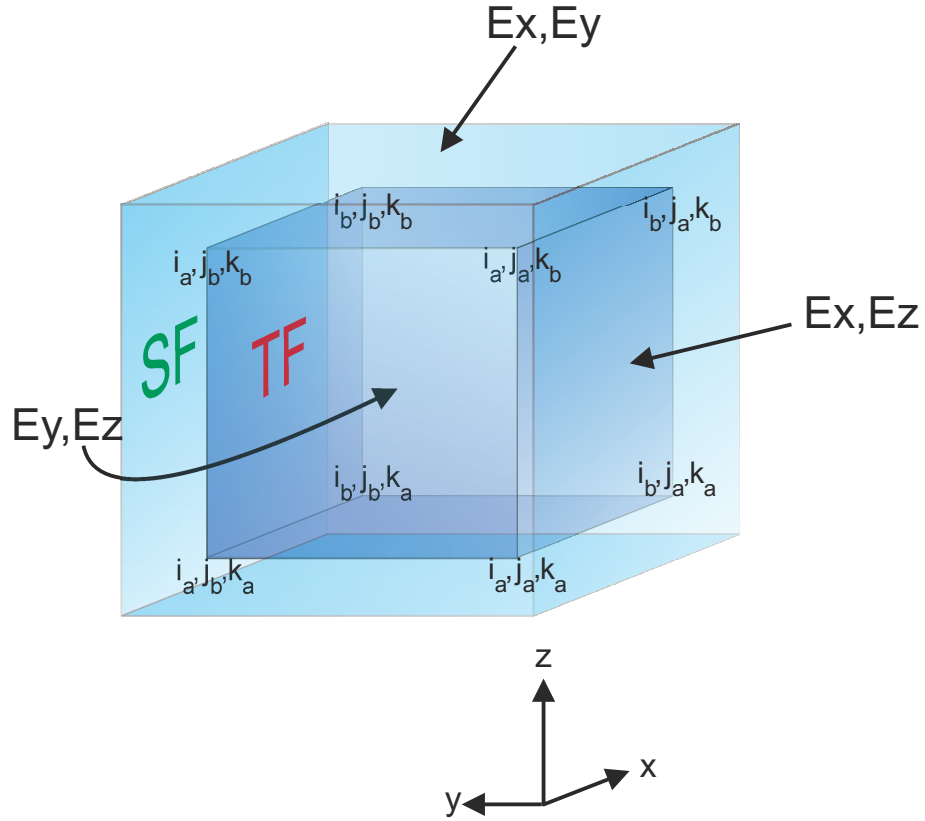


Figure 2.17: 3 – D computational domain which contains a TF/SF boundary ($\mathbf{i}_a, \mathbf{j}_a, \mathbf{k}_a, \mathbf{i}_b, \mathbf{j}_b$ and \mathbf{k}_b) and the nodes that are used in the corrections.

figure 2.17 and taken into account the interleaving between E and H spatial positions:

in $x - z$ plane, E_z value at $\mathbf{j} = \mathbf{j}_a$ and $\mathbf{j} = \mathbf{j}_b$ for $i \in [i_a, i_b]$ and for $k \in [k_a, k_b]$:

$$E_z(i, \mathbf{j}_a, k) = E_z(i, \mathbf{j}_a, k) + \frac{\Delta t}{\epsilon \Delta} H_x^{inc}(\mathbf{j}_a - \frac{1}{2}) \quad (2.67)$$

$$E_z(i, \mathbf{j}_b, k) = E_z(i, \mathbf{j}_b, k) - \frac{\Delta t}{\epsilon \Delta} H_x^{inc}(\mathbf{j}_b + \frac{1}{2}) \quad (2.68)$$

in $x - y$ plane, E_y value at $\mathbf{k} = \mathbf{k}_a$ and $\mathbf{k} = \mathbf{k}_b$ for $i \in [i_a, i_b]$ and for $j \in [j_a, j_b]$:

$$E_y(i, j, \mathbf{k}_a) = E_y(i, j, \mathbf{k}_a) - \frac{\Delta t}{\epsilon \Delta} H_x^{inc}(\mathbf{k}_a - \frac{1}{2}) \quad (2.69)$$

$$E_y(i, j, \mathbf{k}_b) = E_y(i, j, \mathbf{k}_b) + \frac{\Delta t}{\epsilon \Delta} H_x^{inc}(\mathbf{k}_b + \frac{1}{2}) \quad (2.70)$$

Now we write the H field

in $x - y$ plane, H_x value at $\mathbf{k} = \mathbf{k}_a - \frac{1}{2}$ and $\mathbf{k} = \mathbf{k}_b + \frac{1}{2}$ for $i \in [i_a, i_b]$ and for $j \in [j_a, j_b]$

:

$$H_x(i, j, \mathbf{k}_a - \frac{1}{2}) = H_x(i, j, \mathbf{k}_a - \frac{1}{2}) - \frac{\Delta t}{\Delta} E_y^{inc}(\mathbf{k}_a) \quad (2.71)$$

$$H_x(i, j, \mathbf{k}_b + \frac{1}{2}) = H_x(i, j, \mathbf{k}_b + \frac{1}{2}) + \frac{\Delta t}{\Delta} E_y^{inc}(\mathbf{k}_b) \quad (2.72)$$

in x – y plane, H_y value at $\mathbf{i} = \mathbf{i}_a - \frac{1}{2}$ and $\mathbf{i} = \mathbf{i}_b + \frac{1}{2}$ for $i \in [j_a, j_b]$ and for $k \in [k_a, k_b]$:

$$H_y(\mathbf{i}_a - \frac{1}{2}, j, k) = H_y(\mathbf{i}_a - \frac{1}{2}, j, k) + \frac{\Delta t}{\Delta} E_y^{inc}(\mathbf{i}_a) \quad (2.73)$$

$$H_y(\mathbf{i}_b + \frac{1}{2}, j, k) = H_y(\mathbf{i}_b + \frac{1}{2}, j, k) - \frac{\Delta t}{\Delta y} E_y^{inc}(\mathbf{i}_b) \quad (2.74)$$

For the two remaining faces, there is no need to correct the EM field because the involved components are always null. To validate our 3-D TF/SF FDTD code, we will model in next section, nanosphere taking advantage of this method to calculate its scattering efficiency and compare it to the one obtained by Mie theory.

2.10/ MODELING THE OPTICAL RESPONSE: FDTD-TF/SF VALIDATION

Even if any geometrical shape (nanosphere, nanotubes, nanoelliptical beads, nanoshells and also nanoantenna ...etc) can be considered in the FDTD code, we will start by studying the light scattering by spheres in order to validate our code.

2.10.1/ FRAMEWORK OF SCATTERING OF LIGHT

In order to illustrate the calculation of the scattered and absorption energies, let's look at what would happen when a nanoparticle is illuminated by an EM wave.

To better describe the problem, it is convenient to define the total field as the sum of incident and scattered fields. Thus, if one notes that \mathbf{E}_{sca} and \mathbf{H}_{sca} as the scattered electric field and scattered magnetic field respectively and \mathbf{E}_{inc} and \mathbf{H}_{inc} as the incident field, then the total field outside of the particles corresponds to the superposition of these two fields. The latter is already written in equation 2.52. The elastic interaction between the particle and the incident field will induce the scattering to occur in all directions. As shown in Fig.2.18, one can see that the conservation of energy for the problem can be

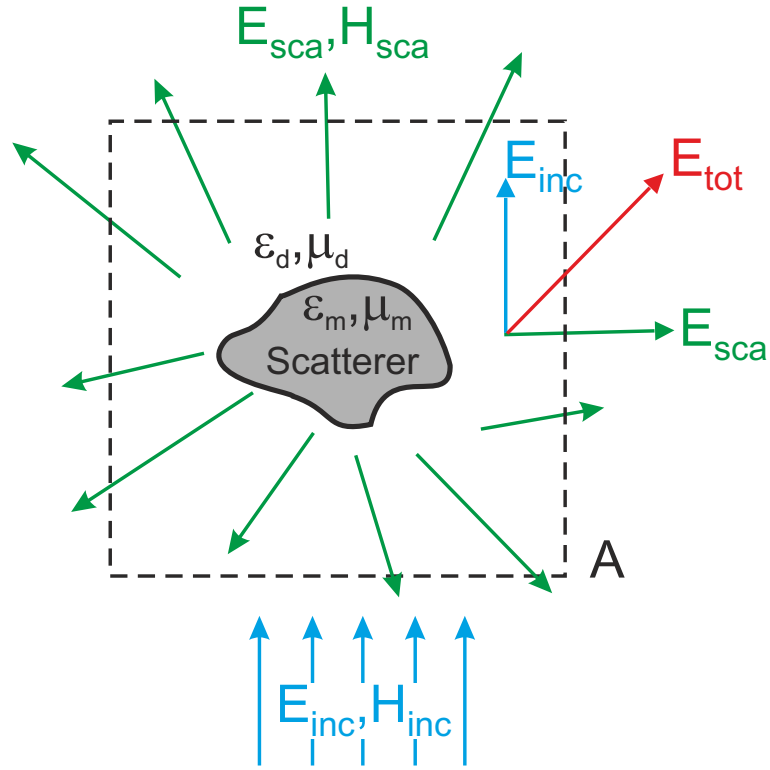


Figure 2.18: Sketch showing an arbitrary particle illuminated with plane wave, a part of incident light is scattered by the particle. Note that electromagnetic fields E_{tot} , H_{tot} decompose of incident and scattered components.

expressed by:

$$\vec{\mathbf{P}}_{ext} = \vec{\mathbf{P}}_{abs} + \vec{\mathbf{P}}_{sca} \quad (2.75)$$

where $\vec{\mathbf{P}}_{abs} = \frac{1}{2} \Re(\vec{\mathbf{E}}_{abs} \times \vec{\mathbf{H}}_{abs}^*)$ and $\vec{\mathbf{P}}_{sca} = \frac{1}{2} \Re(\vec{\mathbf{E}}_{sca} \times \vec{\mathbf{H}}_{sca}^*)$ are the time-averaged Poynting vector obtained by the electromagnetic fields absorbed and scattered by the particle respectively. whereas $\vec{\mathbf{P}}_{ext} = \frac{1}{2} \Re(\vec{\mathbf{E}}_{inc} \times \vec{\mathbf{H}}_{sca}^* + \vec{\mathbf{E}}_{sca} \times \vec{\mathbf{H}}_{inc}^*)$ denotes the power emerging due to the superposition of the incident and scattered fields.

As seen in figure 2.18, for any auxiliary closed surface A including the target, we can obtain a simple relation of different energies by integrating the Poynting vectors over this surface. If we consider that the general case is without loss (surrounding medium is pure dielectric), then the incoming light is a plane wave giving $\int_A P_{inc} dA = 0$. Therefore, the

power scattered and absorbed by the particle are:

$$W_{sca} = \int_A P_{sca} dA \quad (2.76)$$

$$W_{abs} = - \int_A P_{tot} dA \quad (2.77)$$

One can see that W_{abs} in Eq. 2.77 is a link between the total and absorbed energies. In fact, the surrounding medium in our case is lossless, while the imaginary part of epsilon $\Im\epsilon > 0$. Let notice that the minus sign that appears in the W_{abs} expression is due to the fact that the normal vector to the A surface is taken along the outgoing direction.

As previously explained, the extinction term corresponds what is lost by the incident beam by both scattering and absorption. The scattering and absorption cross-sections can be defined as:

$$\sigma_{sca} = \frac{W_{sca}}{P_{inc}} \quad (2.78)$$

$$\sigma_{abs} = \frac{W_{abs}}{P_{inc}} \quad (2.79)$$

where $P_{inc} = \frac{1}{2} c \epsilon_o \sqrt{\epsilon_m} |E_o|^2$ is the power flow per unit area supported by a plane wave of the form $\vec{E}_{inc} = E_o e^{-i(\omega t - \vec{k} \cdot \vec{r})}$, where k is the wave vector the incident medium $k = \frac{2\pi}{\lambda} \sqrt{\epsilon_m}$. The extinction cross-section then can be deduced from the energy conservation as:

$$\sigma_{ext} = \frac{W_{ext}}{P_{inc}} = \sigma_{sca} + \sigma_{abs} \quad (2.80)$$

It is also appropriate, to define Q which is the efficiency that can be obtained by normalizing the cross-section σ to the physical cross-sectional area of the target projected onto a plane perpendicular to the direction of illumination.

Numerically, by applying the TF/SF FDTD technique, it can be possible to directly access to the total energy P_{tot} that is calculated inside the total zone. According to equation 2.77, the flux of this quantity through an enclosed surface A located in the TF zone directly leads to the absorbed power (P_{abs}). Similarly, the scattered power P_{sca} is determined by applying the same calculation but in the SF zone. Knowing the incident power that is deduced from the expression of the injected incident field, scattering and absorption coefficients can be easily determined. In our case, and for seek of simplicity, the two enclosed surfaces consist on two parallelepipedic boxes surrounding the target, one in the TF zone and the other in the SF zone. By the way, totally, we need to integrate the Poynting vector over 12 planar faces. Note that, the Fourier transform of the E and H fields

needed for the calculation of the Poynting vector, should be done simultaneously when updating them through the FDTD algorithm in order to avoid a very huge data storage.

2.10.2/ COMPARISON NUMERICAL RESULT WITH ANALYTIC RESULT

In order to validate our approach we calculate the optical response of aluminum nanosphere and with radius $R = 60 \text{ nm}$ (see Fig.2.19) and compare the obtained efficiencies from TF/SF-FDTD code with the analytical Mie theory. In the computational domain, the value of the grid size is set to $\Delta x = \Delta y = \Delta z = 5 \text{ nm}$ and the time-step was $8.34 \times 10^{-18} \text{ s}$. 10 grid cells are used as a PML all around the computational windows that has $1 \times 1 \times 1 \mu\text{m}^3$ volume. The sphere is illuminated by linearly polarized incident plane wave propagating along z -axis and polarized along y -axis. The dielectric function integrated in our FDTD code is a simple Drude model that was adapted to the wavelength $\lambda = 344.4 \text{ nm}$ has been extracted from Palik et al [109]. The scattering cross-section is calculated over 300 nm to 800 nm wavelength range.

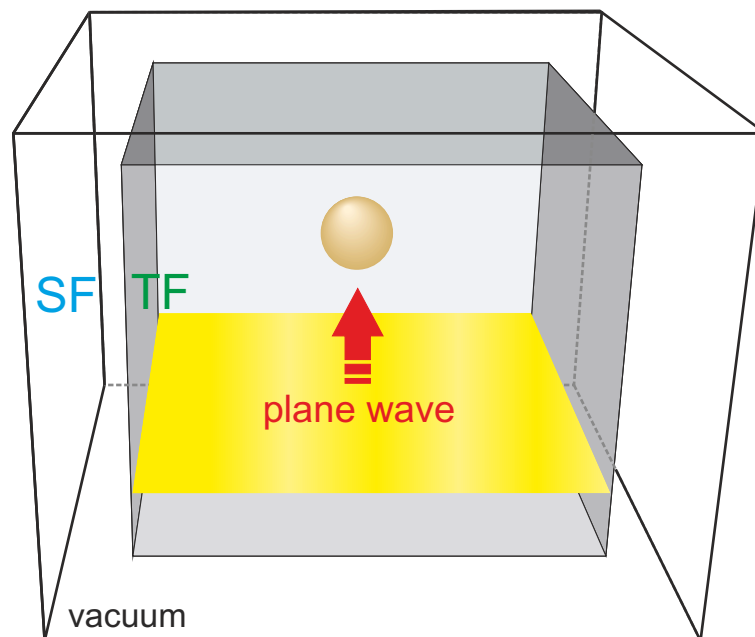


Figure 2.19: Computational domain in the case of a metal sphere which contains a TF/SF boundary .

Figure 2.20 shows a comparison between the FDTD result (red line) and the theoretical one calculated by Mie theory (blue line). Unfortunately, the results do not agree very well because of the errors that arise from numerical source such as the mesh size that induces staircasing close to the sphere surface. This problem may occur for any type

of curved surfaces. To overcome this problem, the simplest idea is to reduce the size of spatial cell size. However, there are drawbacks to work with thinner meshing. In fact, when the spatial size is reduced by a factor x , the required memory grows as x^3 and the total time-step also increases by a factor x due to the stability criterion given in Eq. (2.42). This results by increasing the total simulation CPU-time by a factor of x^4 . For example, when $x = 2.5$ and a total volume of $1 \mu m^3$, the CPU-time needed to make one FDTD simulation grows from 2 hours ($\Delta x = 5 \text{ nm}$) to 70 hours ($\Delta x = 2 \text{ nm}$) which almost corresponds to an increasing by a factor $2.5^4 = 39$. To avoid such huge FDTD simulations, we integrate the Contour Path Technique (CPT) into our FDTD code. This technique is dedicated to enhance the description of curved surface when meshed by rectangular grid.

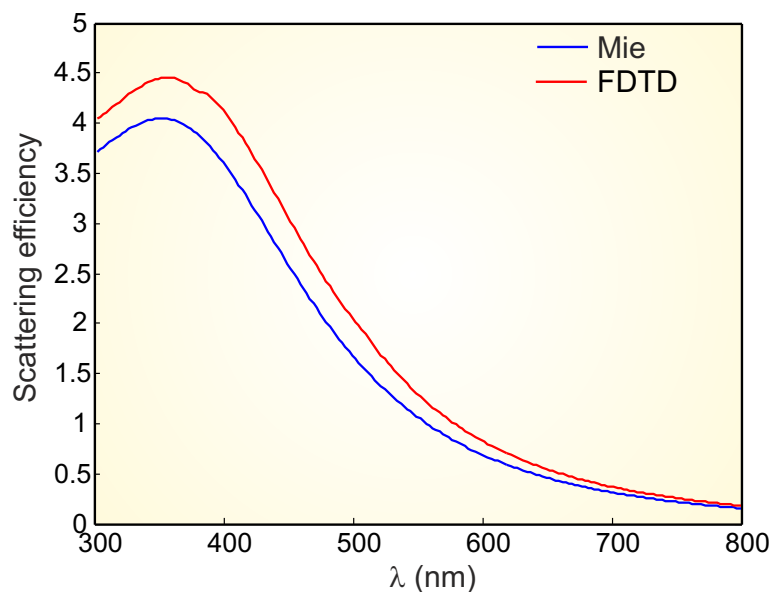


Figure 2.20: Scattering efficiency of aluminum nanosphere with radius ($R = 60 \text{ nm}$) and grid size ($\Delta = 5 \text{ nm}$) is calculated with FDTD (solid blue curve) and Mie (solid red curve). The target is illuminated by plane wave in a vacuum.

2.11/ CONTOUR PATH TECHNIQUE (CPT)

Modeling some objects in FDTD code requires to be well described within the simulation window. The use of a structured uniform mesh makes such objects (see Fig. 2.21(a)) are not described with high spatial resolution. In the literature, different techniques have been developed in order to minimize the staircasing problem in such object with curved surface. These techniques are, for example, the unstructured grids technique [10, 111] or sub Cartesian grids [10, 112], and the CPT one that will be the focus of our attention

in our work.

The principle of CPT was proposed by Yu, Mittra and Dey [113, 114, 115] to describe the objects that have curved surfaces with a structured mesh. The significance of the staircasing error in a conventional FDTD becomes clear when dealing with curved interfaces between two dissimilar dielectrics. Into each cell of Yee (see figure 2.8) crossed by a virtual surface of such object, it is necessary to determine, at each edge of the cell, what proportion is inside the cell, and what proportion is outside. In order to well address this technique, we give below an example of a two-dimensional case (for simplify) that describe the CPT. In figure 2.21(b), shows an object and their intersection between a curved surface and the Yee cell (i.e. there are ε_1 and ε_2). The electric field $E_x(i + \frac{1}{2}, j + 1)$ update algorithm remains unchanged outside of the object (completely in the medium 2) and can be calculated in the usual manner. On the other hand, the edge that has the electric field $E_x(i + \frac{1}{2}, j)$ is intersected by the surface of the object. In this case, we know the intersections of the grid lines with the object surface and hence can distinguish between the medium 1 and medium 2.

In order to determine the electric field $E_x(i + \frac{1}{2}, j)$ at the point of intersection, it must be taken into account the contributions of these two mediums. This effect can be write using the ratios $\frac{\delta x}{\Delta x}$ and $\frac{1-\delta x}{\Delta x}$ as:

$$E_x(i + \frac{1}{2}, j) = \frac{\delta x}{\Delta x} E_x^1(i + \frac{1}{2}, j) + \frac{1 - \delta x}{\Delta x} E_x^2(i + \frac{1}{2}, j) \quad (2.81)$$

where E_x^1 is calculated into medium 1, whereas E_x^2 is calculated into medium 2. Therefore, E_x^1 and E_x^2 must be calculated separately at the object/medium border, and hence must be stored during the calculation FDTD. It is possible to work directly with E_x without using these intermediates fields in the case of non-dispersive dielectric object. In this case, the geometry of the problem is directly described by the dielectric matrix ε . The ratios outside and inside the object, can then be integrated to the same dielectric matrix. By taking the previous example, this technique allows to obtain the eigen dielectric matrix ε to the electric field component

$$\varepsilon_x(i + \frac{1}{2}, j) = \frac{\delta x}{\Delta x} \varepsilon_1 + \frac{1 - \delta x}{\Delta x} \varepsilon_2 \quad (2.82)$$

where ε_1 and ε_2 are the dielectric constants of the object and the surrounding medium respectively. The same work is to be done for E_y and E_z components which would require the introduction of the dielectric matrices ε_y and ε_z . This matrix corresponds to three planes sections passing through the center of a such object in the case of 3D.

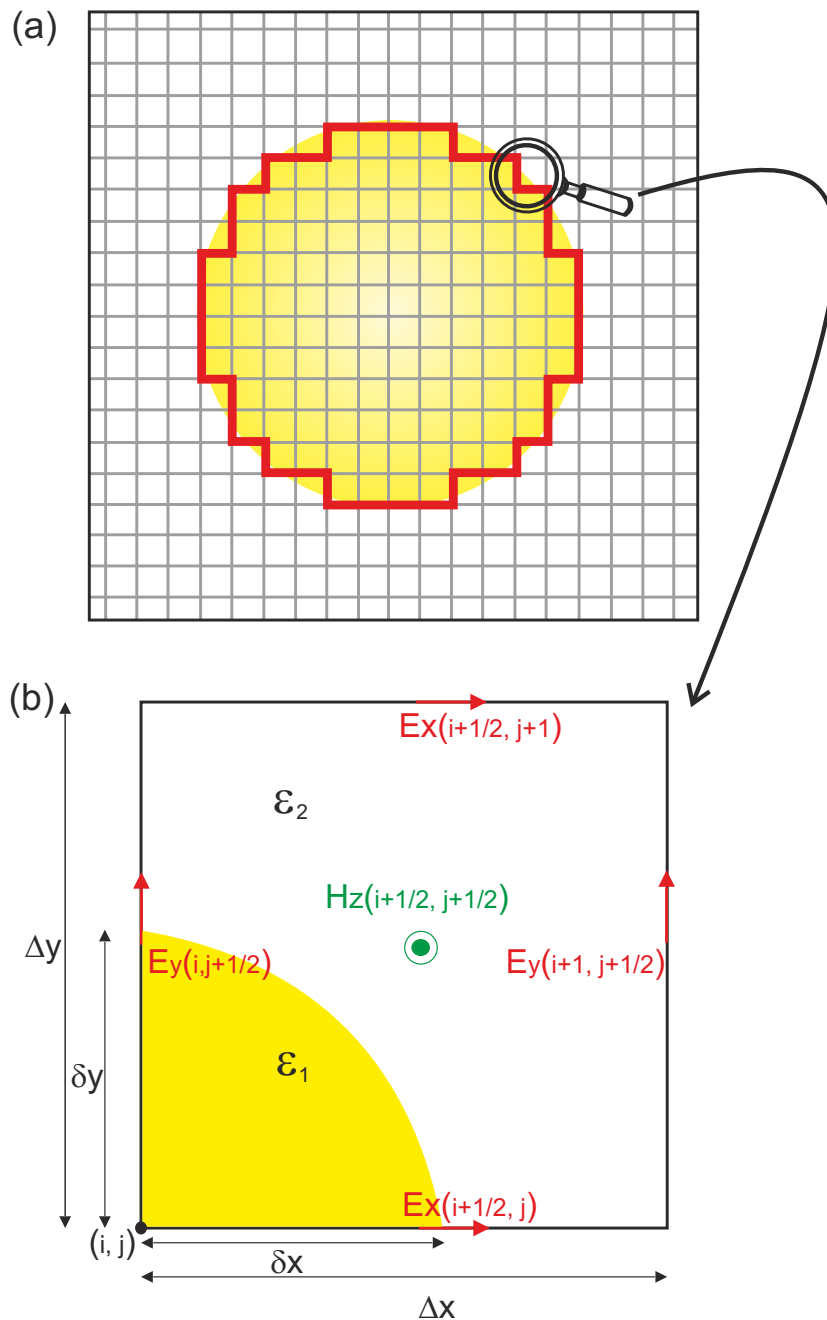


Figure 2.21: (a) Scheme illustrates the defects resulting from using a uniform structured mesh in the case of a sphere. (b) Zoom for a 2D cell Yee in (b) shows the principle of the CPT.

Fig. 2.22 gives an example of the results obtained in the case of a nano-cylinder made of glass, placed in a vacuum with radius of 60 nm and mesh size 5 nm . As shown in Fig. 2.22(a), introduces significant staircasing because the CPT was not applied. On the other hand, figure 2.22(b), shows a clear reducing of the staircasing around the circumference of the cylinder by using CPT.

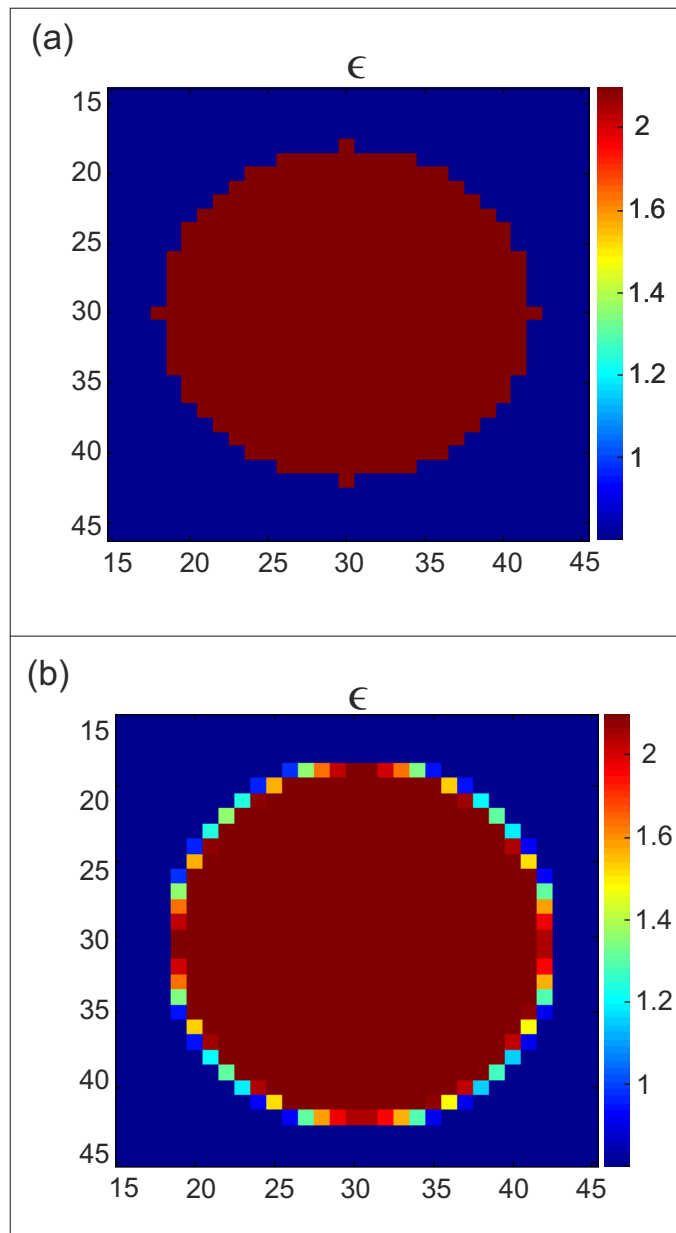


Figure 2.22: Meshing of a 2D nano-cylinder made of glass placed in air (a) staircase, (b) CPT.

In next section, the numerical test of CPT against Mie theory will be conducted through modeling a three-dimensional case (sphere).

2.11.1/ IMPLEMENTATION OF CPT IN FDTD CODE

To illustrate both the accuracy and the stability of CPT-FDTD code, several simulations are performed through calculating the scattering efficiency of an aluminum sphere with

2.11. CONTOUR PATH TECHNIQUE (CPT)

$R = 60 \text{ nm}$, with background index ($n_m = 1$). On the other hand, our numerical results for both code (conventional FDTD and CPT-FDTD) are compared with the exact ones (Mie solutions). The optical constants of aluminum have fitted to a Drude model [108] with the parameters: $\varepsilon_\infty = 1$, $\omega_p = 1.9731 \times 10^{16} \text{ rad/s}$ and $\gamma = 2.1981 \times 10^{14} \text{ rad/s}$. In fact, Drude model has a good approximation for aluminum in the optical domain [102]. Moreover, our aim is focused on comparing the numerical results with those of Mie solution no more. The TF/SF technique is also applied to compute the scattering efficiency of the object under study. The scattering efficiency is calculated for different values of mesh size, figure 2.23(a) shows the result with two values of grid size $\Delta = 5 \text{ nm}$ and $\Delta = 2 \text{ nm}$.

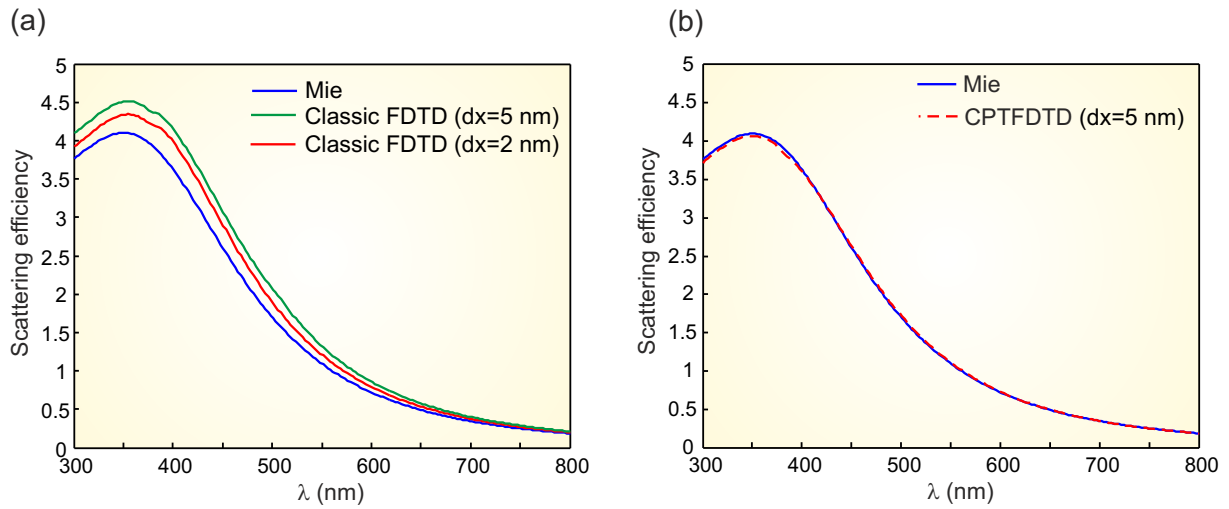


Figure 2.23: Scattering efficiency of nanosphere made in aluminum with radius ($R = 60 \text{ nm}$) is calculated using (a) Classic FDTD code for two values of mesh size $\Delta = 5 \text{ nm}$ (solid green curve) and $\Delta = 2 \text{ nm}$ (solid red curve). (b) CPT-FDTD (dashed red curve) compared with Mie (solid blue curve). The target is illuminated by a plane wave in a vacuum.

The result of CPT-FDTD with mesh size $\Delta = 5 \text{ nm}$ exhibits a high accuracy and agree very well with the Mie solution. The absolute relative error between CPT and Mie calculation is ~ 0.0074 , indicating that the CPT is largely reduced the errors in compare with the FDTD code without CPT (see table 2.3). In contrast, the numerical results of the classic FDTD (staircasing) have much more errors as confirmed in figures 2.23 and 2.24. It is clear from these latter that scattering efficiency calculated by classical code depends on mesh size. Regarding to computational resources, the mesh grid ($\Delta = 5 \text{ nm}$) in CPT-FDTD code requires 7.6 GB of ram and takes ~ 5 CPU hours to complete on a 200^3 cell. On the other hand, the mesh size ($\Delta = 2 \text{ nm}$) in a classic code (i.e. without CPT) uses 47.73 GB of ram and needs ~ 70 CPU hours to finish on a 500^3 cell. In fact, it would have been better to perform another calculation with finer resolution in order to get

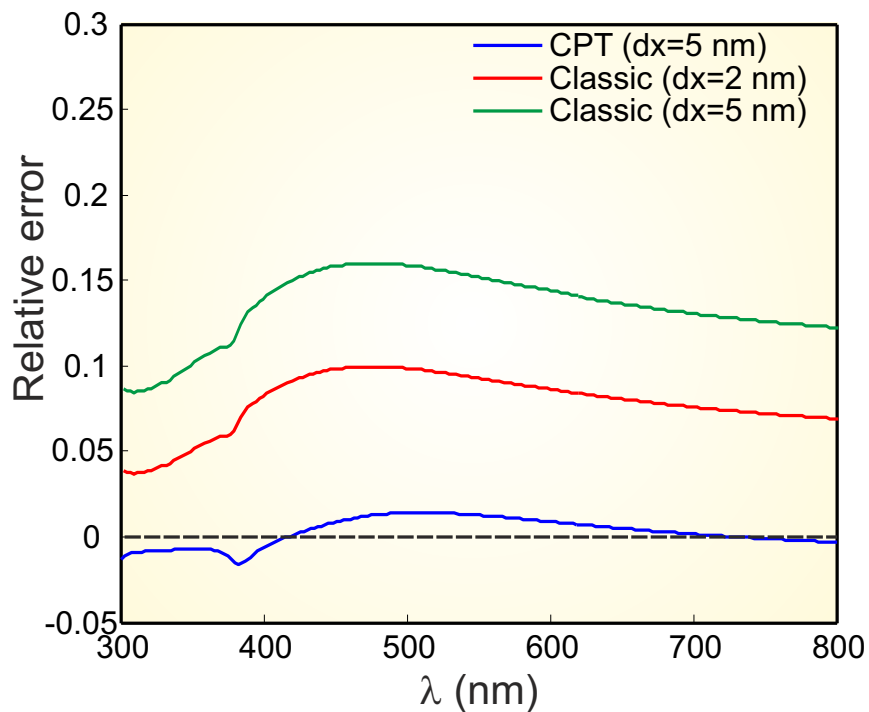


Figure 2.24: Relative error on the scattering efficiency calculated by both FDTD and Mie. The FDTD calculation without CPT technique has two values of mesh size $\Delta = 5 \text{ nm}$ (solid green curve) and $\Delta = 2 \text{ nm}$ (solid red curve). The solid blue curve represents CPT one.

the same curve as in CPT. Unfortunately, it was not possible to reach a value of grid less than 2 nm due to the lack of necessary resources in our laboratory.

Technique used	CPU (hour)	Ram(GB)	# cells	relative error
Classic, mesh size ($\Delta = 5 \text{ nm}$)	01:58	4.1	8 000000	0.1018
Classic, mesh size ($\Delta = 2 \text{ nm}$)	70:10	47.7	64 000000	0.0605
CPT, mesh size ($\Delta = 5 \text{ nm}$)	05:12	7.6	8 000000	0.0074

Table 2.3: The accuracy of both CPT-FDTD and classic FDTD used in the calculation of the scattering efficiency with different values of mesh size.

In general, the numerical results reveal that CPT-FDTD is better than the classic one due to the two advantage main reasons: getting a high precision in particular when the CPT is applied to study the optical response of metallo-dielectric NPs, the second important factor is to reduce the expenses of resources (memory and time of computational).

2.12/ ABSORPTION, SCATTERING AND EXTINCTION PROPERTIES OF BOWTIE AND DIABOLO NANO-ANTENNAS

In the previous section, the FDTD method is presented and validated as a computational tool to model the optical properties of nanostructures. In general, this method is quite adaptable for any geometry of the target. In this present section, we employ our FDTD code to calculate the scattering, absorption and extinction efficiencies for metallic nanoantenna exhibiting very interesting optical properties. Two kinds of NA are considered: the bowtie and the diabolo NAs. A parametric study is performed where all geometrical parameters and metal nature are varied. In fact, these structures exhibit tunability of the resonance wavelength leading to large local field enhancement in the vicinity of the NA making it a good candidate for many applications.

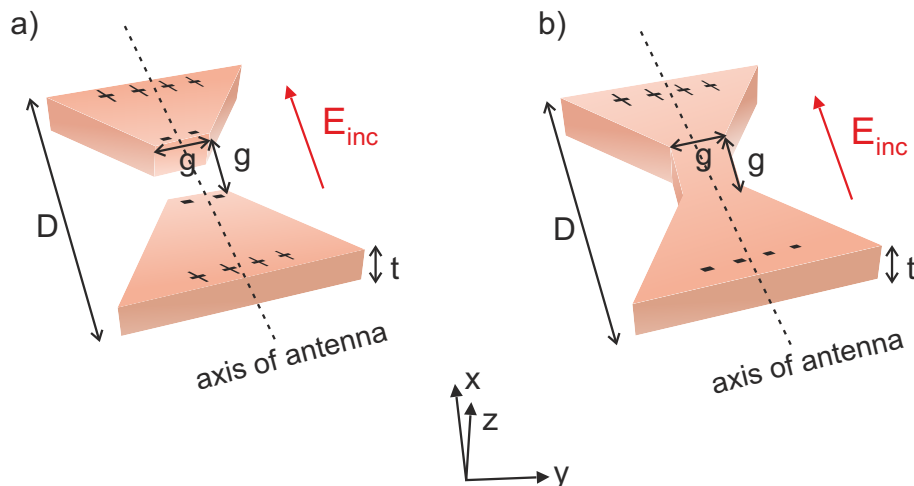


Figure 2.25: Schema showing 3D view of two different nanoantenna configurations (a) bowtie nanoantenna and (b) diabolo nanoantenna under study having the same values of geometric parameters, thickness t , gap g and length D . For both NAs, we consider an incident field with a polarization along its long axis. Note that both NAs are immersed in water.

In present days most of applications require structures or devices operating with high efficiency to minimize the needed power. Therefore, the optimization or the modification of the design is one of the challenges in the optical domain. In the context of LSPR, an important point is the tailoring of the shape and dimensions of metal NPs. This task can be performed through the exploitation of our code based on the TF/SF FDTD technique. We started our study with a comparison between the optical responses of a bowtie and a diabolo NAs with the same geometrical of parameters. We will see from this comparison, how the information supported by optical properties from such structures can

produce an efficient enhancement of electromagnetic field. The electromagnetic energy localized onto these structures is directly linked to the effective cross section of the NA. This work is a contribution to the ongoing discussions about optical responses, not only for nanoantennas but also from any NPs.

Figure 2.25 presents scheme of the two different optical nanoantennas. The first one, called Bowtie nanoantenna (BA), consists of two metallic triangles separated by a small gap [78] (see figure 2.25(a)). Whereas the other one, known as Diabolo nanoantenna (DA), has a similar geometric shape but its gap is filled with metal as narrow waist [18] (see figure 2.25(b)). All the results are carried out through FDTD numerical calculations where the DCP model is adapted to describe the dielectric constant of the considered metals. Our simulations are performed to determine the optical (scattering, absorption and extinction) efficiencies of each NA.

The two NAs presented in figure 2.25 are first supposed to be made in silver and placed in water as host medium. These two targets are separately excited by a plane wave polarized along the axis of the antennas (see figure 2.25). The calculated absorption, scattering and extinction efficiencies, are presented in figure 2.26(a). It can be shown that at the resonance, the effective NA area (i.e. virtual section interacting with light) can reach 38 times its actual area in the case of the DA while only a factor of 10 is obtained for the BA. This result demonstrates a very large amount of scattering of the DA compared to bowtie one. Figure 2.26 shows a DA resonance peak at $\lambda_{res} = 1322 \text{ nm}$, while the bowtie resonates at higher energy with lower amount as well. On the other hand, it is clear that, for both cases presented in this figure, the significant part of the incident energy is scattered, whereas the absorption exhibits a modest contribution of the total efficiency (i.e. the extinction). Let us emphasize that the amount of the energy absorption in DA is larger than those in BA one. The ratio of the absorption efficiency to extinction one (see the definitions of these two quantities on page 44) $\Gamma = \frac{Q_{abs}}{Q_{ext}}$ for both DA and BA is calculated and found to be $\Gamma_{DA} = 0.243$ and $\Gamma_{BA} = 0.213$. Besides, the intensity distribution of electric and magnetic fields is separately calculated in xOy plane in the vicinity of DA and BA and at their resonance wavelengths. Figure 2.26 shows the electric and magnetic distribution in BA (b,c) and DA (d,e) respectively. In figure 2.26(e), a better localization of the magnetic field occurs inside the metallic gap of DA with less electric field enhancement at the corners (see figure 2.26(d)). Whereas for BA, a prominent electric intensity but with low factor can be seen in dielectric gap and the external edges with insignificant magnetic intensity (see figure 2.26(b,c)). As a result, one can deduce that the DA has a larger volume mode compared to BA leading to $\lambda_{res}^{DA} > \lambda_{res}^{BA}$ due to the contribution of both electric and magnetic optical resonances. As mentioned earlier, this wonderful performance of

the DA is due to the enhancement of magnetic field through charge funneling in its narrow waist region [18].

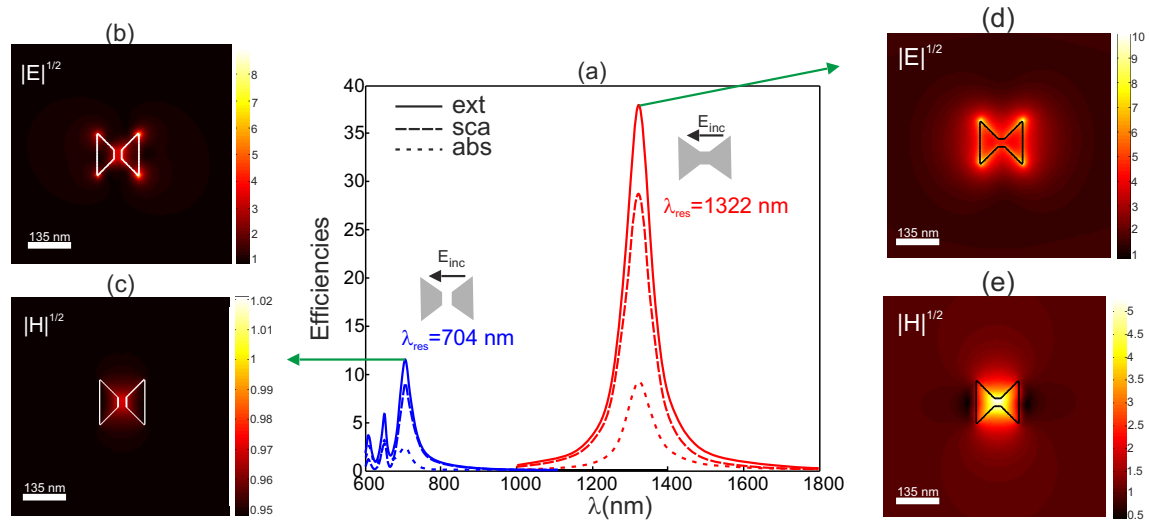


Figure 2.26: (a) Calculated extinction (solid curves), scattering (dashed curves) and absorption (dotted curves) efficiencies for two different NAs: bowtie (blue curves) and diabolo nanoantenna (red curves). The two NAs have the same values of metal thickness $t = 25$ nm, gap $g = 25$ nm and length $D = 135$ nm and both NAs are immersed in water. (b) and (c) calculated square root of the electric and magnetic amplitude distribution respectively in the xOy plane in the vicinity of BNA. (d) and (e) the same as in (b,c) but for DA. Note that the intensity distribution is calculated in the total field region.

In order to get a focused image of the hotspot generated in metal gap of DA at resonance $\lambda_{res} = 1322$ nm, the distribution of the energy flow in a vertical plane comprising the DA axis is displayed in figure 2.27. One can clearly see, the Poynting vector (see yellow arrows) that is then converging towards the neck region of the DA. Therefore, the large magnitude of scattering efficiency at resonance corresponds to the high efficiency of the funneling effect seen in figure 2.26 d and e.

Due to the interesting resonance properties of the DA, a more detailed study on this structure will be performed in the following. We will start this systematic analysis by investigating the influence of the metal nature on the resonance wavelength value. The effect of the host medium is also addressed. Finally, the influence of different geometrical parameters (length, gap and thickness) is performed. This study is an attempt to optimize the antenna performances in the context of the growing interest by our laboratory in applications involving strong enhancement of light magnetic field.

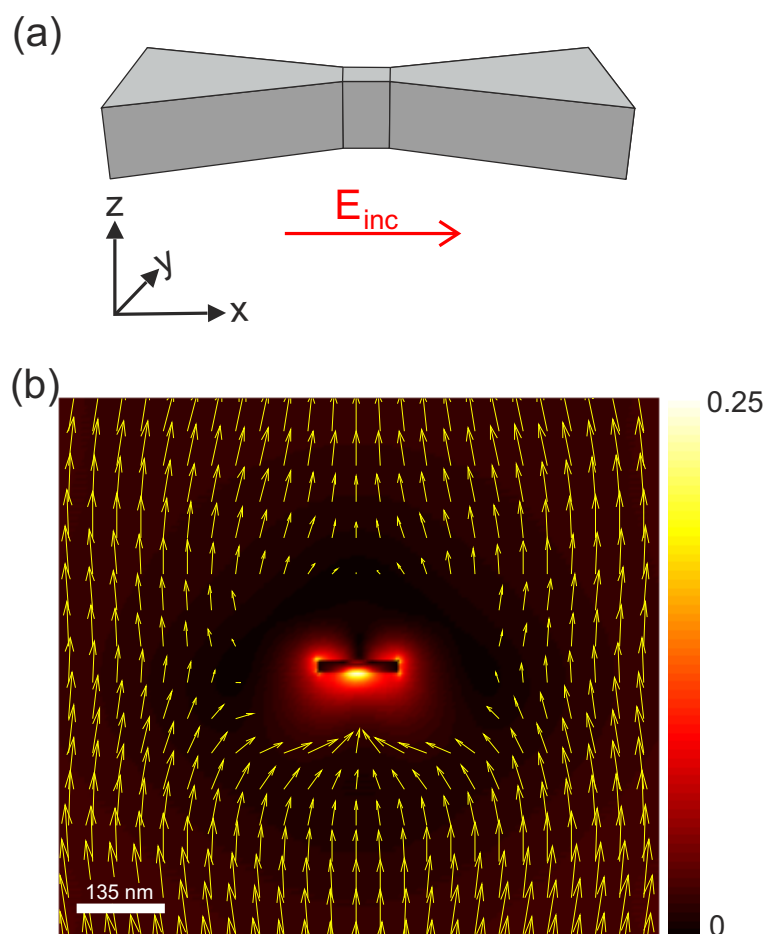


Figure 2.27: The energy flow distribution (in color map) passing through the middle of Diabolo NA in a vertical xOz plane. Yellow arrows correspond the tangential Poynting vector. Dimensions of the diabolo NA are: thickness $t = 20 \text{ nm}$, gap $g = 25 \text{ nm}$ and length $D = 135 \text{ nm}$. The incident field with a polarization along its long axis.

2.12.1/ EFFECT OF THE MATERIAL ON THE OPTICAL RESPONSE OF DA

This section is devoted to discuss the influence of different metals, in particular gold, silver and aluminum on the scattering, absorption and extinction spectra of the diabolo NA. This investigation is necessary to obtain a selective and efficient enhancement of the light into such NA. The latter is supposed to be illuminated by a plane wave normally incident (along the z axis in figure 2.27(a)) and linearly polarized along the axis of the antenna which is placed in water. The considered diabolo nanoantenna has a length D of 135 nm , gap g of 25 nm and has a thicknesses t of 25 nm . Figure 2.28 shows the optical responses (extinction, scattering and absorption) of gold diabolo nanoantenna (blue curves), silver (red curves) and (green curves) for aluminum one. The optical constants of Au and Ag are previously given in tables 2.1 and 2.2, whereas the values of the parameters of the

2.12. ABSORPTION, SCATTERING AND EXTINCTION PROPERTIES OF BOWTIE AND DIABOLO NANO-ANTENNAS

ϵ_∞	$\omega_D(\text{rad s}^{-1})$	$\gamma(\text{rad s}^{-1})$	A_1	$\Omega_1(\text{rad s}^{-1})$	$\gamma_1(\text{rad s}^{-1})$
1.0000	2.035×10^{16}	1.730×10^{14}	3.8029548	1.92×10^{15}	6.335×10^{15}
$\phi_1(\text{rad})$	A_2	$\Omega_2(\text{rad s}^{-1})$	$\gamma_2(\text{rad s}^{-1})$	$\phi_2(\text{rad})$	
-0.785	17.200025	2.147×10^{15}	2.344×10^{15}	-0.785	

Table 2.4: Permittivity of aluminum for DCP model is optimized using Δ function presented previously in section 2.8.4 over 300 – 2000 nm wavelength range

DCP model allowing the description of Al dispersion are given in the table 2.4.

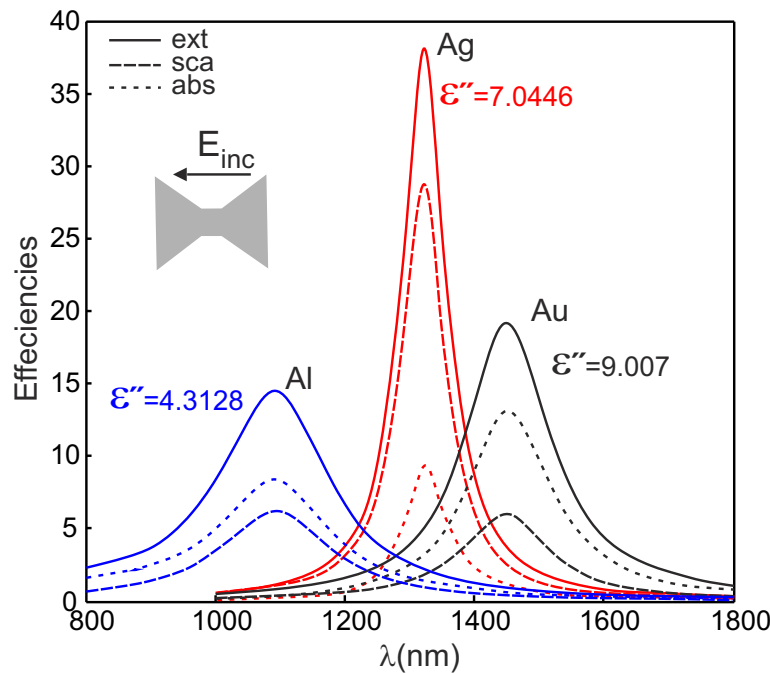


Figure 2.28: Optical responses (extinction (solid curves), scattering (dashed curves) and absorptions (dotted curves) of diablo nanoantenna made of gold (black curves), silver (red curves) and aluminum (blue curves), with $D = 135 \text{ nm}$, $g = 25 \text{ nm}$ and $t = 25 \text{ nm}$. Note that the diablo NA is placed in water medium.

As shown in Fig. 2.28, the Ag-diablo nanoantenna clearly exhibits a strongest spectral response (i.e. the extinction) outperforming the two others (Au and Al) NAs. The resonance wavelength is directly linked to the dispersion properties of the three metals for which the plasma frequency increases ($\omega_D^{Al} > \omega_D^{Ag} > \omega_D^{Au}$) (see tables 2.1, 2.2 and 2.4). This results confirms the plasmonic nature of the resonance. On the other hand, absorption of each metal is related to their imaginary parts $\epsilon''(\omega)$, for example, aluminum exhibits weak losses in visible region because of its imaginary part which represents the conduction loss is smaller than two others Ag and Au (see the values of $\epsilon''(\omega)$ for the three metals in figure 2.28). Furthermore, the quantity of the absorbed energy as function of D is compatible with the so called loss of energy relation Λ , where the latter can

express in term of the complex Poynting theorem as (see the derivation in Appendix A):

$$\Lambda = -\frac{1}{2} \int \int \int_V \varepsilon_0 \varepsilon_r' \omega |E^2| dV \quad (2.83)$$

In our case, the distribution of the electric field is almost the same for the three metals of DA (numerically verified), therefore the term $\int \int \int_V |E^2| dv$ can be assumed to be constant A leading to write Λ as: $\Lambda = -\frac{1}{2} \varepsilon_0 \varepsilon_r' \omega A$ and hence the latter is directly proportional to ε_r' indicating that our numerical results presented in figure 2.28 are compatible with the relation Λ . Henceforth, our study will be focused in Ag-DA due to its resonance properties in the NIR region. The work of the next sections is dedicated to perform a geometrical study on this Ag-nanoantenna in addition to the influence of the host medium nature.

2.12.2/ EFFECT OF THE HOST MEDIUM ON THE OPTICAL RESPONSE OF DA

This study is also interesting due to the antenna sensitivity to variations of the surrounding medium index. In fact, the relationship between the index and the dielectric function ($\varepsilon_m = n_m^2$) emphasizes that increasing the value of the latter leads to adjust the position of SPR. As shown in figure 2.29 the scattering spectral positions of DA strongly depend on the host index of refraction. As expected, a linear increase of the resonance with n_m is obtained.

2.12.3/ EFFECT OF THE LENGTH

There are other important factors (shape and geometry) that play a crucial role and govern the optical response of optical nanoantenna. Particularly, one of the most determinant factors to control the resonant frequency and scattering property is the size of the particles. Figure 2.30 investigates the influence of the length (D) of the DA on the scattering efficiency where the two others parameters g and t are fixed to 25 nm . This figure presents the numerical calculations for four different DA lengths. As this latter becomes longer, the longitudinal dipole resonance shifts to the large wavelength due to the increasing of the spatial extension of the resonance mode over all the geometry of the DA. At a first approximation, the resonance wavelength is proportional to D^2 due to the fact that the width of the DA is also modified simultaneously with its length (the DA is circumscribed inside a square of side D). Indeed, the resonance wavelength of DA is a combination of the electric and the magnetic fields at the corner and center of DA respectively, therefore when D varies, the magnetic field is not modified leading to λ_{res}/D^2 is not more coherent. In

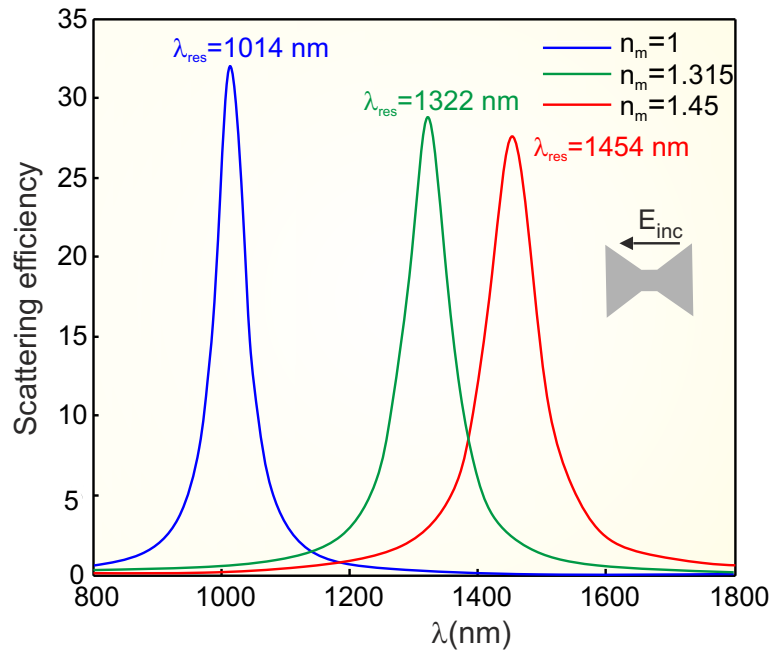


Figure 2.29: Sensitivity of the scattering responses to the refractive index of the surrounding medium for a silver daibolo nanoantenna with $D = 135 \text{ nm}$, $g = 25 \text{ nm}$ and $t = 25 \text{ nm}$, blue (in air), green (in water), red (in oil).

addition, this red-shift of the resonance wavelength is accompanied by a decreasing of the scattering efficiency (current density function of D). At the resonance wavelength, the scattering efficiency with a smaller length of DA is about ~ 30 orders of magnitude higher than the corresponding geometrical cross-section.

2.12.4/ EFFECT OF GAP SIZE

The effect of the gap size is also investigated through the calculation of the scattering efficiency. Numerical simulations are performed for different lengths of gap (g) where both D and t are fixed to 135 nm and 25 nm respectively. It is clear from figure 2.31, that when the length of gap is increased, the scattering resonance peak shifts towards high energy region. In contrast, the scattering efficiency exhibits a non linear behavior due to the fact that both length and width of the gap zone are also modified simultaneously. One can demonstrate that by spreading out the two metallic triangles, the magnetic confinement decreases leading to a smaller scattering efficiency. Nevertheless, if we enlarge the gap width, the current density in the neck zone becomes smaller. The combination of these two somewhat contradictory effects allows optimizing the DA performances (see green curve of figure 2.31). However, the DA geometries are proposed to be compatible with commonly used fabrication techniques that are available at our institute.

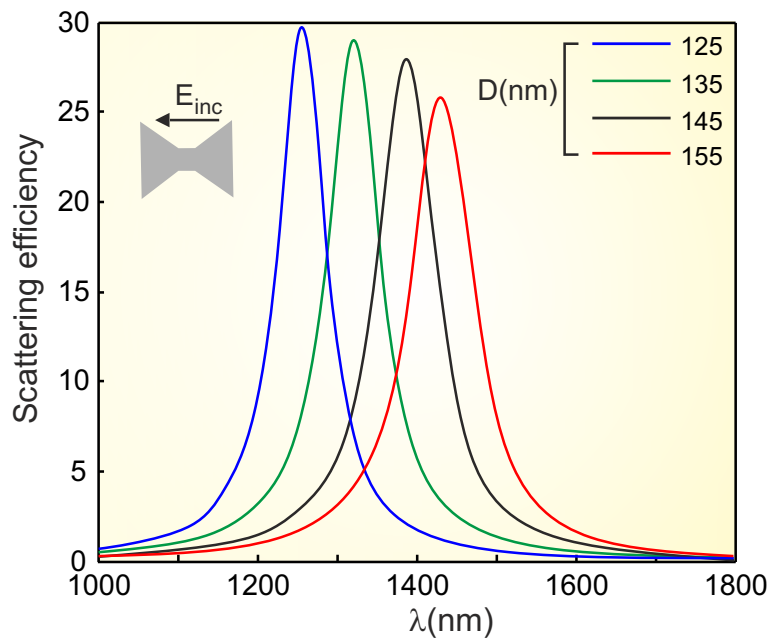


Figure 2.30: Evolution of the scattering efficiency with length of silver DA, g and t are 25 nm . Note that the diatomic NA is placed in water medium.

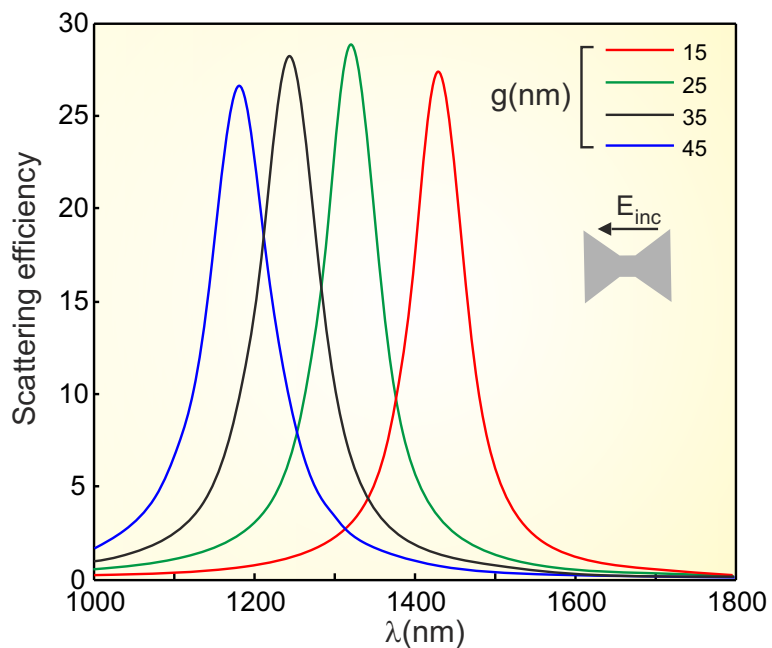


Figure 2.31: Scattering efficiency with the gap size of DA made in silver, D and t are 135 nm and 25 nm respectively. The water is considered as a medium.

2.12.5/ EFFECT OF THE METAL THICKNESS

The numerical results in Fig. 2.32 clearly show the effect of thickness of the DA on the scattering efficiency. The higher thickness is, the higher somewhat in scattering efficiency is, while, its scattering resonance peak shifts to low energy region. Nevertheless, when the thickness is decreasing, the current density at the DA center increases leading to highly mode confinement (larger mode volume) that induces a blue-shift of the resonance wavelength. Nonetheless, this effect seems to be counterbalanced by the enhancement of the electric field confinement at the DA corners induced by the small metal thickness. Thus, the total volume of the mode increases when t increases.

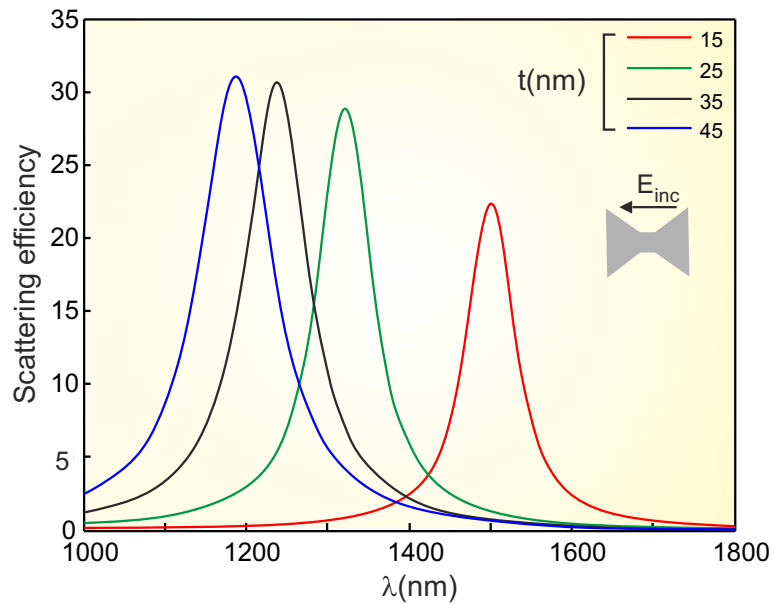


Figure 2.32: Dependency of the scattering efficiency on the thickness t of DA made in silver, D and g are 135 nm and 25 nm respectively. The diablo NA is placed in water medium.

2.13/ CONCLUSION

In this chapter, we have first reviewed the state of the art on NPs including several types of isotropic (spherical) and anisotropic (Bowtie and Diabolo) nanoantennas and their optical response supported by LSPRs. We have then described with more detail the Mie theory that can address basically isotropic NPs through the determination of their absorption and scattering efficiencies. Among such isotropic shapes, the responses of gold nanosphere for two different sizes in the near and far field were calculated using a

Matlab code involving the formulas of Mie theory. We have showed that for both sizes, the dipolar resonances are compatible with the polarisability relation of the sphere. In addition, the scattering coefficient is powerless when the sphere volume is small and the global extinction cross section is almost obtained by the contribution of the absorption one. On the other hand, the latter becomes less effective compared to the scattering as the sphere size gradually increases. The obtained results can be appropriate to select the suitable NPs in very important applications, for example, the photothermal therapy due to light is mainly absorbed by the particles and hence the energy converted to heat, whereas larger particles is desirable in imaging applications. Unfortunately, the calculation of the optical response using Mie solution, is restricted to the spheres and ellipsoid geometry.

To overcome the problem of constraints on the shapes, a numerical approach which the most commonly used is FDTD method, have been successfully applied to solve light-matter interaction especially in nano-optics. In order to calculate absorption, extinction and scattering coefficients of any shape NPs, we have adapted the TF/SF technique and numerically investigated the 1D, 2D and 3D and their validations inside a conventional homemade FDTD code. The numerical results obtained have indicating that there is no agreement with the analytical results calculated by Mie theory due to the errors arising from numerical such as mesh size. Consequently, we have integrated the CPT into our TF/SF-FDTD code in order to optimize the spatial resolution that describes such objects, and to avoid a huge FDTD simulations resulting from the increase of spatial cell size. Several simulations were conducted pointing out that CPT results exhibit a high precision with respect to the Mie solution. We were able to construct an algorithm that is capable of modeling any NPs.

From the outcome of our numerical developments, we have investigated the optical responses of two kinds of nanoantenna (BA and DA) in terms of extinction, scattering and absorption efficiencies. We have succeeded to optimize a diabolo design that has a very large amount of scattering compared to the BA one. This interesting result was obtained thanks to a highly localized electromagnetic field in the vicinity of the DA (both center and corners of its design). Different simulation studies have been made to investigate the characteristics of the resonance of DA through its influence by: the metal nature; the host medium and geometrical parameters (length, gap and thickness). A selective and efficient enhancement of light into silver DA have been obtained and outperformed the two other (Au and Al) NAs. The numerical study have also reported that the DA is very sensitive to the variations of the surrounding medium index and exhibits a linear increase in resonance with increasing n_m . The obtained systematic study (length, gap and thickness) that were performed explaining that as the length of DA becomes longer, the

2.13. CONCLUSION

resonance properties shifts to red region accompanied by a decreasing of the scattering efficiency. Whereas the increasing of the gap size displays a shift towards high energy region of the scattering resonance peak, and the latter has a non linear behavior. In addition, the effect of thickness of the DA on the scattering efficiency has been clearly shown that the larger mode volume induces a blue-shift of resonance wavelength with higher scattering coefficient. Finally, the obtained results explain that the factors studied above play a vital role on the tunability and the increasing of the effective volume up to several times the physical cross section of NA. This feature can be employed to enhance the interaction of any object located in their proximity with electromagnetic wave.

In the next chapter, we will address a different type of plasmon excitation called plasmonic waveguide mode in order to characterize the optical properties of periodic structure with subwavelength dimension.

OPTICAL TRANSMISSION PROPERTIES THROUGH SUB-WAVELENGTH ANNULAR APERTURES ARRAY (AAA)

3.1/ INTRODUCTION

The interesting optical properties associated with localized surface plasmon (LSP) of metallic NPs (spheres, bowtie and diabolito NAs) have been numerically discussed in the previous chapter. The FDTD method with TF/SF and CPT techniques was used to model the optical responses of the NPs under study. This chapter deals with the exploitation of Propagating Surface Plasmons (PSPs) resulting from the excitation of a guided mode inside nano-apertures made in metallic layer to act as Enhanced Transmission Metamaterials (ETM). The main property of such ETM is the fact that the excited mode has no cutoff and efficient transmission can be obtained for large values of wavelength compared to the aperture dimension.

This chapter therefore, is devoted to the study of the excitation of this fundamental guided mode and aims to explore the optical properties of nanoscale subwavelength annular apertures when arranged in a array (AAA: Annular Aperture Array). Even if the excited mode has no cutoff, experimental and technological constraints need to be taken into account in order to achieve individual components capable to realize basic optical operations. Consequently, this goal will be accomplished by correctly designing the structures (geometrical parameters) to get efficient/low power performances. We conducted

3.2. STATE OF THE ART ON THE TRANSMISSION THROUGH NANOAPERTURES

extensive numerical simulations based on a 3D-FDTD homemade code where the DCP dispersion model, the TF/SF and the CPT techniques are adapted to accurately describe the dielectric constant of the considered metals and its geometry. We will present basic principle of waveguides in terms of the dispersion relation of fundamental guided modes in order to provide a basic information about the cutoff frequencies and effective indexes. The last section will be dedicated to the numerical study of the excitation of TEM guided mode through an AAA. In particular, we highlight on the factors that would contribute to optimize the transmittance in visible range.

3.2/ STATE OF THE ART ON THE TRANSMISSION THROUGH NANOAPERTURES

The observation made by T. W. Ebbesen's team of an Extraordinary Optical Transmission (EOT) of light through artificially periodic nanostructured metallic layers has inevitably revolutionized the field of nano-optics (see figure 3.1). The amazing feature monitored in that subwavelength apertures is due to the very large measured transmission obtained from the whole periodic structure compared to the sum of transmissions of each single aperture. Whereas, this EOT only appears for wavelength values larger than the structure period meaning that evanescent diffracted orders plays a predominant role in the observed phenomenon.

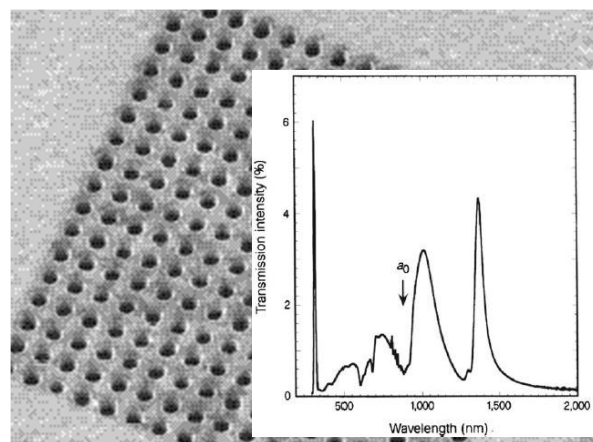


Figure 3.1: Zero-order transmission spectra of an Ag array (period (a_0) = 900 nm, diameter= 150 nm and thickness= 200 nm). Ref. [26].

Few years after the publication of T. W. Ebbesen et al., there has been a growing interest in many experimental and theoretical studies in order to investigate the physical origin of the EOT presented in that paper. In a previous study, the position of large

transmission peak of a cylindrical aperture array engraved in opaque thin metallic film corresponds exactly to the excitation of the surface plasmon wave of the structure without apertures. Although most of works on EOT are based on SPR, the guided modes offer a better efficiency and take advantage of increasing in transmission capacity at larger wavelength values with respect to the nanostructures dimension [116, 117, 118, 119]. In the last decade, the EOT has attracted tremendous attention from research teams in particular theoreticians due to the need of extensive numerical studies to get a deeper understanding of the EOT phenomenon.

One of the first examples of a theoretical calculation by using a Fourier modal method of light transmission through 2D grating, was presented by Popov et al. [120]. References [121] and [122] calculated the transmission of a 2D hole perforated in metal film via a modal expansion of the fields (see figure 3.2). The researchers developed in their papers a very simple and efficient minimal model and arrived at the conclusion that the holes behave like subwavelength cavities for the evanescent waves to couple with the surface plasmon on both sides of the films. A numerical study of the transmission of a tiny (20 nm) 2D hole grating was performed, using a differential method, by Salomon et al. [123]. In references [124, 125, 126], the authors argue that the enhanced transmission is associated with the cavity resonances into the holes (cas of lamellar gratings). In addition, a near field analysis of the Ebbesen experiment in the light of evanescent short range diffraction was presented in [127]. Furthermore, an interesting comparison between the EOT phenomenon and multiband frequency selective surface (FSS) in near-infrared to microwave region was addressed in [128, 129]. These FSS elements are designed for a wide domain of applications such as Fabry-Perot interferometers, filters, couplers for laser cavity output, or simply as polarizers. Their optical responses are directly linked to their geometrical parameters (i.e. their thickness, aperture size, period), and particularly the shape of the aperture.

In recent years, several publications have appeared documenting a very good discussion of the EOT phenomenon. Garcia de Abajo [130] published in 2007, a quite useful review paper. Besides, Catrysse and Fan [131] have demonstrated through an interesting paper, the principle of the EOT in Ebbesen's experiments in term of different mechanisms. In those works, it was indicated that the EOT can be explained as a combining effect of surface plasmon waves and propagation plasmonic guided modes. In a recent paper, Gordon et al. [132] stated a general review paper on EOT including the discussion of various approaches, developments in hole-array fabrication, and integration of hole-arrays into devices. As reported by Ebbesen, the challenge is how to obtain transmission spectra located at wavelength greater than the array period with perforated metallic opaque

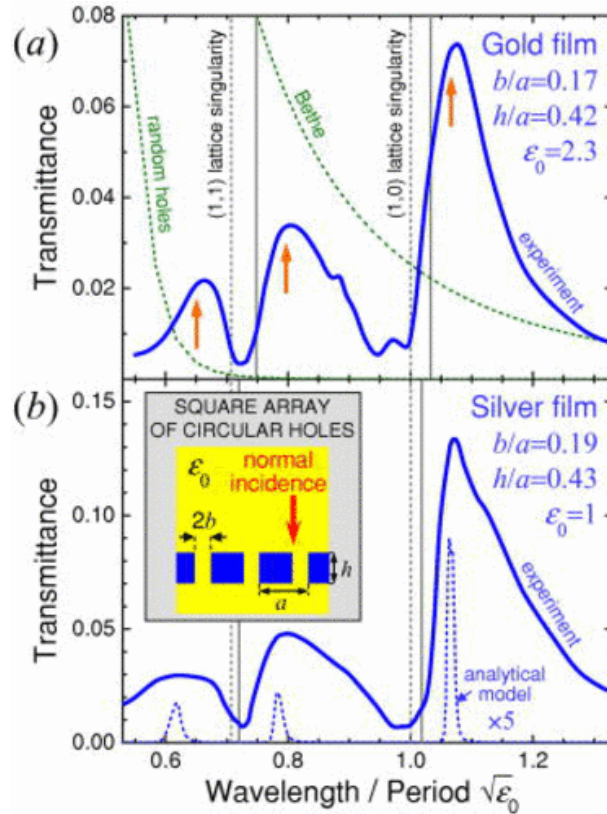


Figure 3.2: Theoretical and experimental transmission spectra of extraordinary optical transmission EOT structures based on cylindrical holes engraved into opaque metallic layer. (a) Experimental zero-order transmission spectra of Au film on a quartz substrate, the film thickness is $h = 250 \text{ nm}$, the hole radius is $b = 100 \text{ nm}$ and the lattice constant is $a_o = 600 \text{ nm}$. Ref. [121] (b) Experimental (solid curve) and analytical model (dotted curve) of zero-order power transmittance at normal incidence for a square array of holes ($a_o = 750 \text{ nm}$ and $b = 140 \text{ nm}$) in a free standing Ag film $h = 320 \text{ nm}$. Ref. [122]

plates. A simple idea is then emerged: it is to get better optical transmission based on a guided mode that could be excited inside through the openings. The structure periodicity has only the role of phase matching that allows controlling the energy propagation direction through quantified diffracted orders. Therefore, the concept of waveguide is a key point for designing these structures. Consequently, the first periodic waveguide structure proposed in Refs. [30, 31] was AAAs due to fact that it can support a guided mode without cutoff, namely, the TEM mode although this latter occurs under specific conditions [135]. However, an Enhanced Transmission (ET), larger ($\approx 5\times$) that obtained EOT (Ebbesen) with cylindrical holes was achieved (see figure 3.3) [31, 136, 134, 137, 133, 138]. In our laboratory, the first numerical study demonstrating the ET through AAA structure in comparison with cylindrical aperture array was published in [31]. comparison is done by partially filling the cylindrical holes of a EOT structure with metallic cylinders smaller in order to get AAA geometry. Therefore, this comparison pointed out that by increasing

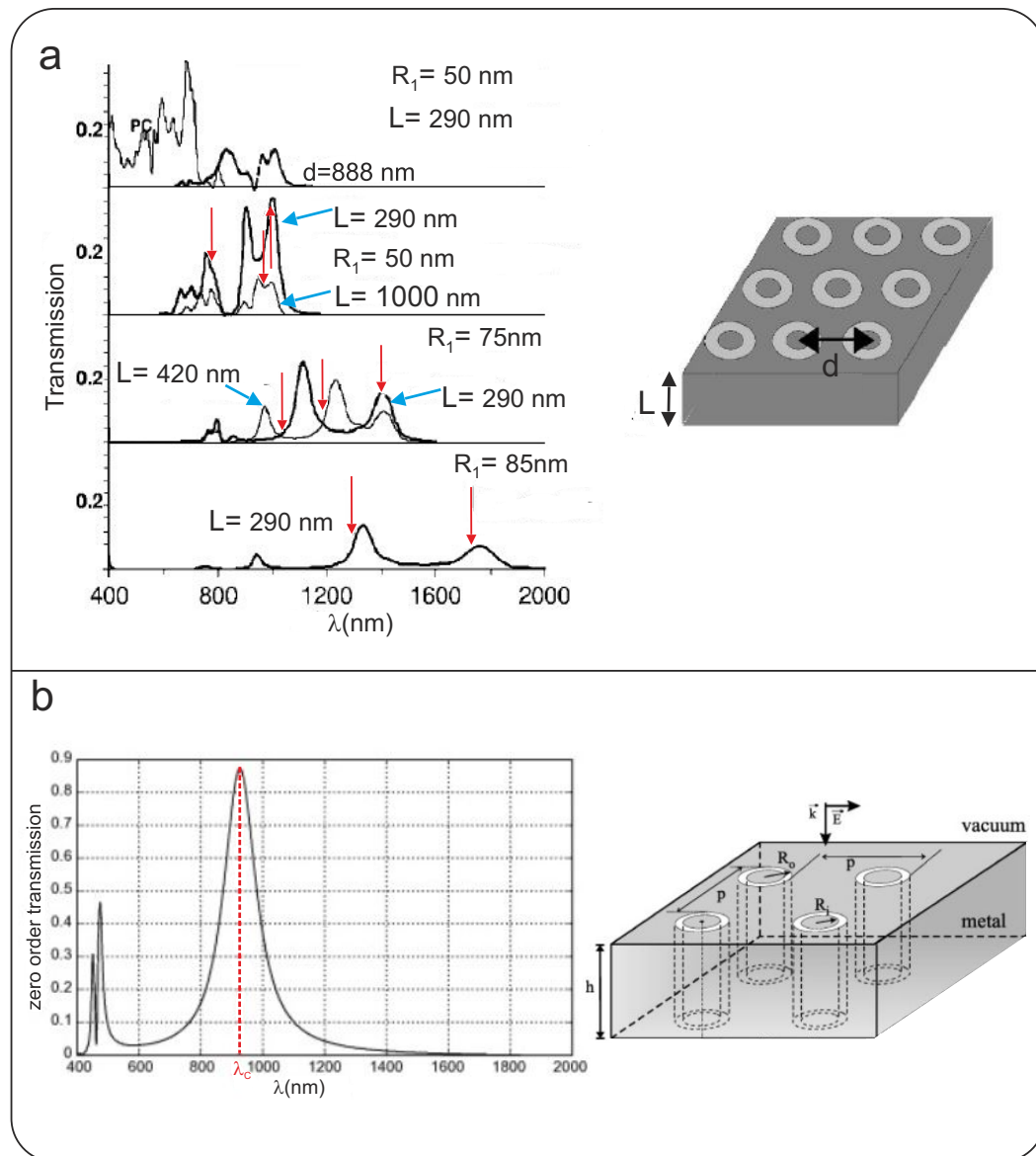


Figure 3.3: Theoretical study of extraordinary optical transmission EOT in AAAs structure. (a) Transmission spectra of a square array of coaxial cylinders, spaced at $d = 555$ nm and for various inner radii (Au cylinders) R_1 and metal thickness L . Note that the outer radii (silica cylinder) is fixed to $R_2 = 100$ nm. The arrows indicate the theoretical $m = 0$ and $m = 1$ cylindrical surface plasmon (CSP) resonance peaks. The top panel includes the cases of a perfectly conducting (PC) and a periodicity of $d = 888$ nm (which has the same predicted resonance positions as the $R_1 = 50$ nm, $L = 290$ nm case in the second panel). Ref. [133]. (b) Transmission spectrum through a silver layer perforated with annular apertures arranged into a square array. The period is $p = 350$ nm, the inner and the outer radii of the coaxial cavities are $R_i = 75$ nm and $R_o = 100$ nm, respectively. The metal thickness is set to $h = 100$ nm and the structure is illuminated by a linearly polarized plane wave at normal incidence. Ref. [134].

3.3. REASON FOR CHOOSING AAA

the hollow area we can get more transmission at larger values of the wavelength. Nevertheless, the TEM guided mode of the AAA structure was not responsible of the obtained ET.

In this chapter, the demonstration of the ET through AAA by the excitation of the TEM guided mode is presented. In the context of improvement the transmission efficiency, this is my first contribution in the theoretical study of the AAA structure. Besides, we address the theoretical results based on FDTD calculations in order to compare with the experimental study that has been performed in Ref. [139]. The excitation of the TEM mode is demonstrated through the emergence of an additional transmission peak located at a wavelength larger than the one associated with the Transverse Electric (TE_{11}) mode.

3.3/ REASON FOR CHOOSING AAA

Before addressing the numerical simulation results, it is necessary to get a basic understanding of waveguide theory of metallic waveguides. We will not delve in the mathematics details of the waveguide theory insofar as we limit our discussions to a brief outline of the formalism and to a statement of the required results. The idea of the waveguide arises from the electromagnetic waves propagating along a hollow metal tube which are typically constrained inside it. Consequently, since the electromagnetic wave is surrounded by metallic boundaries, it is impossible to spread out and hence to neglect the losses even if small propagation distances are in play.

According to waveguide theory, the electromagnetic wave that can propagate inside the waveguide are classified into different types of electromagnetic mode according to the different components within an electromagnetic wave: Transverse Electric (TE), Transverse Magnetic (TM) and the Transverse ElectroMagnetic (TEM). Each mode has a definite higher wavelength limit called cutoff wavelength where above no wave can propagate inside the waveguide. There are several modes that can be excited and their number decreases for a given size of waveguide as the wavelength increases. In addition, there is the so-called dominant mode (the fundamental mode) in the waveguide that can be guided at the largest wavelength.

3.3.1/ TYPES OF WAVEGUIDES

Let's give an example of the first modes that can propagate within three types of waveguides (rectangle, circular and coaxial section ones). For this purpose, figure 3.4 gives us the cutoff wavelengths of some examples of waveguide as a function of their geometrical parameters. Let's consider all examples of waveguides in a PEC, as seen in Fig. 3.4 , the fundamental mode TE_{10} of a rectangular waveguide (sides a and b with $a > b$) has a largest cutoff wavelength at $\lambda_c = 2a$. When a circular waveguide is considered with a radius $R = \frac{a}{2}$, the fundamental mode TE_{11} has a smaller cutoff wavelength at $\lambda_c \approx 1.7a$. Let us consider a coaxial waveguide, for all modes except two, the difference between the outer and inner radii determines the value of the wavelength cutoff which means this value is very small. These two modes are: (a) TEM mode, with no cutoff (i.e. $\lambda_c \rightarrow \infty$), and (b) the TE_{11} mode, for which the cutoff wavelength is proportional to the sum of the radii: $\lambda_{TE_{11}}^c \approx \pi(R_i + R_o)$ where R_i and R_o are the inner and outer radii respectively. This allows designing an AAA structure where the period can be smaller than this cutoff wavelength that will lead to an ET based on the excitation and the propagation of this specific TE_{11} mode [27, 140, 30, 31, 91, 137, 141]. Therefore, the unique mode that has a large value of cutoff wavelength in a coaxial waveguide, is the TE_{11} mode. However, when we try to guide the light through metallic waveguide in the visible or IR spectral range, the dispersion should be taken into account because these types of metals suffer from losses. Furthermore, the guided mode becomes a hybrid mode combining properties of TE and TM ones [29], therefore it is necessary to determine the effect of the metal nature on the guided modes.

3.3.2/ DISPERSION DIAGRAM OF THE GUIDED MODE

The basic information about the guided mode can be provided by the relation dispersion. In a recent paper by Catarysse and Fan [142], an analytical parametric dispersion relation has been performed in the case of nano-coaxial waveguides made in real metal. This relation requires a numerical solution to determine the modal propagation constants simultaneously with the propagation losses. The implementation of an algorithm to calculate the dispersion diagrams of modes for cylindrical and coaxial waveguides using the FDTD method has been performed by N-order Body-Of-Revolution-FDTD (BOR-FDTD). The Maxwell equations in the latter method is written in the cylindrical coordinates system [10, 94], whereas the N-order method consists in exciting the structure using an initial field whose spectrum extends over all of the possible frequencies of the structure modes. Then the FDTD code determines the field variations versus time. After a transient delay,

3.3. REASON FOR CHOOSING AAA

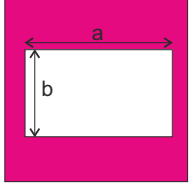
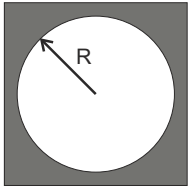
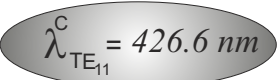
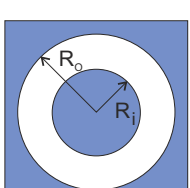
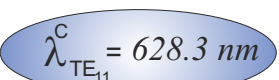
Structure	First modes	Examples
	$\lambda_{TM_{11}}^c = \frac{2ab}{(a^2 + b^2)^{1/2}}$ $\lambda_{TE_{10}}^c = 2ab$	$a=b=250 \text{ nm}$ 
	$\lambda_{TE_{11}}^c = \frac{2\pi R}{1.841}$ $\lambda_{TM_{01}}^c = \frac{2\pi R}{2.405}$	$R=125 \text{ nm}$ 
	$\lambda_{TE_{m1}}^c \equiv \frac{(R_o + R_i)\pi}{m}$ $\lambda_{TE_{mn}}^c \equiv \frac{2(R_o - R_i)}{n-1}$ $\lambda_{TM_{mn}}^c \equiv \frac{2(R_o - R_i)}{n}$	$R_o=125 \text{ nm}$ $R_i=75 \text{ nm}$ 

Figure 3.4: Three different kinds of waveguide made in perfectly electric conductor (PEC) with their cutoff wavelengths of the first guided modes.

only the eigenmodes of the structure persist and lead to a great spectral radiant intensity at every eigenfrequency. The components of the initial EM field which differ from an eigenmode will disappear [90, 143].

As an example, the N-Order BOR-FDTD code calculates the cutoff wavelengths of the first guided modes supported by both cylindrical and coaxial waveguides made in silver and compare them to the PEC case (see Fig. 3.5). The results of modes are denoted by the two numbers (m, n) where m is the azimuthal number ($e^{im\phi}$ with ϕ the azimuthal angle) and n is the radial one (Bessel functions of n order). As seen in Fig. 3.5, the silver waveguide exhibits a cutoff wavelength of the TE_{11} mode in red region compared with the PEC one. Furthermore, the coaxial configuration presents cutoff wavelengths that are more shifted towards the red region with regard to cylindrical one. In addition, metal losses induce additional red shift. Fig. 3.5 shows that $\Delta\lambda$ between the two cutoffs in PEC case is 130 nm whereas it becomes 200 nm in the case of silver [29]. Even if we are expecting to work with the TEM mode, the study of the excitation and propagation of the TE_{11} mode will bring to us more physical insights pointing out the difficulties underlying with the excitation of the cutoff-less TEM mode.

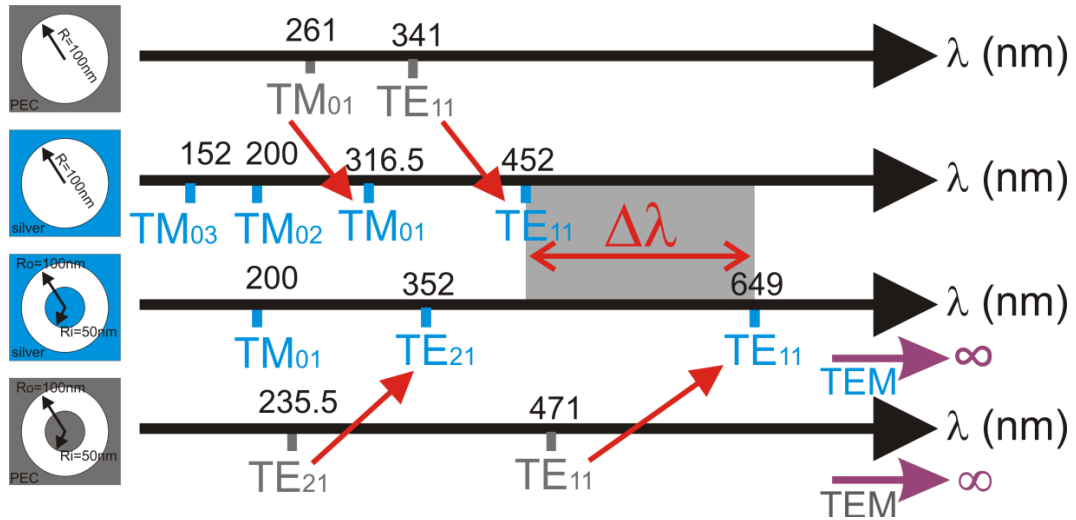


Figure 3.5: Different kinds of the guided modes and their cutoff wavelengths in the case of cylindrical and coaxial nano-waveguides made in a perfect conductor (gray) and in silver (blue). Cylindrical radius is set to $R = 100$ nm and corresponds to the outer radius R_o of the coaxial structure whereas the inner radius of this latter is set to $R_i = 50$ nm. Note that the $\Delta\lambda$ represents the difference between the two cutoff positions of the two fundamental modes. This value, estimated here as $2R$, can be used to quantify the gain due to the coaxial structure. This figure is reproduced from Ref. [29]

3.3.3/ TEM GUIDED MODE

In the case of coaxial waveguide made in perfect conductor, the TEM mode has an electric and magnetic fields that are transverse to the direction of propagation. These two fields are invariant under rotation around the axial direction meaning that there is no dependence according to the azimuthal angle. The electric field is radial while the magnetic one is azimuthal (ortho-radial). Furthermore, this mode holds advantageous property that is its invariant effective index which makes it dispersionless at any frequency ($n_{eff} = n_d$ where n_d is the optical index of the inner media).

Contrarily, when a real metal is considered, the above properties (transverse character and dispersionless) are no more valid. To figure out the influence of the metal nature on the first guided modes (TEM , TE_{11} and TE_{21}), we plot the dispersion diagram of these modes for both PEC and silver coaxial waveguides (see Figure 3.6) with air as inner media. In the case of PEC, the TEM mode has an effective index of 1 and its dispersion curve is superimposed on the light line. For all higher modes, the dispersion relation is given by:

3.3. REASON FOR CHOOSING AAA

$$\omega \sqrt{1 - \left(\frac{\omega_c}{\omega}\right)^2} = k_z c \quad (3.1)$$

where ω_c is the cutoff angular frequency, k_z is the propagation constant along the z -axis (the waveguide axis) and c is the light velocity in vacuum. The value of $\omega_c(TE_{m1})$ for the TE_{m1} modes (first modes) can be analytically written as: $\omega_c = \frac{2m \cdot c}{R_i + R_o}$.

For a coaxial waveguide made in silver, the material dispersion must be taken into account. Parametric equations can be established for the dispersion relation [142]. Nevertheless, a BOR-FDTD code was developed by our team allowing determination of the diagram dispersion [27]. By integrating the DCP model of silver given in table 2.2 and varying m from 0 to 2, we get the three red curves of figure 3.6. For this study, and as for the PEC structure, the inner and outer radii of the waveguiding region are taken to be $R_i = 50 \text{ nm}$ and $R_o = 100 \text{ nm}$, respectively. One can see from figure 3.6 that the TEM guided mode exhibits a dispersion curve lying just below the light line meaning that it has a plasmonic character. On the other hand, the TE_{11} and TE_{21} modes present a hybrid properties combining a conventional character near their cutoff and a plasmonic one for larger values of the frequency.

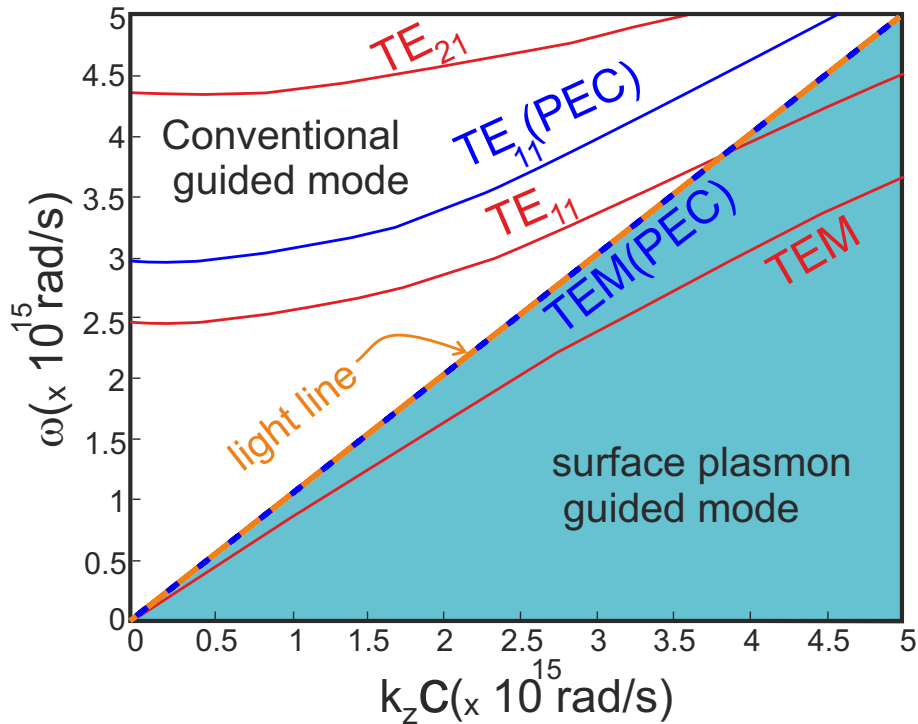


Figure 3.6: Dispersion diagrams of guided modes of an coaxial waveguide made in silver (red curves) and PEC (blue curves). The inner and outer radius are fixed to $R_i = 50 \text{ nm}$ and $R_o = 150 \text{ nm}$ respectively.

The electric field distribution inside the waveguide of the three first guided modes are presented in figure 3.7. The azimuthal dependence is clearly shown where a perfect azimuthal symmetry is obtained for the TEM mode, a $\sin\phi$ or $\cos\phi$ dependence for the TE_{11} mode and a $\sin(2\phi)$ or $\cos(2\phi)$ dependence for the TE_{21} mode. Nevertheless, due to the real nature of the metal (here silver), the TEM mode is no more pure transverse electric and magnetic. Very small longitudinal components appear. Nonetheless, this mode will be named TEM in the following.

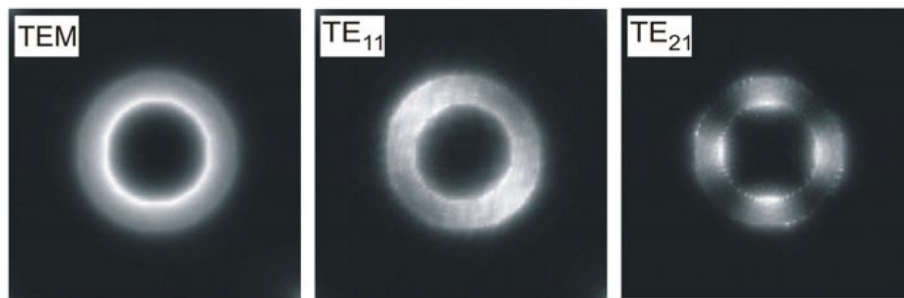


Figure 3.7: Distribution of the intensity light for the first three-guided modes of a coaxial waveguide made in silver with: $R_o = 75 \text{ nm}$ and $R_i = 50 \text{ nm}$.

Due to the symmetry properties shown in figure 3.7, the TE_{11} mode is the only mode that can present non-zero overlap with a linearly polarized incident plane wave. Thus, at normal incidence, the ET through AAA is due to the excitation and the propagation of this peculiar mode inside the annular aperture. The transmission peak appearing in the spectrum of figure 3.3(b) around $\lambda = 910 \text{ nm}$ corresponds to the excitation of the TE_{11} mode at its cutoff wavelength. The second peak, located around $\lambda = 500 \text{ nm}$, is the first interference harmonic of the same TE_{11} mode. Its spectral position is then given by a phase matching condition that will be explicitly given in the following.

However, the TEM mode of the annular aperture can not be excited at normal incidence. As reported by Baida.F. in ref. [135], it was found through an analytical determination that the TEM guided mode can only be excited when the overlap between the incident beam and the mode is non zero. This condition can only be achieved with a transverse magnetic TM polarized plane wave under oblique incidence. This result was supported through numerical simulations involving an original FDTD algorithm that was developed in the A. Belkhir's thesis [144]. One interesting result is shown in Fig. 3.8(a) where the transmission spectrum through an AAA structure (see figure caption for geometrical parameters) illuminated at an angle of incidence of $\theta = 40^\circ$ exhibits a peak at a value of the wavelength that is beyond the cutoff wavelength of the TE_{11} mode. To point

3.3. REASON FOR CHOOSING AAA

out the nature of the propagating mode at this wavelength value, we plot in figure 3.8 (b and c) both the radial $E_r(x, y)$ and azimuthal $E_z(x, y)$ electric field components calculated at the middle of the metal thickness. As quite expected, the appearance of these two quantities confirms the excitation of the TEM mode since the radial component of the electric field is independent of the azimuthal angle and the axial one is negligible [135].

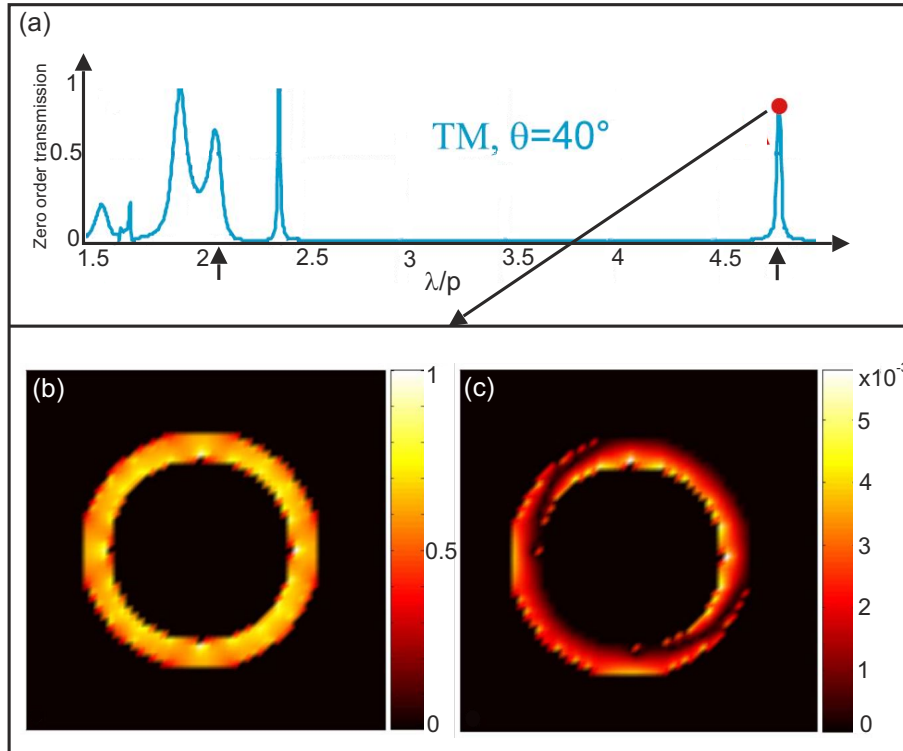


Figure 3.8: (a) Transmission spectra of AAA structure made in a perfect conductor their geometric parameters have been adjusted by setting the inner and outer radius to $R_i = p/4$ and $R_o = p/3$ respectively, p being the period of the AAA structure. The structure is illuminated by a TM polarized plan wave at angle of incidence of $\theta = 40^\circ$. Note that the spectral response presents extra peaks denoted by the point A due to the excitation of TEM guided mode inside each coaxial aperture. Modulus of the radial (b) and azimuthal (c) electric field components calculated at $p/2$ from exit side of the structure for the parameter of point A in (a). These two quantities are normalized according to the maximum of the radial component. Ref. [135]

Even though the excitation of TE_{11} mode has high transmission coefficient, but the excitation of the TEM mode has several advantages. As mentioned above, the properties of the TEM mode are somewhat different because it has no limiting frequency and, consequently, the associated transmission peak can occur at a wavelength λ_{TEM} which is settled in first approximation, by a phase matching condition as in a conventional Fabry-Perot interferometer. In fact, this peculiar mode is exactly analogue to the fundamental cutoff less mode of a linear slit [125]. Consequently, the transmission peak that appears

at λ_{TEM} depends on the thickness of the metal layer (i.e. the cavity length) and on the nature of the metal. Accordingly, it may correspond to a larger wavelength than that of the TE_{11} mode. The phase matching condition can be written as follows:

$$\lambda_{TEM} = \frac{2\pi n_{eff} h}{m\pi - \phi_r} \quad (3.2)$$

where ϕ_r is the phase change induced by the mode reflection at the two ends of the coaxial waveguide including the scattering by the edges of the apertures (ϕ_r depends then of the aperture geometry as it was recently demonstrated in ref. [145]), h is the metal film thickness, M is an integer and n_{eff} is the real part of the effective optical index of the TEM mode (n_{eff} becomes the optical index of the inner dielectric media in the case of a perfect electric conductor structure). Note that the phase term ϕ_r contains the contribution of the evanescent waves generated by diffraction at the two side of the apertures (metal-dielectric interfaces). Some authors [146, 147] attributed this effect to the coupling between the vertical guided mode and the horizontal diffracted waves and others expressed the same thing through an analytical form by adding a phase term to the Fabry-Perot phase matching formula [91, 125] or by integrating it in the same formula as a term depending on the overlap integral between the guided mode and the incident wave [92]. Thus, similarly to a conventional Fabry-Perot interferometer, it is possible to tune the spectral position of the transmission peak by varying h and as a consequence, to obtain an ET for a wavelength larger than $\lambda_{TE_{11}}^c$. However, as it will be shown, the fabrication of nanometric high aspect ratio structures is still a challenging task and the losses associated with noble metals in the visible range prohibits the use of thick metallic plate.

3.4/ THEORETICAL STUDY OF THE EXCITATION OF TEM GUIDED MODE THROUGH AAA STRUCTURE

In this section, we present a brief description of the used FDTD method allowing treatment of periodic structures illuminated under oblique incidence. The considered structure is supposed to be periodic in two dimensions (x and y for example) and finite in the z direction. The FDTD calculation window consists of one unit cell (one period) and the Floquet-Bloch periodicity conditions [148] are applied to the electric and magnetic components through:

3.4. THEORETICAL STUDY OF THE EXCITATION OF TEM GUIDED MODE THROUGH AAA STRUCTURE

$$\vec{E}(x + p, y, z, t) = \vec{E}(x, y, z, t)e^{ik_{ix}p} \quad (3.3)$$

$$\vec{E}(x, y + p, z, t) = \vec{E}(x, y, z, t)e^{ik_{iy}p} \quad (3.4)$$

$$\vec{H}(x, y, z, t) = \vec{H}(x + p, y, z, t)e^{-ik_{ix}p} \quad (3.5)$$

$$\vec{H}(x, y, z, t) = \vec{H}(x, y + p, z, t)e^{-ik_{iy}p} \quad (3.6)$$

where p is the period along both x and y direction, k_{ix} and k_{iy} are the x and y components of the incident wavevector respectively. These two quantities explicitly depend on the angle of incidence but also on the frequency. Consequently, they can not be simply computed due to the temporal character of the FDTD (frequency is not fixed). To overcome this constraint, A. Belkhir developed an FDTD code based on Split-Field Method that allows the integration of the periodicity conditions after a variable changes of the electric and magnetic field components. The basic idea consists in integrating the exponential term appearing in these conditions in order to get similar periodic conditions as in the case of normal incidence. We suggest Ref. [149, 150, 99] to the reader for more details about this method. We only mention here that the variable change induced the introduction of 4 different Yee grids that involve more than 12 electric and magnetic field components. In addition, the implementation of the DCP dispersion model in this algorithm leads to introduce a large number of variables 12. Fortunately, the SFM-FDTD code integrating a DCP dispersion model was available by our team since the beginning of this part of my thesis work.

The first simulation results that were done through this code are presented in the Ref. [135]. Figure 3.8 shows a part of these results that were done to support the analytical findings in that paper. Later, A. Ndao experimentally studied the excitation of the TEM mode [139]. He performed experiments with AAA structures illuminated at oblique incidence and got TEM -based ET. Nevertheless, the magnitude of the observed transmission peak was very small due to the metal absorption and to the fact that the peak spectral position was in the vicinity of the TE_{11} one. In order to optimize the AAA geometry and to get efficient TEM -based transmission peak, it is important to make an overview on the electromagnetic modes that can be excited within the 2D periodic structure depicted in figure 3.9.

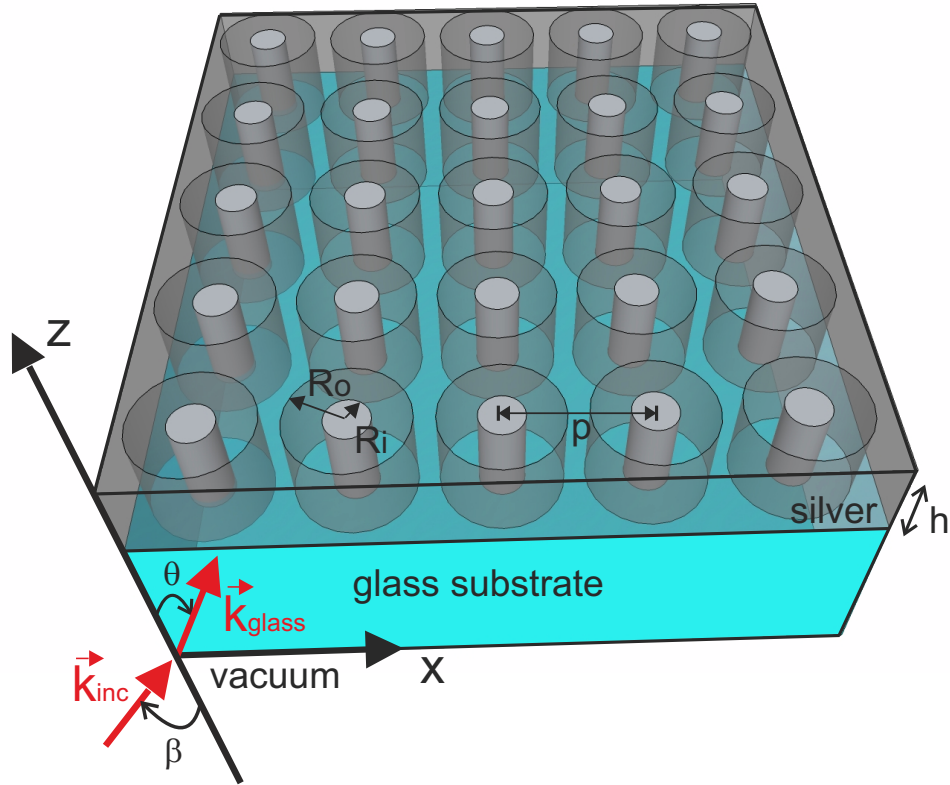


Figure 3.9: Schematic of a conventional Annular Apertures Array (AAA) structure. R_o and R_i are the outer and inner radius respectively, p the period and θ is the angle of incidence at the substrate-metal interface and β is the angle of incidence in the superstrate.

3.4.1/ CLASSIFICATION OF THE EM MODES WITHIN AAA

To better understand and describe the transmission spectra of an AAA, it is very important to point out all the mechanisms that are in play within this structure. As it is well-known, discontinuities can appear in the spectra and they generally correspond to Rayleigh and Wood anomalies due to the diffractive orders that match their excitation. The Rayleigh one is obtained when the diffracted wave-vector is tangential to the interface whereas the second corresponds to the surface plasmon excitation. For both cases, the tangential components of the wave-vector are given by the grating relations:

$$k_{dx} = k_{ix} + \frac{2\pi m}{p} \quad (3.7)$$

$$k_{dy} = k_{iy} + \frac{2\pi l}{p} \quad (3.8)$$

3.4. THEORETICAL STUDY OF THE EXCITATION OF TEM GUIDED MODE THROUGH AAA STRUCTURE

where k_{dx} , k_{dy} , k_{ix} and k_{iy} are the x and y components of the diffracted and incident wave-vectors respectively. The couple of integers (m, l) represent the diffractive orders. Consequently, Rayleigh and Wood anomalies are obtained when:

$$\sqrt{k_{dx}^2 + k_{dy}^2} = \frac{2\pi}{\lambda} \sqrt{\varepsilon_j} \quad \rightarrow \text{Rayleigh} \quad (3.9)$$

$$\sqrt{k_{dx}^2 + k_{dy}^2} = K_{sp} = \frac{2\pi}{\lambda} \Re \left[\sqrt{\frac{\varepsilon_m \varepsilon_j}{\varepsilon_m + \varepsilon_j}} \right] \quad \rightarrow \text{Wood} \quad (3.10)$$

where ε_m and ε_j with $j = 1, 2$ are the relative permittivities of the metal (silver for example) and dielectrics (substrate or superstrate) respectively. Assuming an incident wavevector \vec{k}_i in the xOz plane (see figure 3.9) and after projection along the Ox and Oy directions, one can express its two components by:

$$k_{ix} = \sqrt{\varepsilon_j} \omega/c \sin \theta \quad (3.11)$$

$$k_{iy} = 0 \quad (3.12)$$

Replacing k_{ix} and k_{iy} by their values in equation 3.9 and 3.10 allows writing them through the single following equation:

$$\lambda^2(m^2 + l^2) + 2m\lambda p \sqrt{\varepsilon_j} \sin \theta + p^2 \varepsilon_j \sin^2 \theta - p^2 \alpha = 0 \quad (3.13)$$

where θ is the angle of incidence and α becomes a constant which takes two values: $\alpha = \varepsilon_j$ in the case of Rayleigh anomaly, and $\alpha = \Re\left(\frac{\varepsilon_m \varepsilon_j}{\varepsilon_m + \varepsilon_j}\right)$ in the case of Wood anomaly.

In addition to these horizontal modes, there are guided vertical modes inside the annular apertures. In order to get efficient transmission based on the excitation of these vertical modes, their spectral positions must be far from the anomalies in order to avoid coupling between the two kinds of modes. Nevertheless, this coupling will lead to interesting phenomena but it is considered as out of scope in this work.

To avoid the coupling between horizontal and vertical modes, and to get ET at largest wavelength value than what it is commonly performed with the EOT structures, the TEM mode must be excited beyond the Wood anomaly corresponding to the SP at metal-substrate interface ($j = \text{glass}$). To fulfill this condition, the metal thickness will be large enough to allow verifying both Eqs. 3.2 and 3.10 and small enough to minimize the metal absorption. This enforce to work with the first harmonic ($m = 1$ in Eq. 3.2) interference of the TEM mode inside the vertical cavities (annular apertures).

3.5/ SIMULATIONS RESULTS

Our numerical simulations are based on a 3D-FDTD code integrating a critical points model to accurately take into account the metal dispersion [104]. We recall that our objective is to determine the most appropriate geometrical parameters of the AAA structure in view of experimentally demonstrate ET assisted by a TEM mode in the visible range. We will restrict our study to the case where the plane of incidence is always considered to be parallel to one periodic direction (here the xOz plane) (see Fig. 3.9). In fact, because of the aperture axis-symmetry, the transmission response is quasi-independent on the azimuthal angle (ϕ) [150] if the anomalies are far from the transmission peaks induced by the excitation of guided modes.

Two conditions are imposed in the design of the structure. First, the difference between the inner and outer diameter must be sufficient in order to facilitate the technological fabrication, and second, the metal plate must be thick enough in order to get the TEM mode in the visible range with $\lambda_{TEM} > \lambda_{TE_{11}}^c$. However, the metallic film thickness has to remain below a certain value in order to limit the absorption and to simplify the drilling during the fabrication process. Because gold is more absorbing in the visible range than silver, the latter has been preferred to the former to build our structure. The following sections are devoted to the optimization of the AAA structure by studying the influence of geometrical parameters on the transmission properties.

3.5.1/ INFLUENCE OF GAP ($R_o - R_i$)

First, zero order transmission spectra are calculated for different outer radius ranging from 100 nm to 150 nm. The inner radius is set to $R_i = 50$ nm corresponding to the smallest value that can be reached by the used etching technique (Focused Ion Beam) and ensuring a small value of $\lambda_{TE_{11}}$. The thickness of silver is set to $h = 200$ nm and the period of the array to $p = 400$ nm. These values of geometrical parameters result from the numerical study which is presented in the following. Normalized transmission spectra are plotted in Fig. 3.10 for an angle of incidence of $\theta = 20^\circ$ at the glass-metal interface corresponding to the maximum value of $\beta = 30^\circ$ for an incidence in air that is allowed by the experimental device (see Fig. 3.9). A large amount of light is transmitted through the structure between 600 nm and 800 nm : this high transmission is due to the excitation of the TE_{11} that occurs around its cut-off wavelength (here $\lambda_{TE_{11}}^c \in [690; 765]$ nm). Rayleigh and Wood anomalies also appear on the spectra due to diffractive orders that match their excitation. The wavelength (λ) of these diffractive orders is governed by the relations mentioned previously (see Eq.

3.13).

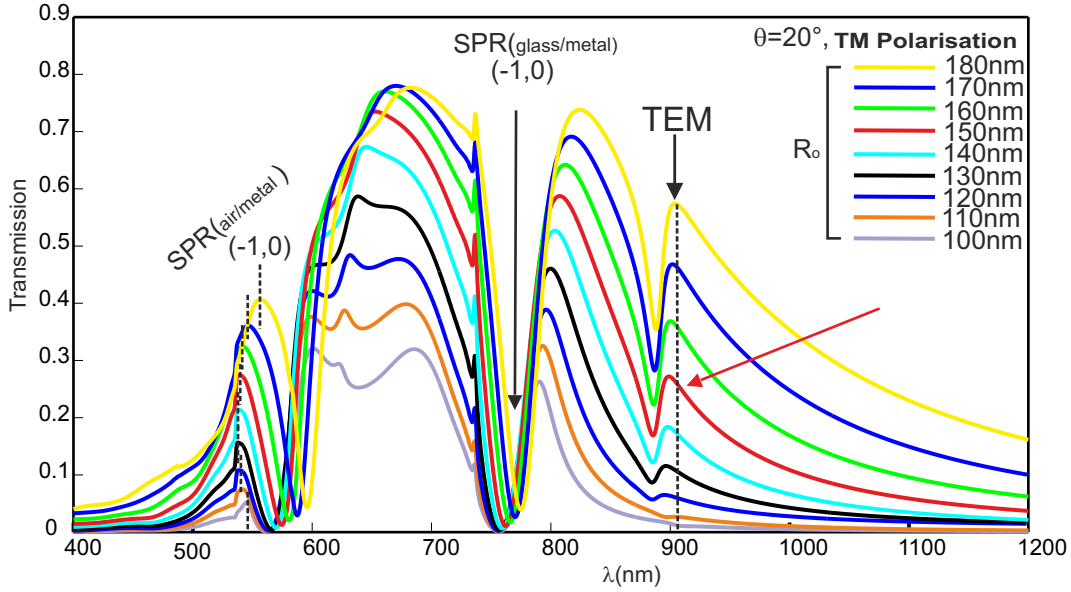


Figure 3.10: Theoretical transmission spectra for different outer radius R_o . The inner radius R_i is fixed to 50 nm , the period $p = 400 \text{ nm}$, the silver thickness is set to $h = 200 \text{ nm}$ and the incidence angle $\theta = 20^\circ$ (i.e. $\beta = 30^\circ$). The red arrow indicates the transmission spectra of the chosen parametric.

Thus, the discontinuities at $\lambda = 537 \text{ nm}$ correspond to the spectral position of the Rayleigh anomaly ($\alpha = 1$) on the air-metal interface while the two large dips are associated with the excitation of two diffractive orders $((m, l) = (0, -1))$ that match the SPR on the metal-air and metal-glass interfaces. Finally, the TEM peak occurs around $\lambda_{TEM} = 915 \text{ nm}$ corresponding to the first harmonic ($m = 1$ in Eq. 3.2). Its position is almost independent from R_o , but its amplitude increases with the latter. Indeed, the smaller the gap is, the more the mode is confined and the more it penetrates inside the metal, leading to a rise of the losses. Consequently, an efficient TEM -based transmission requires large outer radius. However, the value of R_o is limited by the period value and by $\lambda_{TE_{11}}^c$ which also increases to get closer and enhancing artificially the TEM peak. In fact, mode solver calculations demonstrate that the cutoff of the TE_{11} mode varies from $\lambda_{TE_{11}}^c = 665 \text{ nm}$ for $R_o = 100 \text{ nm}$ to $\lambda_{TE_{11}}^c = 827 \text{ nm}$ for $R_o = 180 \text{ nm}$. We have chosen $R_o = 150 \text{ nm}$ as a compromise to have efficient TEM peak together with a weak coupling with the TE_{11} mode. In addition, a very large value of R_o is prohibited since the distance between two successive apertures $(p - 2R_o)$ must be larger than 50 nm to be technologically realized.

3.5.2/ INFLUENCE OF THE METAL THICKNESS

The second important geometrical parameter is the thickness h of the metal plate which plays a key role in the TEM peak via the phase matching condition (see Eq. 3.2). As shown in figure 3.11, the larger h is, the more the spectral position of TEM peak is red-shifted: the position of the TEM peaks is proportional to the metal thickness but also to the effective index of the TEM guided mode traveling inside the apertures. Moreover, the transmission decreases when the thickness increases from 200 nm to 240 nm (see Fig. 3.11).

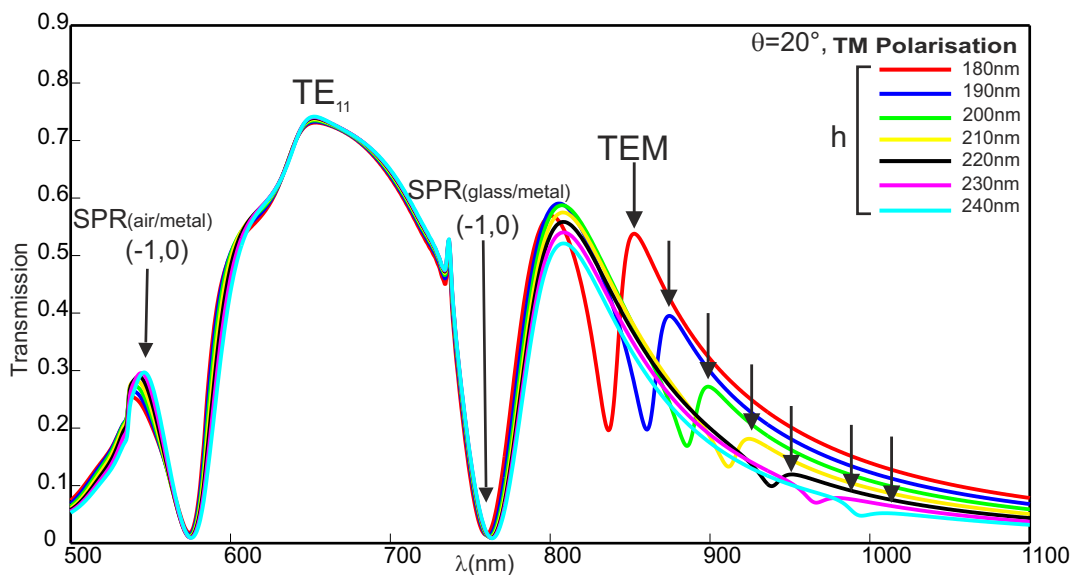


Figure 3.11: Zero-order theoretical transmission spectra through an AAA structure versus the height h of silver for a transverse magnetic (TM) polarization illuminated at $\theta = 20^\circ$ (i.e. $\beta = 30^\circ$). The other geometrical parameters are $R_i = 50 \text{ nm}$, $R_o = 150 \text{ nm}$, $h = 200 \text{ nm}$ and $p = 400 \text{ nm}$.

Once again, this is due to the metal absorption that increases with longer propagation distance. At first glance, this seems contradictory with the fact that metal becomes less absorbing when the wavelength increases. In fact, there is a competition between two effects: the first one is the red-shift of the TEM peak spectral position leading to smaller imaginary part of the metal permittivity while the second is directly linked to the propagation distance that becomes longer and to the variations of imaginary part of the effective index of the TEM mode. According to Fig. 3.11, the second effect is predominant because the TEM -based transmission peak amplitude decreases for larger thicknesses. One notes that the peak corresponding to the TEM mode is narrower than the peak corresponding to the TE_{11} mode conferring the property of being more adapted for some

applications such as spectral filtering.

3.5.3/ INFLUENCE OF THE PERIOD

Finally, the last important parameter is the structure period. Figure 3.12 shows the transmission spectra for four different values of the period. As expected, this greatly affects the anomalies position. Moreover, we choose the larger value of the period for which the anomalies are far from the spectral range of the *TEM*-based transmission peak. This was verified by reporting the analytical value of the anomaly position, obtained through the equation 3.13, on the calculated spectra. As seen in figure 3.12, the black arrow corresponding to that SPR fits well the dip position since $p \leq 400 \text{ nm}$. Coupling with the guided modes appears for larger value of the period and leads to a red shift of the dip. Consequently, we have fixed the value of the period to $p = 400 \text{ nm}$.

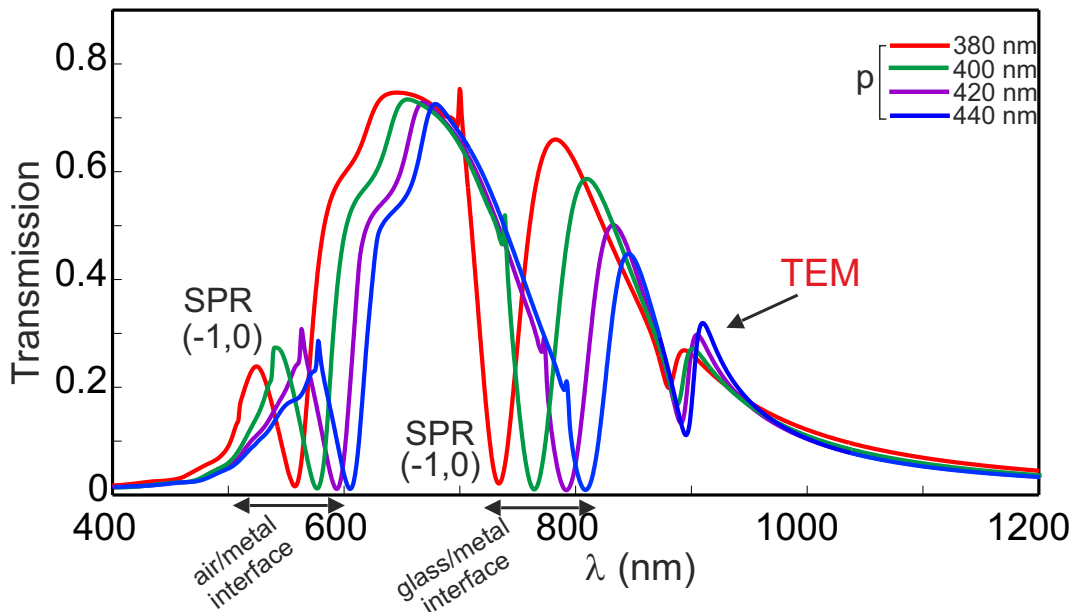


Figure 3.12: Theoretical transmission spectra for different period p values. The inner radius R_i is fixed to 50 nm , $R_o = 150 \text{ nm}$, $h = 200 \text{ nm}$ and the incidence angle $\theta = 20^\circ$ (i.e. $\beta = 30^\circ$).

Given the experimental constraints, this theoretical study leads to the optimum parameters for an efficient transmission through an AAA thanks to a plasmonic *TEM* mode: $h = 200 \text{ nm}$, $R_o = 150 \text{ nm}$, $R_i = 50 \text{ nm}$, $p = 400 \text{ nm}$ and the incidence angle must be as large as possible.

3.6/ THE MEASURED AND SIMULATED TRANSMISSION OF AAA

This section is devoted to compare the measurement of the light transmission through AAA structure whose transmission properties are described in the previous section. Once the simulation results become available, it is possible to do the process of the fabrication of the design depending on the information obtained theoretically. We review the description of this fabrication and the way of the recorded transmission, measurements of transmission coefficients without delve into the fine details because the experimental part is out of scope of this thesis.

3.6.1/ BRIEF DETAILS OF THE SAMPLE FABRICATION

The fabrication of this structure has been performed in the context of A. Ndao's thesis. [139]. For this purpose, Focused Ion Beam (FIB) milling combined with a very accurate metal deposition process has been used. It allows building a structure with very small radii. A 5 nm thin chromium layer is deposited on the glass substrate (index $n = 1.51$) as an adhesion layer. Next, a silver film (thickness $h = 200$ nm) is deposited by evaporation. Finally, the structure grating is obtained by FIB milling of the metallic layer. A Scanning Electron Microscopy (SEM) images of a fabricated matrix of 30×30 annular apertures is presented in Fig. 3.13(a). Two enlargements made on Fig. 3.13(a) with different viewing angles are presented in the Figs. 3.13(b) and (c) in order to check the good surface quality. For checking the quality of the apertures along the metal thickness, a vertical cutting of the structure parallel to the xOz plane passing through the center of the aperture is presented in Fig. 3.13(d). More details on the quality of the fabrication including extended demonstrations are presented in [139].

3.6.2/ COMPARISON BETWEEN THEORY AND EXPERIMENT

For the spectrum normalization, the transmission coefficients are theoretically and experimentally defined as the ratio of the transmitted intensity of the diffracted zero order through the structure to the same quantity measured through a reference area. The latter is a large square aperture having the same lateral size ($12 \times 12 \mu\text{m}^2$) as the whole array of nano-apertures that are engraved in the same metallic film.

Transmission spectra are recorded for three different incidence angles in the context of thesis of A. Ndao. but we only present here the result of one value ($\theta = 20^\circ$). This result

3.6. THE MEASURED AND SIMULATED TRANSMISSION OF AAA

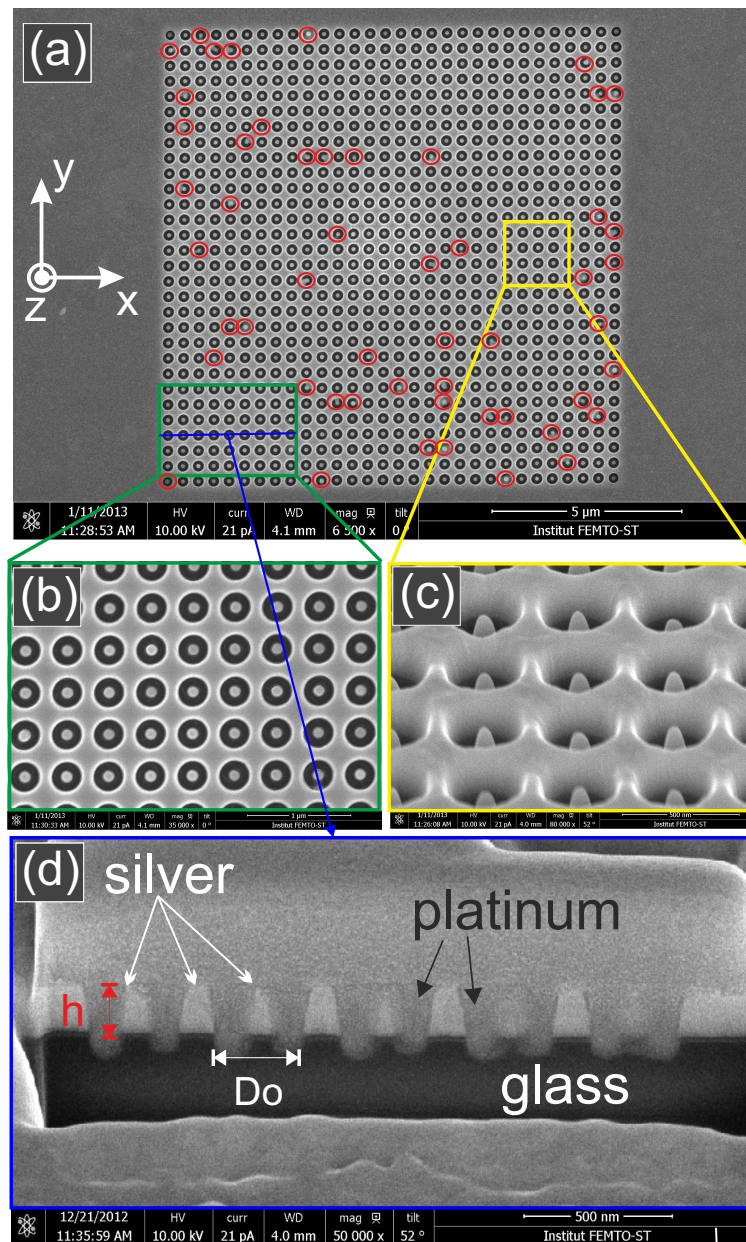


Figure 3.13: (a) SEM top view image of the studied AAA (30×30 apertures) engraved in silver film. (b) zoom-in over 6×9 patterns. (c) 52° tilted zoom-in over 4×4 apertures. (d) Vertical cross-section made on the structure after it was filled in with platinum. Ref. [139]

is compared to the theoretical calculations in Fig. 3.14. As it can be seen from figure 3.13, some fabrication imprecision occurs and leads to different geometrical parameters than those of the designed structure. To take into account these slight modifications geometry, the geometrical parameters of the simulated structure were adapted to those obtained

from SEM images of Fig. 3.13. More precisely, the inner and outer radii are fixed to $R_i = 50 \text{ nm}$ and $R_o = 145 \text{ nm}$ instead of 150 nm respectively, and the metal thickness to $h = 190 \text{ nm}$ instead of 200 nm . The comparison is made for both TE and TM incident polarizations at $\theta = 20^\circ$. Experimental and theoretical spectra of figure 3.14 are in good agreement in terms of the peak position and amplitude. Nevertheless, the technological process produces samples with periods and aperture diameters slightly different from one pattern to the other. In addition, when looking closely to Fig. 3.13(a) (see the red circle), one can see that 52 apertures among the 784 that the AAA contains are almost not completely opened. This obviously leads to cancel the *TEM* guided mode excitation inside these apertures and affects the transmission amplitude of the TEM peak. Unfortunately, FDTD simulations exploiting periodic boundary conditions can not support such a structure. All this can explain the small discrepancies between the theoretical and experimental results of Fig. 3.14. The main broad peak in two curves of Fig. 3.14 is attributed to the TE_{11} mode excited at its cutoff wavelength $\lambda_{TE_{11}}^c \simeq 751 \text{ nm}$. This transmission peak position remains the same independently at the incidence angle [150].

However, the most interesting feature is the presence in the transmission spectrum for $\theta = 20^\circ$ (Fig. 3.14(a)) of a small peak located at $\lambda = 915 \text{ nm}$. This peak is due to the excitation of the *TEM* mode. Indeed, as expected, this peak does not exist under normal incidence and it disappears if the polarization is turned to *TE* (Fig. 3.14(b)). Nevertheless, its position is independent of the incidence angle since it is far from the anomalies. The absorption along the $h = 200 \text{ nm}$ of the metal thickness prevents the *TEM* peak from having a larger amplitude. Unfortunately, the set-up could not allow the incidence angle to be increased beyond $\beta = 30^\circ$ (corresponding to $\theta = 20^\circ$) which could have further enhanced the *TEM* peak amplitude.

3.7/ CONCLUSION

In this chapter, we have reviewed the state of the art achieved on Extraordinary Optical Transmission (EOT) and the basic principle of waveguides have then outlined in terms of the dispersion diagram of fundamental guided modes. A theoretical study of the excitation of *TEM* guided mode through AAA structure has been conducted. We have performed extensive numerical simulations based on a 3D-FDTD homemade code where the DCP dispersion model is adapted to accurately describe the dielectric constant of the considered metals. We have reported the influence of: the cavity gap, metal thickness, and the period on ET. We have been able to get the preferable parameters for an efficient transmission through an AAA structure. Consequently, the demonstration of the simulation

3.7. CONCLUSION

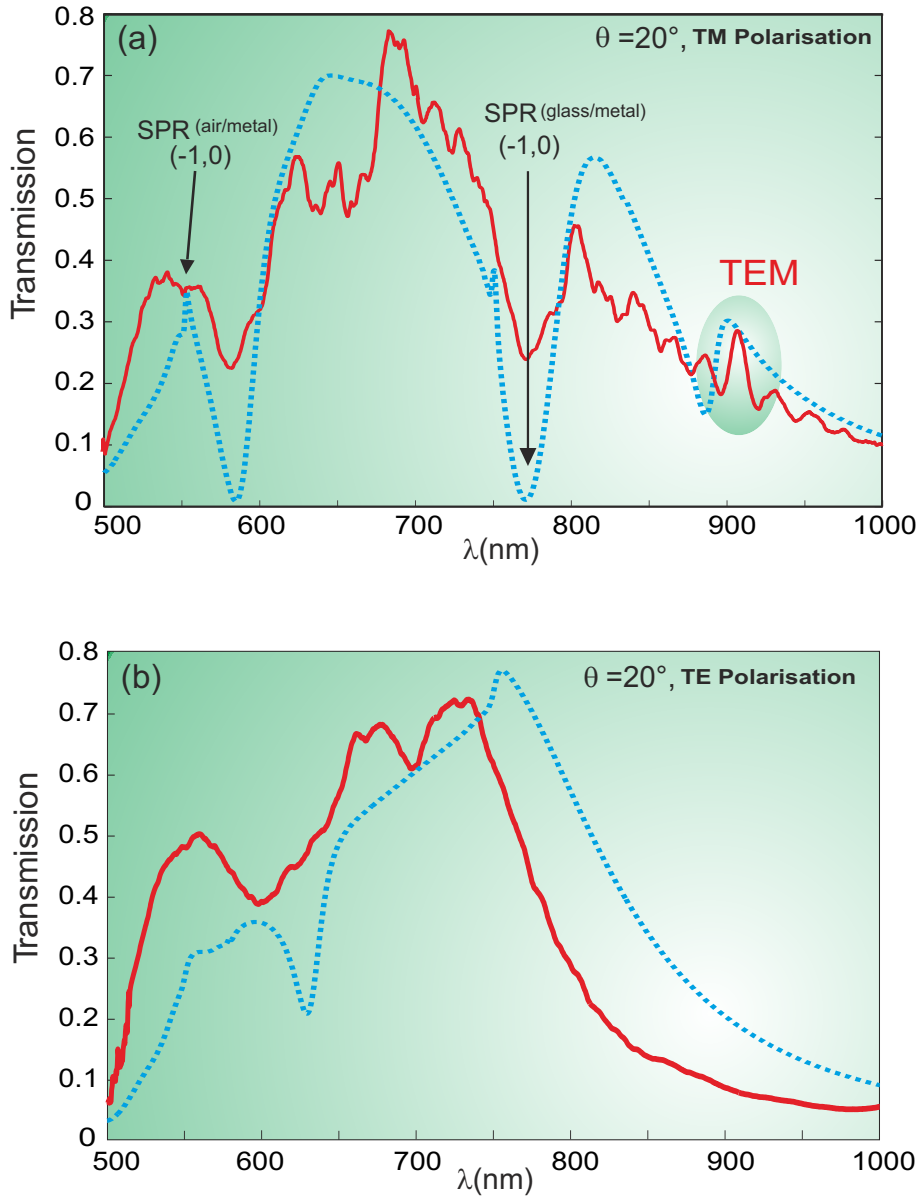


Figure 3.14: Experimental (solid line) and theoretical (dashed line) transmission spectra at $\theta = 20^\circ$ (i.e. $\beta = 30^\circ$) through an AAA made in silver for both (a) TM and (b) TE polarizations. Numerical simulations are performed with the geometrical parameters : $R_i = 50nm$, $R_o = 145nm$ and $h = 190nm$. The vertical arrows show surface plasmons resonance (SPR) positions and the colored area marks the position of the peak due to the excitation of the TEM guided mode. The TEM mode is only excited with a TM polarization: no peak appears around 900 nm in TE polarization.

results have somewhat ensured and facilitated the AAA fabrication process and hence the characterization of the experimental construction of AAA structure has been undertaken. Our numerical studies have revealed that, for the first time to our knowledge, the ET assisted by a TEM mode in the optical regime can be excited inside the apertures under oblique incident TM polarized light. This mode has no cut-off wavelength, therefore,

annular nano-apertures can transmit light at wavelength much larger than their external diameter ($\lambda_{TEM} = 6R_o = 2.3p$ in our case). However, the TEM peak amplitude remains low because of metal absorption but it can be increased with large incidence angles and/or by stretching out the inner part from the metallic layer as shown in ref. [93] (see figure 4c of that paper) where this point will be the focus of our attention in the next chapter. Nevertheless, in the case of the AAA structure, the propagation constant of the TEM mode is always larger than the freely propagation one (plasmonic character) meaning that it does not allow slow light propagation nor enhancing of non-linear effects as it can be done within the TE_{11} one [151]. By the way, the TEM mode becomes complementary to the TE_{11} one. Despite everything, the TEM mode of AAA structures leads to efficient transmission in the domain of terahertz waves or microwaves where metal absorption is negligible.

TRANSMISSION PROPERTIES OF SLANTED ANNULAR APERTURE ARRAYS (SAAA)

In the previous chapter, we theoretically demonstrated an enhanced transmission ET through annular aperture arrays AAA by the excitation of the peculiar transverse electromagnetic (*TEM*) guided mode. We have performed a numerical study to correctly design the structure seeking the optimal performance before it is experimentally characterized. As explained in chapter 3, two conditions require to be fulfilled in order to excite the *TEM* mode that is often experimentally difficult to allow efficient transmission at oblique incidence. The fabrication process has been constrained with some limits associated to the angle of incidence and the thickness of metal. It was experimentally found that maximum value of the angle of incidence can reach to 30° [139]. For most of applications, it is best to get a more efficient transmission (i.e. in the visible and near-IR) through the *TEM* mode assuming an operation wavelength larger than the TE_{11} one. To overcome this constraint, an alternative solution was carried out by J. J. Greffet team [152]. They proposed a geometric evolution of the profile of the cavities, to favor a wide-band behavior. The suggestion was to incline the apertures instead of tilting the whole structure and/or the incident beam. In 2010, Baida F. et al. have presented a pure theoretical study of such structures called Slanted Annular Aperture Arrays (SAAA), to demonstrate their potential [93]. In that paper, the transmission of *TEM* guided mode was numerically predicted for several configurations. Unfortunately, the ET based on the *TEM*-mode excitation remains very small ($\sim 15\%$ at normal incidence) for an easy-fabrication SAAA structure (see figure 4b of ref. [93]).

After an overview on the ET through SAAA for applications in the visible and NIR do-

mains, pointing out the limitations due to the losses induced by the real nature of metals, we will restrict our study to the case of SAAA made in perfectly conducting metal. We will numerically and analytically describe some intrinsic properties of the structure as a function of its geometry. Moreover, we will bypass the excitation of the TE_{11} mode, that was already discussed in details in [29] and the references therein.

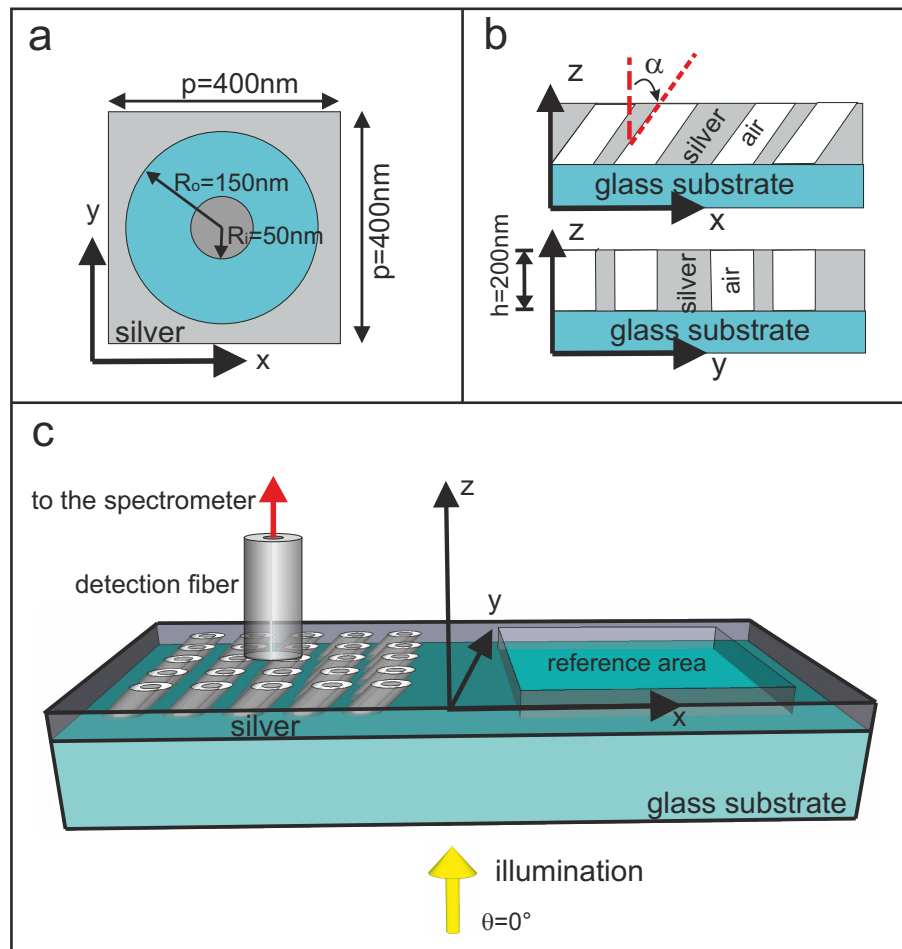


Figure 4.1: (a) Schematic of one annular aperture section in the xOy plan giving the geometrical parameters (outer radius $R_o = 150 \text{ nm}$, inner radius $R_i = 50 \text{ nm}$). (b) Schema of the xOz and yOz sections showing the metallic film with thickness $h = 190 \text{ nm}$ perforated with SAAA. Note that the tilted angle $\alpha = 30^\circ$ of the aperture axis belongs to the xOz plan. (c) Sketch of the whole sample with SAAA structure and the reference zone used to normalize the transmitted signal. Ref. [153].

4.1/ A HISTORICAL OVERVIEW OF THE CHARACTERIZATION AND FABRICATION OF SAAA STRUCTURE

Recently, the experimental demonstration of an ET associated with the excitation of the TEM mode of the SAAA structure (depicted in Fig. 4.1) was addressed by A. Ndao et al. [153]. The fabricated structure consists of annular apertures with axes tilted by an angle $\alpha = 30^\circ$ normal to a $h = 190 \text{ nm}$ thick silver layer (see Fig. 4.1(b)). This value of thickness is necessary to, at least, shift TEM -based transmission peak away from the TE_{11} -based one (see phase matching condition Eq. 3.2). As already mentioned, the choice of the array period plays an important role to move away the Wood's and Rayleigh's anomalies from the spectral range where the TEM guided mode is excited (see Eqs. 3.9 and 3.10 in Ch.3).

The numerical simulations of different geometric parameters for the SAAA structure for both silver and PEC were previously presented in [139]. The influence of outer and inner radii was also addressed in order to explore their effects on the position and the amplitude of the TEM -based peak and hence to be the best characterized (see figure 4.2). This study shows high dependence of the peak spectral position with the value of the inner radius. More specifically, the peak shifts towards the red region as R_i increases for both real and perfect metals (see figure 4.2(a,b)), this shifts is attributed to two different factors: (a) the growth in the TEM guided mode effective index as the gap decreases and (b) to the modification (increase) of the reflection phase at the ends of the apertures (see figure 8(a) of Ref. [145]; [93]). Nevertheless, in the case of PEC structure where the effective index of the TEM guided is equal to 1 whatever the radii values, the shift is only linked to the second factor. Consequently, smaller shifts occur in the case of PEC as shown in Fig. 4.2(a). A $\Delta R_i = 25 \text{ nm}$ leads to $\Delta \lambda_{TEM} = 150 \text{ nm}$ for PEC and $\Delta \lambda_{TEM} = 230 \text{ nm}$ for silver. Similarly, the influence of the outer radius was studied and it was found that decreasing R_o , the TEM -based peak of a PEC structure shifts to blue spectral region (see Fig. 4.2(c)). This behavior is directly related to the variation in the phase ϕ_r of the reflection at the aperture ends. Contrarily to the case of PEC where the shift is quite proportional to R_o , the silver case presents a more complicated behavior (see Fig. 4.2(d)) due to the fact that increasing R_o allows coupling between adjacent aperture TEM modes. This coupling occurs not only at the interfaces (up and down) but also through the metal part that exists between the apertures. In this case, the dispersion diagram of the TEM mode becomes different from the one of a unique waveguide, i.e. a collective effect appears as depicted in figure 1.28(b) of Ref. [144].

According to these results, and in the perspective of experimental demonstration,

4.1. A HISTORICAL OVERVIEW OF THE CHARACTERIZATION AND FABRICATION OF SAAA STRUCTURE

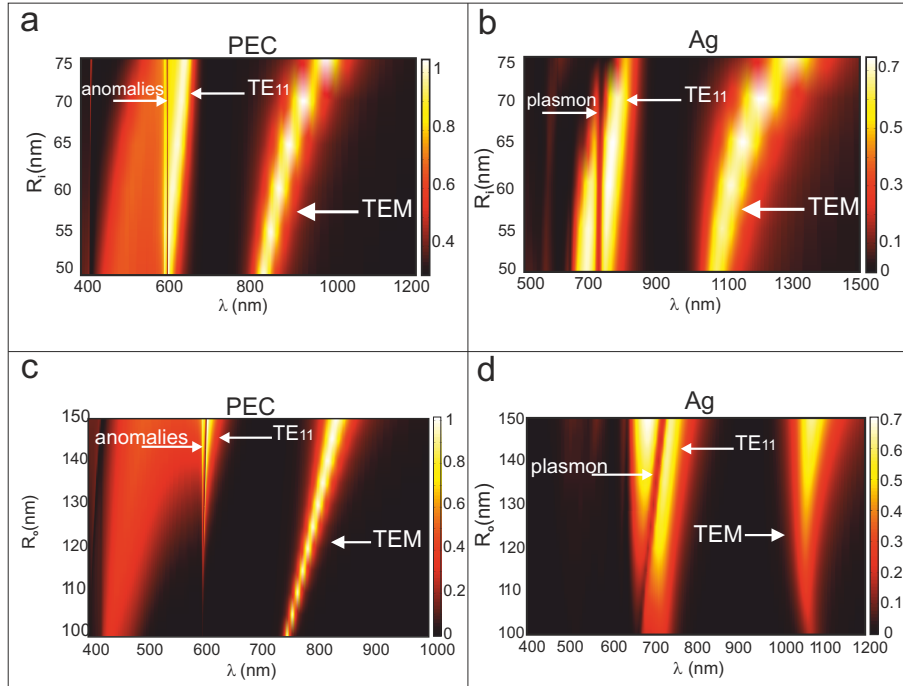


Figure 4.2: (Top) Study of the influence of the inner radius in perfect conductor (a) and real metal (silver) (b). The outer radius is fixed to $R_o = 150 \text{ nm}$. (Bottom) Study of the influence of the outer radius in perfect conductor (c) and real metal (silver) (d). The inner radius is fixed to $R_i = 50 \text{ nm}$. Note that The structure is illuminated by a linearly TM polarized plane wave at normal incidence with an angle of inclinations $\alpha = 30^\circ$ and the period equal to $p = 400 \text{ nm}$. Ref. [139].

Ndao A. envisaged two different metals for the fabrication of the structure; namely silver and gold due to their good performances in the visible and NIR spectral ranges. In this context, it was appropriate pointing out the dispersion diagram of the TE_{11} and the TEM mode of an infinitely-long coaxial waveguide, within the geometrical parameters deduced from the study performed above ($R_i = 50 \text{ nm}$, $R_o = 150 \text{ nm}$). The TE_{11} mode was considered in order to ensure large spectral separation with the TEM mode. The dispersion of these two modes is calculated using a homemade BOR-FDTD code that was adapted to determine the eigenmodes of a structure exhibiting a cylindrical symmetry [27]. The DCP dispersion model of gold and silver was implemented with the parameter values given in tables 2.1 and 2.2 in page (31 and 31) respectively. Consequently, the effective index, real and imaginary parts, of the two guided modes were obtained from the calculated electromagnetic spectral density. As expected, for both silver and gold, TE_{11} mode exhibits a hybrid character: conventional propagating guided mode (over the light line) and plasmonic one (under the light line). Whereas, the TEM mode is only a plasmonic one (see figure 4.3(b)). As it is well known, when light propagates as a guided wave it experiences some propagation losses. According to the results of Fig. 4.3(c and d), silver is

most suitable, instead of gold due to a smaller imaginary part of the effective index of its TEM mode. Nevertheless, one can expect that the transmission efficiency of the TEM peak will be smaller compared to the TE_{11} peak due to the fact that the latter is always excited at its cutoff wavelength involving very small losses ($n_{eff}^{TE_{11}} = 3 \times 10^{-2}$ as seen in Fig. 4.3(c)), while the TEM mode exhibits smaller values ($n_{eff}^{TEM} \simeq 0.015$ at $\lambda = 1550$ nm). To optimize the transmission efficiency based on the excitation of the TEM mode, it is necessary to choose an operation wavelength around 900 nm (see Fig. 4.3(d)).

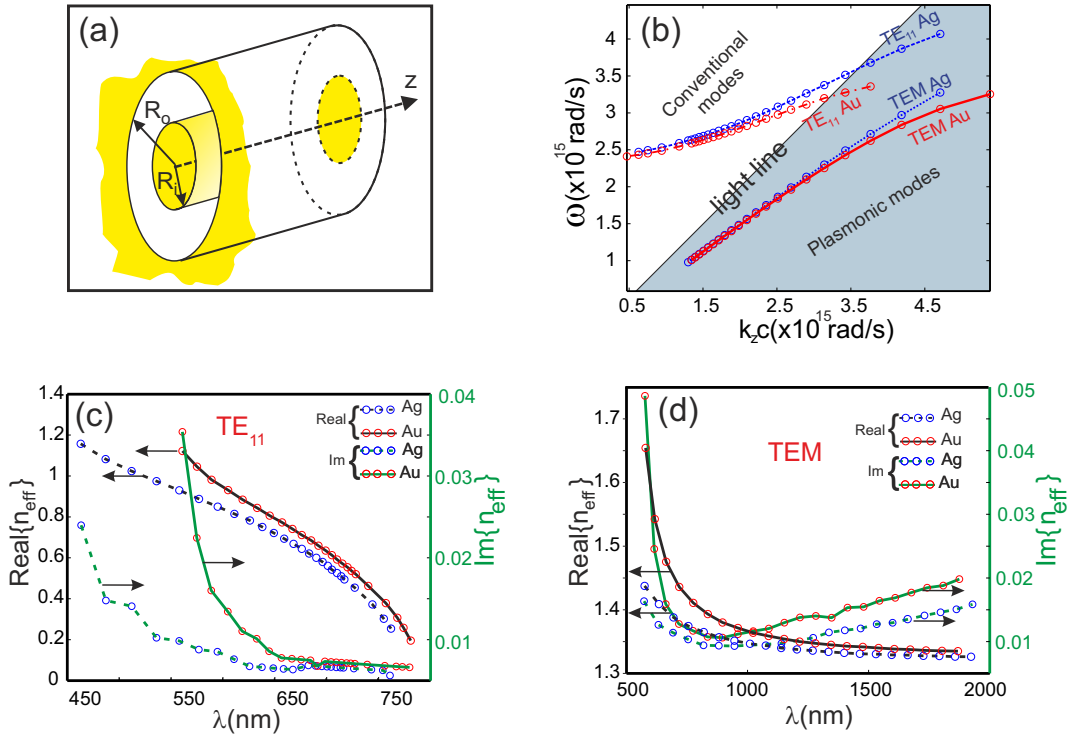


Figure 4.3: (a) Schematic of the infinite coaxial waveguide considered for the determination of the real and imaginary part of the effective index and the dispersion diagram of the TE_{11} and the TEM guided modes. (b) Dispersion curves for waveguides made in gold (red lines) or silver (blue lines) when $R_i = 50$ nm and $R_o = 150$ nm. (c) Real part (black curves: Ag in dashed and Au in solid lines) and imaginary part (green curves: Ag in dashed and Au in solid lines) of the effective index of the TE_{11} mode calculated from (b). (d) corresponding curves as in (c) for the TEM mode. Ref. [153].

The fabrication of this structure was performed in the context of A. Ndao's thesis [139]. The focused ion beam (FIB) milling combined with very accurate metal deposition has been used. Thereafter, a silver film with thickness $h = 190$ nm is deposited by evaporation, and the SAAA grating is gained using FIB milling of the metallic layer. Figure 4.4 shows the good quality of the fabrication and the geometric parameters of the sample that has been checked using scanning electron microscopy images (SEM). As shown in figure 4.1, the angle of inclination of slanted apertures was set to $\alpha = 30^\circ$ in the xOz plan

4.1. A HISTORICAL OVERVIEW OF THE CHARACTERIZATION AND FABRICATION OF SAAA STRUCTURE

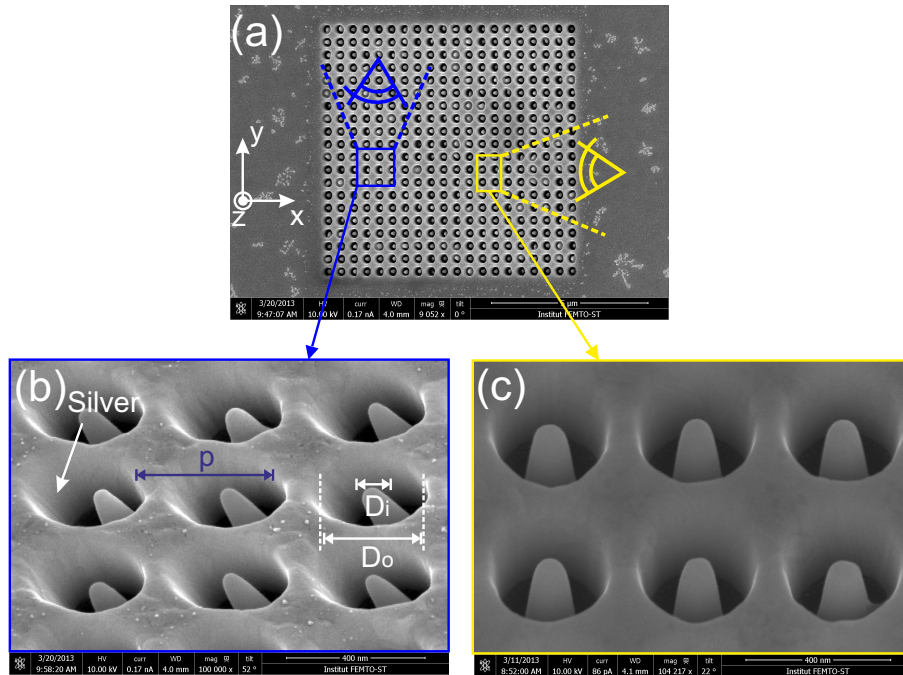


Figure 4.4: Top view SEM image of the studied SAAA matrix engraved in silver film. (b) is a zoom-in made over 3×3 patterns imaged in the O_y direction to point out the slanted apertures. (c) is a zoom-in made over 3×2 apertures in the O_x direction. Ref. [153].

(angle between the annular aperture axis and the perpendicular to the metal film). A top view SEM image of the whole fabricated array (i.e. a matrix of 20×20 annular apertures) is presented in figure 4.4(a). As well, figure 4.4(b) is side view SEM image from O_y direction that clearly shows the slanted apertures whereas, figure 4.4(c) is obtained in the O_x direction. For more details about the checking of the quality and the processes of fabrication of the apertures along the metal thickness, the reader can be referred to Ref. [153].

To investigate the transmission spectra for the fabricated SAAA structure, the zero-order transmission for both the recorded experimental transmission and the correspondent theoretical simulations are presented in figure 4.5. A good agreement between theory and experiment was obtained. The TE_{11} guided mode is efficiently excited with transmission efficiency more than 70% located around its cutoff wavelength ($\lambda_{TE_{11}}^c \simeq 707 \text{ nm}$). In fact, this transmission value was less than the one obtained by Poujet et al. [141] because of the metal thickness (i.e. the propagation distance) that is here larger ($h = 190 \text{ nm}$ instead of 100 nm). Furthermore, another transmission peak occurs at ($\lambda^{TEM} \simeq 935 \text{ nm}$) thanks to the excitation of the TEM guided mode inside the apertures. The nature of this peak (TEM guided mode excitation) was experimentally confirmed by the fact that it only occurs for TM polarization of the incident illumination. Nevertheless, as shown in Fig.

4.5(a), there was a difference between theory and experiment in terms of transmission efficiency. However, both the measurement and simulation results are qualitatively very comparable, whereas the small discrepancy is linked to the fabrication imperfections that are induced by the used technological processes as explained in Ref. [139].

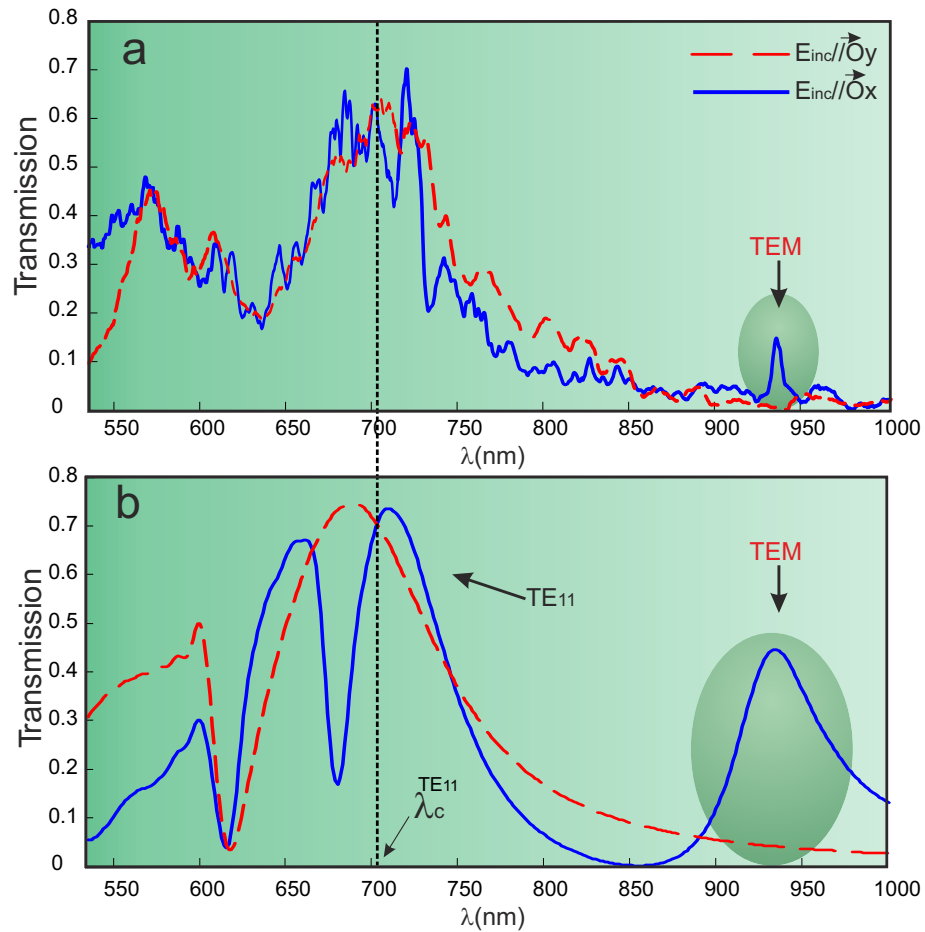


Figure 4.5: Zero-order (a) experimental and (b) theoretical transmission spectra of the SAAA structure as a function of wavelength for the two cases of polarization: $E_{inc} // O_x$ (solid blue line) and $E_{inc} // O_y$ (dashed red line). The TEM guided mode is only excited when the incident electric field has a non-zero component along the aperture axis (here TM polarization). Ref. [153].

In brief, the review of the recent study of SAAA described above shows that the TEM mode is excited at normal incidence and its spectral position is expected to be red-shifted compared to the conventional AAA structure. In fact, due to the inclined path through the metal film, the effective thickness of the cavities is increased and the phase matching condition can be fulfilled for larger values of the wavelength. Unfortunately, the TEM -based transmission in the visible range was weak due to metal losses and to the fact that this TEM mode is spatially extended in the metal more than the TE_{11} mode. Therefore,

4.2. COMPARISON BETWEEN AAA AND SAAA

in this chapter, we will address theoretical and numerical simulations through 3D-FDTD algorithm only in case of microwave and THz domain where metals can be considered as PECs leading to an efficient transmission. In the next section, we discuss in detail the difference between the AAA structure and the SAAA one in terms of their transmission. Due to the interesting transmission properties through the SAAA structure, a more detailed study on this structure on the basis of both numerical and analytical calculations will be performed in the following. The investigating of the influence of angle of inclination α , incidence θ and azimuthal ϕ on the transmission spectra is conducted. Then, we present an exhaustive demonstration of the transmission characteristics in terms of the couple (θ and ϕ). Finally, the analytical treatment of an arbitrary SAAA configuration to reinforce our numerical results is supported.

4.2/ COMPARISON BETWEEN AAA AND SAAA

As already mentioned, the *TEM*-based transmission in the visible range was weak due to metal losses and to the fact that this *TEM* mode is spatially extended in the metal more than the *TE*₁₁ mode. In this section we present a numerical simulations study through homemade 3D-FDTD algorithm to compare the transmission spectra of an AAA and an SAAA having the same geometrical parameters.

Figure 4.7 a depicts the schema of the two studied structures and gives all the geometrical parameters. Note that due to the non-dispersive character of all the considered media, reduced parameters are used with p unit where p is the period of the structure. The AAA structure is illuminated at oblique incidence with an angle of incidence equals to the tilt angle ($\theta = \alpha = 30^\circ$) of the SAAA structure while this later is illuminated at normal incidence. The incident polarization is TM (magnetic field perpendicular to the plane of incidence); As shown in figure 4.7(b) the *TEM*-based transmission peak appears and reaches 100% for both structures. Nevertheless, as expected, its spectral position is significantly red-shifted when the apertures are tilted. Indeed, since the Rayleigh anomaly is far from the spectral position λ_{TEM} of the *TEM*-based transmission peak (structure period $p < \pi(R_i + R_o)$), λ_{TEM} can be given by a phase matching relation:

$$\lambda_{TEM} = \frac{4\pi n_{eff} h_{eff}}{(2m\pi - \phi_r)} \text{ with } \{h_{eff} = h \text{ for AAA}\} \text{ and } \{h_{eff} = h/\cos(\alpha) \text{ for SAAA}\} \quad (4.1)$$

m is a non-zero positive integer, n_{eff} is the real part of the effective index of the *TEM* mode ($n_{eff} = 1$ if perfect conductor) and ϕ_r is the phase change due to the mode reflection (and diffraction) at the input or the output sides of the aperture. Let us recall that α is the

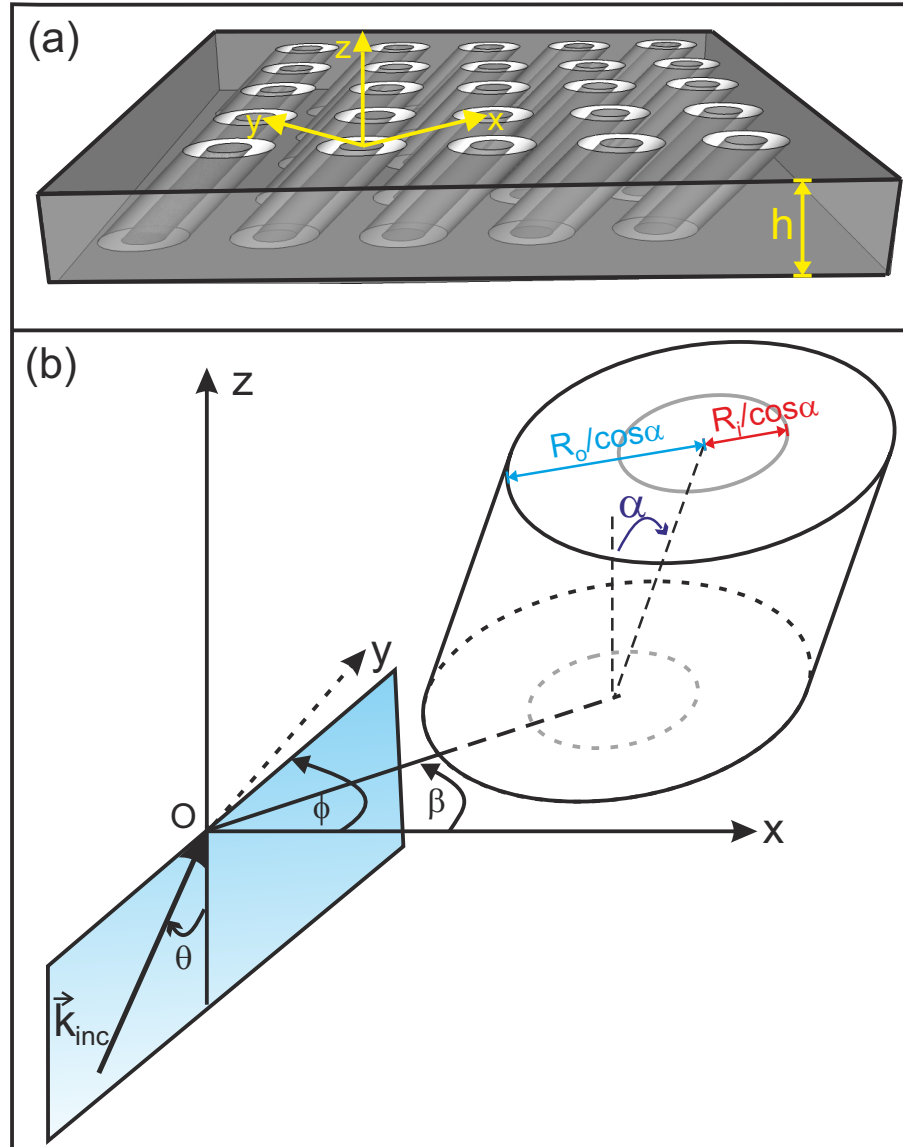


Figure 4.6: (a) 3D view of the Slanted Annular Aperture Array (SAAA) structure under consideration. (b) Schema showing the different geometrical parameters used to assign the incident wave-vector position (in the plane formed by the Oz axis at an angle ϕ from the Ox axis) and direction (incidence angle θ counted from the Oz axis). The aperture axis is tilted by an angle α from the vertical direction (Oz) in a plane also located at an angle β from the Ox axis). The horizontal section of an aperture has then outer (inner) ellipses with minor half axis R_o (R_i) and major $R_o/\cos\alpha$ ($R_i/\cos\alpha$).

angle of the aperture tilt counted from the normal to the metal interface. The position of the TEM peak can then be tuned through the tilt angle for a fixed value of the thickness. Nevertheless, this dependence is not completely explicit because the phase term (ϕ_r) can also depend on α . Furthermore, the quality factor Q of the TEM transmission peak for the two configurations are calculated and it is found that the $Q_{AAA} = 122.78$ and $Q_{SAAA} = 45$. Consequently, the low quality factor of SAAA can be useful for broad-band applications

4.3. INFLUENCE OF ANGLE OF INCLINATION ON THE TRANSMISSION SPECTRA

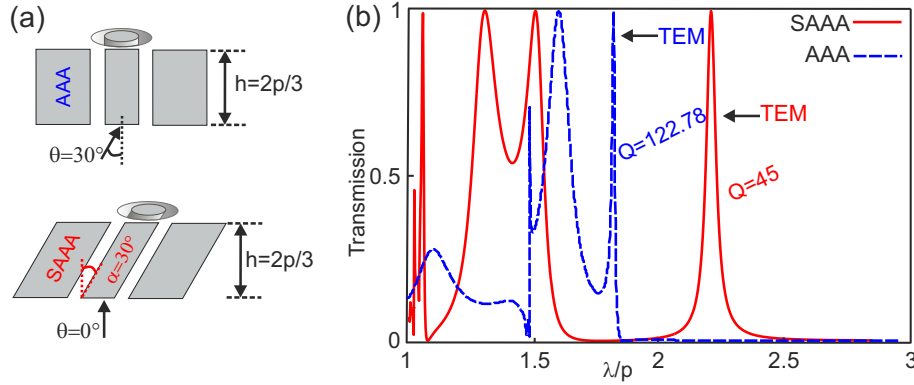


Figure 4.7: Calculated transmission spectra for two different configurations (a) having the same metal thickness $h = 2p/3$ where p is the period along Ox and Oy directions. (b) The red curve represents the transmission through the SAAA structure at normal incidence while the blue one corresponds to the transmission through the AAA structure. For both structures, we consider a TM polarized incident plane wave with $\phi = \beta = 0^\circ$ (see Fig. 4.6) but $\theta = 0^\circ$ and $\alpha = 30^\circ$ for the SAAA structure and $\theta = 30^\circ$ in the case of the AAA structure. For the two configurations, we fixed the radii values to $R_o = p/3$ and $R_i = p/6$.

while the AAA structure is more appropriate for spectral filtering applications, chemical sensing, biology and enhanced Raman spectroscopy.

4.3/ INFLUENCE OF ANGLE OF INCLINATION ON THE TRANSMISSION SPECTRA

This study is performed in order to gain more insight and to see how the angle of inclination affects the phase term (ϕ_r). For this purpose, we have studied the transmission response as a function of α at a fixed value of the thickness $h = 2p/3$ and in the case of normal incidence. In both cases, the radii of the annular aperture are fixed to $R_o = p/3$ and $R_i = p/6$ and $\beta = 0$ meaning an inclination axis parallel to the xOz plane. The results are plotted in figure 4.8(a) for α varying from 5° to 45° . As expected from equation 4.1, the TEM peak position shifts to the red region of the spectrum when α increases ($1/\cos \alpha$ increases). Figure 4.8(b) depicts the spectral positions of the TEM peak as a function of $1/\cos \alpha$ (solid blue curve). An almost linear behavior is obtained meaning that the phase ϕ_r is quite constant when α varies. The slight discrepancy appearing at small values of α between the numerical calculation and that obtained from equation 4.1 when considering $\phi_r = 1.9$ rad (dashed red line), can be attributed to the coupling between the TEM and the TE_{11} modes.

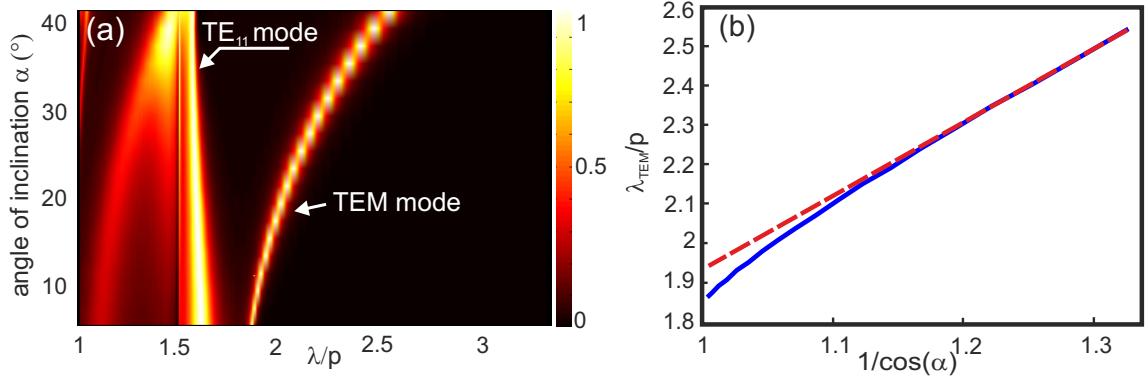


Figure 4.8: (a) Transmission spectra in color level versus the tilt angle α of a SAAA with metal thickness $h = 2p/3$ (p is the period of the grating along the Ox and Oy directions), the inner and outer radii of the coaxial cavities are $R_i = p/6$ and $R_o = p/3$ respectively. The structure is illuminated by a TM polarized plane wave at normal incidence with $\phi = \beta = 0^\circ$. (b) The solid blue curve is the spectral position of the TEM -based transmission peak function of $1/\cos(\alpha)$. The dashed red curve corresponds to the asymptotic linear behavior when we consider ϕ_r constant.

4.4/ INFLUENCE OF ANGLE OF INCIDENCE

A closer look at the equation 4.1, shows that there is no explicit relation between λ_{TEM} and the angle of incidence θ . Nonetheless, one can intuitively suspect a relation between this angle and the phase term ϕ_r . In order to point out this effect, we have performed extensive numerical simulations (see Fig. 4.9(a)) corresponding to a tilt angle $\alpha = 35^\circ$ and an angle of incidence that varies from -45° to 45° . The results show that the spectral position and the maximum value (100%) of the TEM -based transmission peak are independent of the angle of incidence. Only the quality factor (peak sharpness) is affected and it is maximum at normal incidence. Nevertheless, the TEM peak exhibits a perfect symmetry with respect to the normal incidence ($T(-\theta) = T(\theta)$), as shown in figure 4.9(b), where two spectra corresponding to $\theta = \pm 40^\circ$ are plotted. This property is a consequence of the energy balance and the reciprocity theorem as analytically demonstrated in the appendix (see paragraphs 1 and 3 of the appendix B). The symmetry of the spectra with respect to the angle of incidence (that appears for $\lambda > \lambda_{Rayleigh}$ corresponding to the subwavelength regime) can be understood intuitively by the fact that the dimensions aperture are sub-wavelength details of the structure, and therefore their properties cannot be detected in the far-field. On the contrary, when $\lambda < \lambda_{Rayleigh}$ the transmission spectra do not exhibit any symmetry. In this spectral range, propagating diffracted orders exist and their efficiencies depend on the tilt angle. Consequently, the diffracted zero order transmission changes with respect to the energy carried by these homogeneous orders. The obtained symmetry breaking, due to energy loss in the propagated diffraction orders,

4.4. INFLUENCE OF ANGLE OF INCIDENCE

is clearly illustrated in figure 4.9(b) where the diffracted zero order is more efficient when the angle between the incident light and the aperture axis (tilt direction) is small (blue curve of figure 4.9(b)) compared to the opposite incident angle case (red curve of figure 4.9(b)). Let us notice that the property of symmetry with respect to the angle of incidence is valid for any resonance of the transmission that occurs beyond the Rayleigh anomaly. This is clearly illustrated in the same figure 4.9(a) where the two TE_{11} -based transmission peaks exhibit the same symmetry properties with respect to the normal incident axis ($\theta = 0^\circ$) and also reach 100% transmission efficiency independently of the angle of incidence. Nevertheless, for large values of θ ($\gtrsim 20^\circ$), the Rayleigh anomaly approaches the TE_{11} -based transmission peaks and a coupling between the two resonances occur resulting in a modification of the transmission properties.

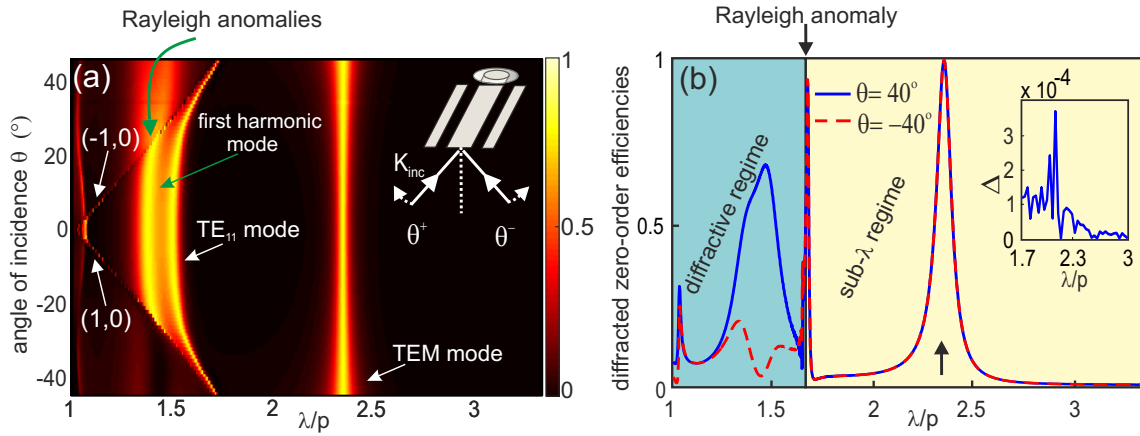


Figure 4.9: (a) Calculated transmission spectra in color level versus the angle of incidence. Inset of (a) presents the illumination direction with respect to the tilt angle. Two Rayleigh anomalies can be seen in the figure and are indicated by the value of the (m, l) corresponding to diffracted order (m along x and l along y axis). (b) two cross-sections made on (a) and illustrating the transmission spectra for two angles of incidence $\theta = 40^\circ$ in solid blue line and $\theta = -40^\circ$ in dashed red line. Note that the up- and down-arrows indicate the position of TEM -based transmission peak and the Rayleigh anomaly respectively whereas the value of the tilt angle is fixed to $\alpha = 35^\circ$. The inset of (b) shows the residual numerical signal ($\Delta = |T(\theta = 40^\circ) - T(\theta = -40^\circ)|$) corresponding to the difference between the two spectra only in the sub- λ regime.

All the results presented above correspond to a TM polarized incident plane wave where the electric field is parallel to the plane of incidence that is also parallel to the plane of aperture axis inclination ($\beta = 0^\circ$). For a TE polarization, the TEM mode is not excited whatever the value of the incidence angle (see figure 4.10). In addition, the two TE_{11} -based peaks are located at different spectral values from the TM case. This discrepancy is attributed to the asymmetry of the annular apertures (i.e the xOy plane) where aperture becomes elliptical with major axis along Ox direction. In order to point out the influence of

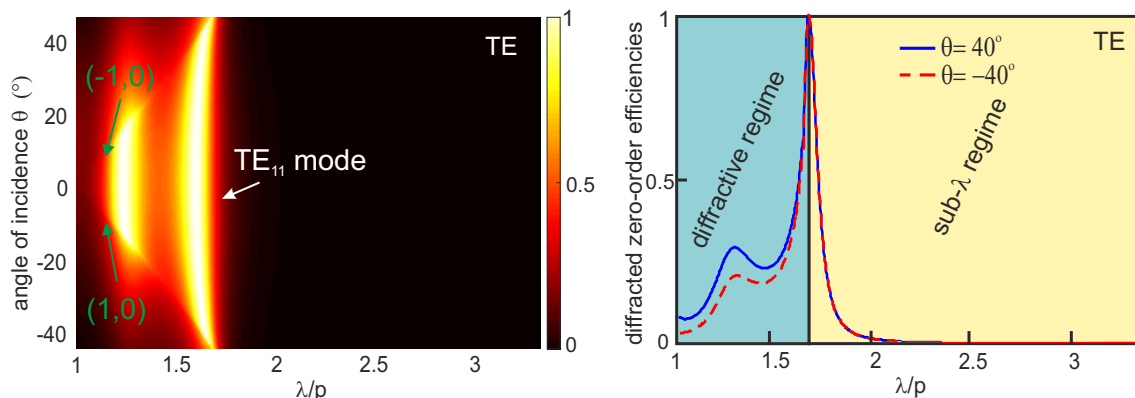


Figure 4.10: (a) Calculated transmission spectra in the case of TE polarization in color level versus the angle of incidence. Two Rayleigh anomalies can be seen in the figure and are indicated by the value of the (m, l) corresponding to diffracted order (m along x and l along y axis). (b) two cross-sections made on (a) and illustrating the transmission spectra for two angles of incidence $\theta = 40^\circ$ in solid blue line and $\theta = -40^\circ$ in dashed red line. Note that the up- and down-arrows indicate the position of the Rayleigh anomaly respectively whereas the value of the tilt angle is fixed to $\alpha = 35^\circ$.

the angle of incidence in a general case (mismatch between the incidence and inclination planes), we rotate the plane of incidence by an angle $\phi = 35^\circ$ (see figure 4.6) and we carry out the results of transmission in both TE and TM polarizations that are plotted in figure 4.11. One can see that the symmetry properties with respect to the angle of incidence are conserved. Nevertheless, the transmission efficiencies change (85% in TM) and a TEM peak appears in TE polarization (15%). As discussed in appendix B, this results from the projection of the incident field on the direction of the eigenvector that yields a 100% transmission (at $\phi = 0^\circ$ the TM polarization is parallel to this eigenvector).

4.5/ INFLUENCE OF THE AZIMUTHAL ANGLE

As already mentioned, an important information can be shown from the transmission spectra of the SAAA structure: the central symmetry allowing transmission of 100% at the wavelength resonance that only depends on the tilt angle. This total transmission (100%) is obtained whatever the angle of incidence and the tilt angle. Unfortunately, the polarization of the incident wave is the only parameter that is involved in the value of the transmission efficiency through the value of the azimuthal angle ϕ . In the following, we address the properties of the TEM-based mode with respect to the variation of this angle. For this purpose, let us fix the angle of incidence to $\theta = 30^\circ$ and vary ϕ from 0° to 60° by 5° step. Let us recall the geometrical parameter of the SAAA that are the same

4.5. INFLUENCE OF THE AZIMUTHAL ANGLE

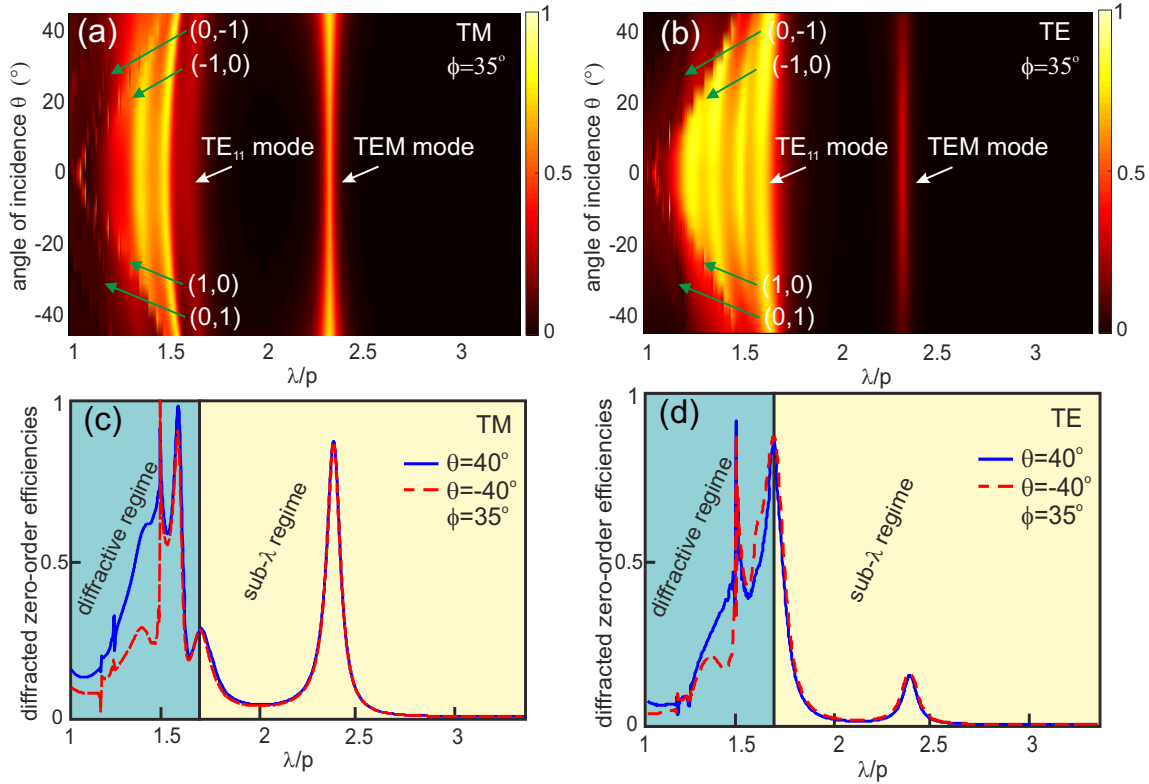


Figure 4.11: (Top) Calculated transmission spectra in color level in both TM (a) and TE (b) polarizations versus the angle of incidence. Two Rayleigh anomalies can be seen in the figure and are indicated by the value of the (m, l) corresponding to diffracted order (m along x and l along y axis). (Bottom) two cross-sections in both TM (c) and TE (d) polarizations made on (a) and (b) respectively, illustrating the transmission spectra for two angles of incidence $\theta = 40^\circ$ in solid blue line and $\theta = -40^\circ$ in dashed red line. Note that the up- and down-arrows indicate the position of the Rayleigh anomaly respectively whereas the value of the tilt angle is fixed to $\alpha = 35^\circ$ and for an arbitrary azimuthal angle $\phi = 35^\circ$.

as in the previous section: $R_i = p/6, R_o = p/3, h = 2p/3$ and $\alpha = 30^\circ$. The simulation results are presented in figure 4.12. On the other hand, the discontinuities shown in the transmission spectra of figure 4.12(a,b) correspond to Rayleigh anomalies which arise when a propagating diffracted wave likes evanescent. Once more, the figure 4.12(a,b) unambiguously shows that the sum of the transmission at the TEM -based peak appears 100% for both polarization states (TE, TM) (see figure 4.12(d)).

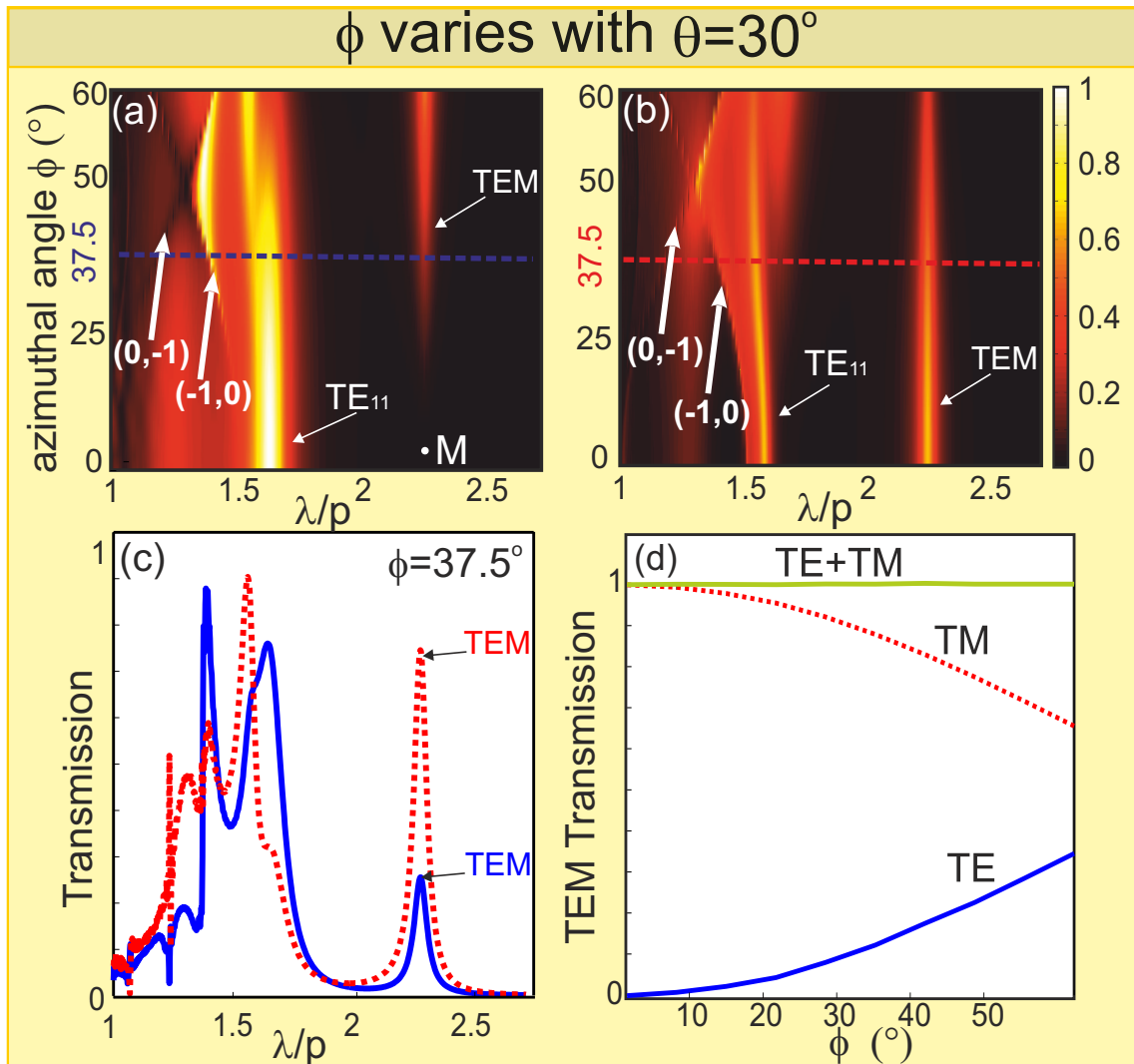


Figure 4.12: Transmission spectra for different azimuthal angles ϕ values in both TM (a) and TE (b) polarizations for an angle of incidence of $\theta = 30^\circ$. (c) Cross-sections made over (a) and (b) at $\phi = 37.5^\circ$. (d) Transmission efficiencies at λ_{TEM} of the two polarization states (TM in dashed red line and TE in solid blue line) and their sum (green horizontal line) as a function of the azimuthal angle ϕ .

4.6/ ANALYTIC TREATMENT

We address here an analytic treatment in order to reinforce our numerical results. The fact that for the structure under study, the sum of the transmittivities for TE and TM incident polarizations is equal to 100% at resonance whatever the angle of incidence, can be explained by analyzing the eigenvectors and eigenvalues of the $T_1^* T_1$ matrix, where T_1 is the scattering matrix of the structure and T_1^* is the conjugate transpose of T_1 . The details are presented in the Appendix B, which extends the demonstrations made in [154] and

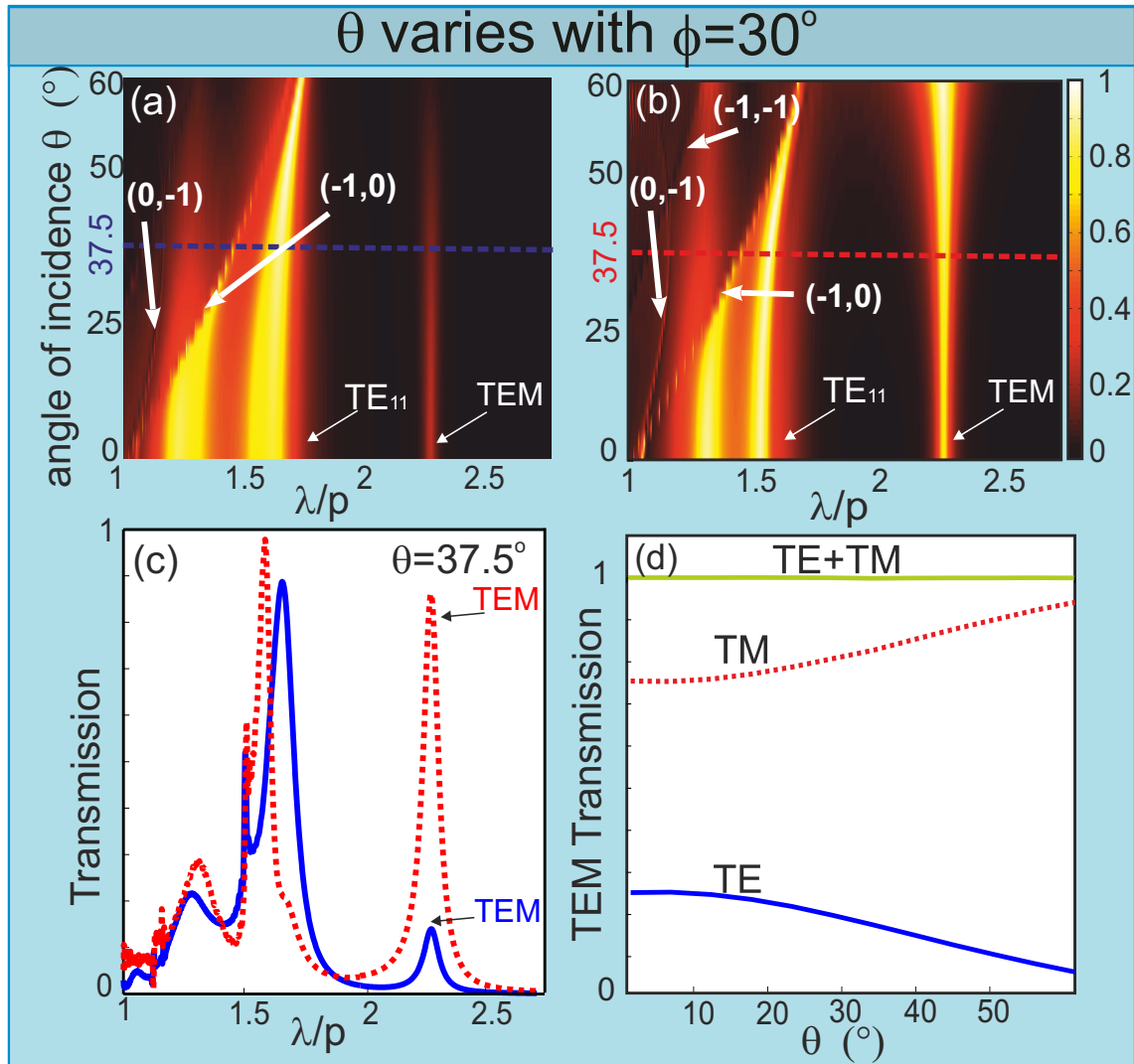


Figure 4.13: Transmission spectra for different angles of incidence in both TE (a) and TM (b) polarizations obtained for an arbitrary azimuthal angle $\phi = 30^\circ$. (c) Cross-sections made over (a) and (b) at $\theta = 37.5^\circ$. (d) Transmission efficiencies at λ_{TEM} of the two polarization states (TM in dashed red line and TE in solid blue line) and their sum (green horizontal line) as a function of the angle of incidence θ .

[155]. To sum-up, the two eigenvalues of the $T_1^* T_1$ matrix are real and positive and they are the limits of the range of variation of the transmittivity when the polarization of the incident plane wave takes all possible states, even non linear polarization states (see the Appendix B, first paragraph). The only necessary assumption is that the only propagative diffraction order is the zero order so the minimum wavelength value must be greater than the Rayleigh anomaly (sub-wavelength regime). The two eigenvectors, which are orthogonal to each other, correspond to the polarization of the incident wave that allow obtaining these limits of transmittivity. Hence, it appears that it is better to work with the eigenvalues and eigenvectors of the $T_1^* T_1$ matrix rather than with the transmittivities for TE

and TM incident polarizations, especially for structures leading to polarization conversion.

Furthermore, if the structure has a symmetry center, it is possible to show (see the Appendix B, paragraph 2-4) that one eigenvalue of the $T_1^*T_1$ matrix reaches 100% when one eigenmode is excited, provided that the materials are lossless.

4.6.1/ CENTRAL SYMMETRY OF THE TRANSMISSION IN SAAA.

In the case of the SAAA structure that presents a center of symmetry, we can say that there exists a polarization state (P_{max}) for which the transmission reaches 100%. Moreover, in our case, as we consider small apertures in a metallic plate, the orthogonal P_{min} polarization state leads to a negligible transmission, or eventually to a residual transmission due, for example, to the presence of another resonance at a different wavelength. In our case, it corresponds to the value of the transmission at point M of figure 4.12. The P_{max} polarization is clearly the TM polarization when $\beta = \phi = 0$ (see Fig. 4.13(b)), meaning a plane of incidence parallel to the aperture axis. In the general case of arbitrary incident polarization, because of the fact that the P_{max} and P_{min} polarization are orthogonal to each other, the sum of the transmittivities for TE and TM polarizations is equal to the sum of the eigenvalues of the $T_1^*T_1$ matrix, hence is close to 100%. This property is numerically verified through the results presented in Fig. 4.12 and 4.13 where different illumination configurations are considered by varying both the angle of incidence θ and the azimuthal one ϕ assuming $\beta = 0^\circ$. For each couple (θ, ϕ) , the two polarization states (TE, TM) are studied and we found that the sum of the transmission at the TEM -based peak is equal to 100% whatever the couple (θ, ϕ) is.

4.6.2/ TRANSMISSION SPECTRA OF AN ARBITRARY SAAA.

Let us now consider an arbitrary configuration where ϕ and β are simultaneously nonzero and different from each other. Consequently, we have fixed the geometrical and illumination parameters to : $R_i = p/6$, $R_o = p/3$, $h = 2p/3$, $\alpha = 30^\circ$, $\phi = 65^\circ$, $\beta = 25^\circ$ and $\theta = -35^\circ$. Fig. 4.14(a) presents the numerical transmission spectra where the dashed red line and the solid blue one correspond to the TE and TM polarization states respectively. Once again, the sum of the transmission at λ_{TEM} is equal to 1. The two eigenvalues of the $T_1^*T_1$ matrix are plotted in Fig. 4.14(b) where the solid green line corresponds to the polarization state P_{max} while the dashed magenta one represents the P_{min} state. As expected, perfect transmission is obtained at λ_{TEM} for the P_{max} polarization while an al-

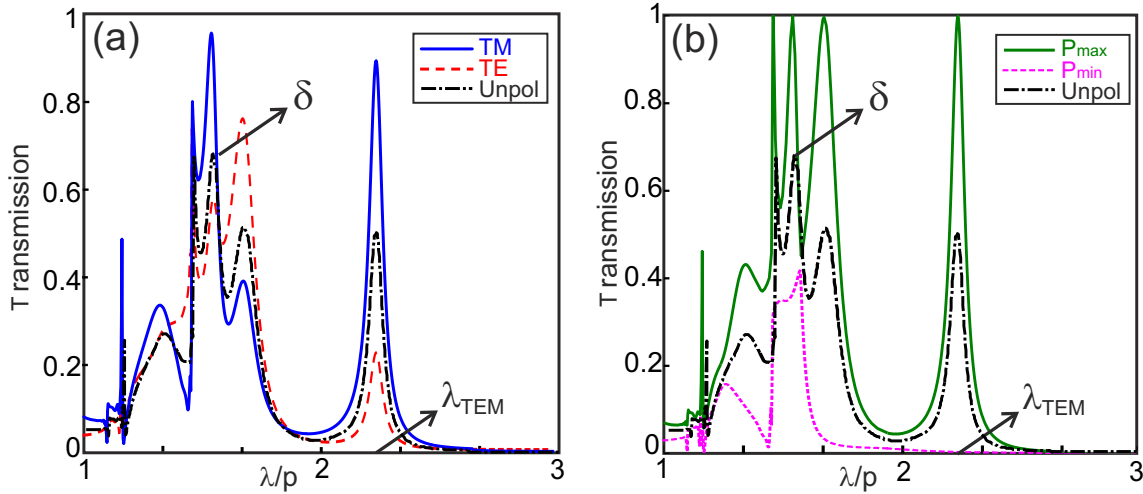


Figure 4.14: Transmission spectra of an arbitrary SAAA structure where $\beta = 25^\circ$, $R_o = p/3$, $R_i = p/6$, $h = 2p/3$ illuminated by a linearly polarized plane wave with $\phi = 65^\circ$ and $\theta = -35^\circ$. (a) The solid blue line corresponds to the case of a TM polarization while the dashed red one fits the case of a TE polarization. The dotted black line presents the transmission of an unpolarized incident beam. (b) Transmission spectra for the two polarization states (P_{max} , P_{min} that correspond to the two eigenvalues of the matrix $T_1^* T_1$). Note that the polarization states P_{max} and P_{min} vary with the wavelength. The dotted black line is the same as in (a) because it equals to $(P_{max} + P_{min})/2 = (TE + TM)/2$.

most zero transmission (2.6% only) occurs for the orthogonal polarization P_{min} . Note that, for the P_{max} polarization, other transmission maxima (up to 100%) arise corresponding to additional transmission resonances (especially due to the excitation of the TE_{11} guided mode at two different wavelength values corresponding to Fabry-Perot harmonics). It is important to note that the eigenvectors corresponding to the eigenvalues plotted in Fig. 4.14(b) generally vary with the wavelength, hence, the polarization state allowing a 100% transmittivity may not be the same when the TEM and the TE_{11} modes are excited. From this study, it appears that when one eigenmode is excited, the transmission efficiency of an unpolarized incident beam at the resonance wavelength is, at least, equal to 50%. This is confirmed by the plot of the transmittivity for an unpolarized wave in Fig. 4.14. Another conclusion is that a necessary condition to obtain a polarization independent transmittivity at resonance is to excite two eigenmodes.

4.6.3/ GIANT ENERGY DEVIATION

Finally, let us emphasize that in the sub-wavelength regime, at λ_{TEM} and for the polarization state P_{max} , the incident energy is totally routed through the apertures for every value of the tilt angle. As an example, we consider a SAAA structure with $\alpha = 35^\circ$ illuminated by

a plane wave propagating at $\theta = \pm 75^\circ$. The calculated transmission spectra for the P_{max} polarization state are presented in Fig. 4.15(a). A TEM -based transmission peak occurs at $\lambda_{TEM} = 2.3p$ whatever the sign of θ . In order to visualize the energy propagation in the vicinity of the SAAA, the energy flow (Poynting vector) is also calculated and presented in a vertical plane containing the axis of the apertures. One can clearly see in Fig. 4.15(b) and 4.15(c) the giant bending of light that occurs over a distance as small as $\lambda/5$ (see the direction change of the white arrows at the bottom of the structure). In the vicinity of the structure, the light energy follows a serpentine path with laminar flow (total transmission) through the nanostructured metallic film after suffering a total deviation of 220° over a distance smaller than the wavelength.

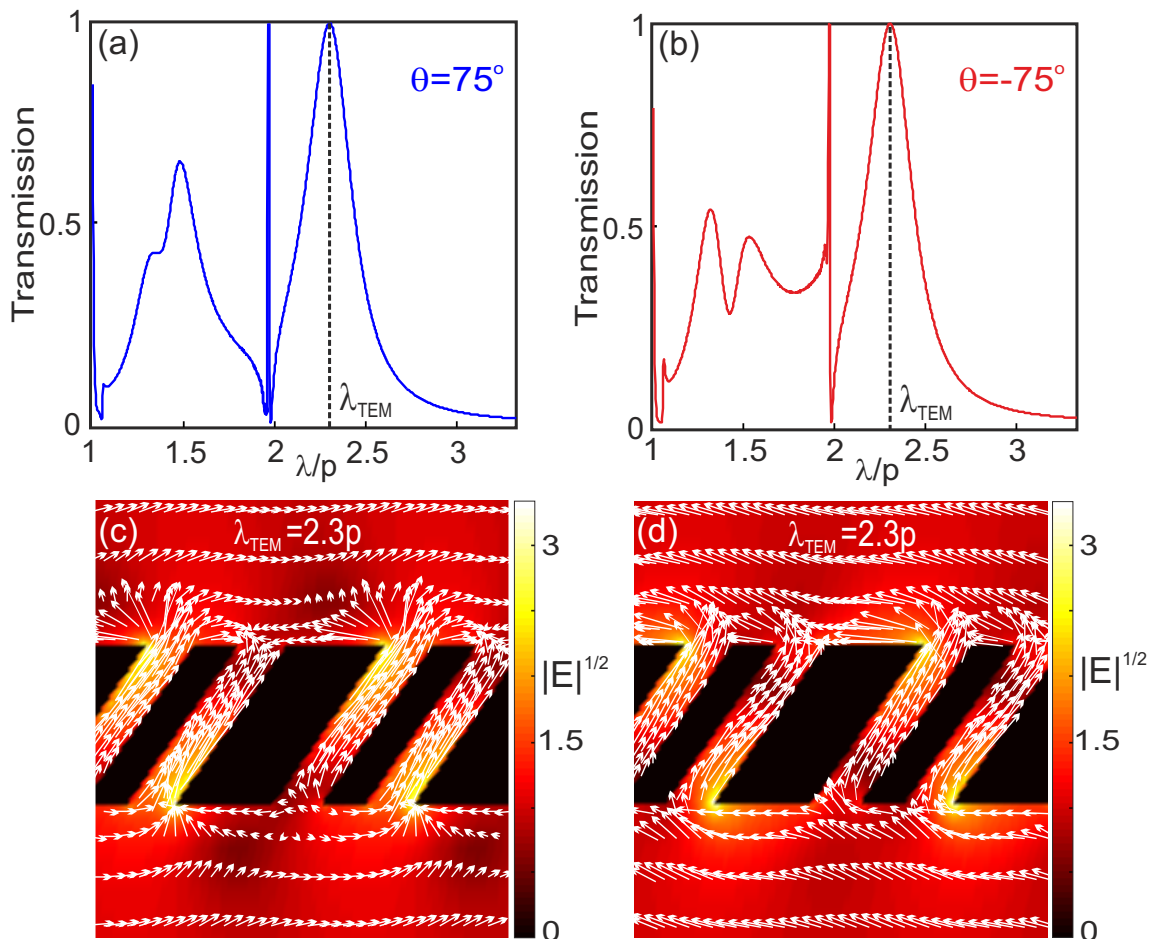


Figure 4.15: Transmission spectra for an angle of incidence $\theta = 75^\circ$ in (a) and $\theta = -75^\circ$ in (b) for the same SAAA structure of Fig. 4.7. (c) Square root of the electric field amplitude distributions (in color map) around the nano-structured metallic film in a vertical plane containing the aperture axis for an illumination at $\theta = 75^\circ$. White arrows correspond the tangential Poynting vector. (d) Same as (c) for $\theta = -75^\circ$.

4.7/ CONCLUSION

In this chapter, we have recalled a brief overview of the characterization and fabrication as well as the numerical study of the influence of the inner and outer radius in both PEC and silver SAAA on the transmission spectra of the SAAA structure. In this review, the simulated SAAA has also been qualitatively validated through the investigation of the zero-order transmission for both recorded experimental transmission and the correspondent theoretical simulations. The comparison between the measurement and simulation results agreed very well.

In addition, we have studied the fundamental aspect of the enhanced transmission mechanism through the SAAA structure on the basis of both numerical and analytical calculations. we have first carried out a numerical comparison between the transmission of an AAA and SAAA structures having the same film thickness. This comparison have revealed that the TEM -based transmission peaks appears and reaches 100% for both structures although they have red-shifted on its spectral position but SAAA spectra is located at $\lambda_{TEM}(SAAA) > \lambda_{TEM}(AAA)$. As an additional result, we presented some properties of this structure that demonstrate a high potential for applications in various fields such as spectral filtering regardless of the illumination direction. The giant deviation of the energy flux over small distance presented in Fig. 4.15(c) and (d), brings a supplementary and comprehensive physical insight about the guided mode-based enhanced transmission paradigm without the need to resort to surface plasmons or other surface waves.

GENERAL CONCLUSION

We have improved an existing FDTD code by integrating the TF/SF technique. This method allows calculating the pure scattered field and the absorbed one. After applying this technique on a sphere particle, the result showed a mismatch with those from analytical Mie solutions. We took advantage of a method that was already implemented in the context of the FDTD algorithm by other authors, the CPT (Contour Path Technique). The latter have also adapted in our code to more accurately describe the curved surface of a structure keeping parallelepiped mesh by resolving Maxwell equations expressed in their integral forms at specific cells of the grid. We have seen that the numerical result of a single metal nanosphere has a high accuracy and exhibits a very good agreement with the Mie solution than those resulted from classic FDTD (i.e. FDTD code without CPT). The supported TF/SF and CPT- FDTD techniques which are effective for a wide range of problems have employed to study the optical responses of NAs as one of the important applications in optical domain. We have emphasized that the influence of shape can control the optical antennas properties such as the scattering efficiency and the resonance wavelength. Therefore, a comparison between two different designs of optical NA (BA and DA) has been performed. The numerical results have showed that at plasmon resonance, the diabolo design exhibits a very large amount of scattering compared to bowtie one. The interesting obtained results are thanks to a highly localized electromagnetic field in the vicinity of the DA (both center and corners). Due to the interesting resonance properties of the DA, a systematic study is performed including the influences of metal nature, the host medium and geometrical parameters (length, gap and thickness) affecting on tunability of the resonance frequency and hence controlling its the performances of optical antennas. We have showed that the magnitude of the scattering efficiency is strongly influenced by the factors (parameters) studied above. The obtained results explain that the excitation of LSPR plays a vital role by increasing the effective section up to several times the physical cross section of the nanostructure. This feature can be employed to enhance the interaction of any object located in their proximity with electromagnetic wave.

The TF/SF technique adopted in FDTD algorithm is applicable to model any NPs and detect their efficiencies to make them suitable for various applications. Future simulations study may address another nanoform which can be useful in evaluating the optical responses for applications where the strong scattering or/and absorption efficiencies are desired.

In the context of plasmonic wave guide, the optical properties of the latter have been theoretically studied in the next chapter. Parametric simulations have been conducted to obtain the most convenient parameters that allow an efficient transmission of light through AAA structure. The simulation results were useful to facilitate and optimize the AAA fabrication process that were performed in the context of another thesis performed in our laboratory. The ET assisted by a *TEM* mode, which is a pure plasmonic guided mode of a metallic coaxial waveguide, in the optical regime is observed through exciting this peculiar mode inside each annular aperture under oblique incident TM polarized light. Nevertheless, the magnitude of the *TEM* amplitude remains low due to the metal absorption that specifically occurs in the visible range. In fact, only high efficient *TEM*-based ET can be achieved in the domain of terahertz waves or microwaves where metal absorption is negligible.

In order to get more interesting properties of AAA structure, we have taken the advantage of SAAA structure that was previously proposed to study the fundamental aspect of the enhanced transmission mechanism on the basis of both numerical and analytical calculations. We have performed a comparison between the AAA and SAAA structures in the case of PEC. It has been found that the spectral position of the *TEM* mode of SAAA is significantly red shifted compared to AAA structure. We have numerically shown that the light is totally transmitted through the structure independently of the value of tilted angle but at different values of wavelengths. The numerical simulations have presented another feature including that the peak of *TEM* guided mode at the maximum value (100%) of the transmission is independent of the angle of incidence θ and its quality factor increases when the θ becomes close to zero. The property of the transmission spectra with respect to the angle of incidence is analytically demonstrated through the concept of energy balance and the reciprocity theorem. Consequently, the property of symmetry respect to θ can be valid for any resonance of the transmission. Another surprising property is observed when the planes of incidence are not along the direction of periodicity of the structure. Similarly, it has numerically and analytically found that the sum of the transmission at the *TEM*-based peak is equal to 100% whatever the angle of incidence and the azimuthal one. This means that, for incoherent illumination (sun for instance), the transmission is equal to 50% whatever the light source condition. In addition, we have

emphasized that in the subwavelength regime at λ_{TEM} and for the transmission maxima, the incident energy is totally routed through the apertures of SAAA for every value of tilt angle. This is illustrated by visualizing the energy propagation in the vicinity of the SAAA. The giant bending of light is clearly observed over a distance as small as $\lambda/5$ and it follows a serpentine path with laminar flow with deviation of 220° per wavelength.

This structure supports some properties that demonstrate a high potential for applications in various fields such as spectral filtering regardless of the illumination direction. The next step should address the potential enhancement of the transmission of unpolarized beams (more than 50%) by spectrally approaching two different resonances (here the TEM and the TE_{11} ones) without causing destructive coupling through a degeneracy breaking. This may require an accurate optimization of the parameters of the structure or more complex structure geometries, as it was done in the case of all dielectric sub-wavelength periodic structures presenting a resonance peak due to the excitation of a leaky guided mode (guided mode resonance grating) [156, 157] .

BIBLIOGRAPHY

- [1] Michael Faraday. The bakerian lecture: Experimental relations of gold (and other metals) to light. *Philosophical Transactions of the Royal Society of London*, 147:145–181, 1857.
- [2] L. Rayleigh. *Philosophical Magazine*, 47:375, 1899.
- [3] Gustav Mie. Beiträge zur optik trüber medien, speziell kolloidaler metallösungen. *Annalen der Physik*, 330(3):377–445, 1908.
- [4] G.C. Papavassiliou. Optical properties of small inorganic and organic metal particles. *Progress in Solid State Chemistry*, 12(34):185 – 271, 1979.
- [5] D. R. Bohren, C. F.; Huffman. *Absorption and Scattering of Light by Small Particles*. Wiley Interscience: New York, 1983.
- [6] R. Gans. Colour of ellipsoid. *Ann. Phys. (Leipzig)*, 37:881, 1912.
- [7] M. Fleischmann, P.J. Hendra, and A.J. McQuillan. Raman spectra of pyridine adsorbed at a silver electrode. *Chemical Physics Letters*, 26(2):163 – 166, 1974.
- [8] David L. Jeanmaire and Richard P. Van Duyne. Surface raman spectroelectrochemistry. *Journal of Electroanalytical Chemistry and Interfacial Electrochemistry*, 84(1):1 – 20, 1977.
- [9] M. Grant Albrecht and J. Alan Creighton. Anomalously intense raman spectra of pyridine at a silver electrode. *Journal of the American Chemical Society*, 99(15):5215–5217, 1977.
- [10] A. Taflove and S. C. Hagness. *Computational Electrodynamics : The Finite Difference Time Domain Method*. Artech House, Norwood, MA, second edition, 2005.
- [11] M. Vollmer U. Kreibig. *Optical properties of metal clusters*. Springer, 1995.
- [12] K. Lance Kelly, Eduardo Coronado, Lin Lin Zhao, and George C. Schatz. The optical properties of metal nanoparticles: the influence of size, shape, and dielectric environment. *The Journal of Physical Chemistry B*, 107(3):668–677, 2003.

- [13] P. Bharadwaj, B. Deutsch, and N. Lukas. Optical antennas. *Adv. Opt. Photon.*, 1(3):438–483, Nov 2009.
- [14] Vincenzo Giannini, Antonio I. Fernández-Domínguez, Susannah C. Heck, and Stefan A. Maier. Plasmonic nanoantennas: Fundamentals and their use in controlling the radiative properties of nanoemitters. *Chemical Reviews*, 111(6):3888–3912, 2011. PMID: 21434605.
- [15] Antoine Moreau, Cristian Ciraci, Jack J. Mock, Ryan T. Hill, Qiang Wang, Benjamin J. Wiley, Ashutosh Chilkoti, and David R. Smith. Controlled-reflectance surfaces with film-coupled colloidal nanoantennas. *Nature*, 492(7427):86–89, December 2012.
- [16] Mark W. Knight, Lifei Liu, Yumin Wang, Lisa Brown, Shaunak Mukherjee, Nicholas S. King, Henry O. Everitt, Peter Nordlander, and Naomi J. Halas. Aluminum plasmonic nanoantennas. *Nano Letters*, 12(11):6000–6004, 2012. PMID: 23072330.
- [17] Martin Husnik, Stefan Linden, Richard Diehl, Jens Niegemann, Kurt Busch, and Martin Wegener. Quantitative experimental determination of scattering and absorption cross-section spectra of individual optical metallic nanoantennas. *Phys. Rev. Lett.*, 109:233902, Dec 2012.
- [18] T. Grosjean, M. Mivelle, F. I. Baida, G. W. Burr, and U. C. Fischer. Diabolo nanoantenna for enhancing and confining the magnetic optical field. *Nano Letters*, 11(3):1009–1013, 2011. PMID: 21319837.
- [19] C. J. Powell and J. B. Swan. Effect of oxidation on the characteristic loss spectra of aluminum and magnesium. *Phys. Rev.*, 118:640–643, May 1960.
- [20] R. H. Ritchie. Plasma losses by fast electrons in thin films. *Phys. Rev.*, 106:874–881, Jun 1957.
- [21] R W Wood. On a remarkable case of uneven distribution of light in a diffraction grating spectrum. *Proceedings of the Physical Society of London*, 18(1):269, 1902.
- [22] Lord Rayleigh. On the dynamical theory of gratings. *Proceedings of the Royal Society of London A: Mathematical, Physical and Engineering Sciences*, 79(532):399–416, 1907.
- [23] U. Fano. The theory of anomalous diffraction gratings and of quasi-stationary waves on metallic surfaces (sommerfeld’s waves). *J. Opt. Soc. Am.*, 31(3):213–222, Mar 1941.

- [24] Andreas Otto. Excitation of nonradiative surface plasma waves in silver by the method of frustrated total reflection. *Zeitschrift für Physik*, 216(4):398–410, 1968.
- [25] E. Kretschmann and H. Raether. Radiative decay of nonradiative surface plasmons excited by light. *Zeitschrift für Naturforschung A*, 23, 1968.
- [26] T. W. Ebbesen, H. J. Lezec, H. F. Ghaemi, T. Thio, and P. A. Wolff. Extraordinary optical transmission through sub-wavelength hole arrays. *Nature*, 391:667–669, 1998.
- [27] F. I. Baida, A. Belkhir, D. Van Labeke, and O. Lamrous. Subwavelength metallic coaxial waveguides in the optical range: Role of the plasmonic modes. *Phys. Rev. B*, 74:205419, 2006.
- [28] Michael I. Haftel, Carl Schlockermann, and G. Blumberg. Enhanced transmission with coaxial nanoapertures: Role of cylindrical surface plasmons. *Phys. Rev. B*, 74:235405, Dec 2006.
- [29] F. Baida and J. Salvi. *Reviews in Plasmonics 2010*. Springer, New York, 2011.
- [30] F. I. Baida and D. Van Labeke. Light transmission by subwavelength annular aperture arrays in metallic films. *Opt. Commun.*, 209:17–22, 2002.
- [31] F. I. Baida and D. Van Labeke. Three-dimensional structures for enhanced transmission through a metallic film: Annular aperture arrays. *Phys. Rev. B*, 67:155314, 2003.
- [32] Rodríguez-Oliveros Rogelio, Paniagua-Domínguez Ramón, Sánchez-Gil José A., and Macías Demetrio. Plasmon spectroscopy: Theoretical and numerical calculations, and optimization techniques. *Nanospectroscopy*, 1, 2015.
- [33] M. Futamata, Y. Maruyama, and M. Ishikawa. Local electric field and scattering cross section of ag nanoparticles under surface plasmon resonance by finite difference time domain method. *The Journal of Physical Chemistry B*, 107(31):7607–7617, 2003.
- [34] Chris Oubre and Peter Nordlander. Optical properties of metallodielectric nanostructures calculated using the finite difference time domain method. *The Journal of Physical Chemistry B*, 108(46):17740–17747, 2004.
- [35] George C. Schatz Richard P. Van Duyne Benjamin J. Wiley Leif J. Sherry, Shih-Hui Chang and Younan Xia. Localized surface plasmon resonance spectroscopy of single silver nanocubes. *Nano Letters*, 5(10):2034–2038, 2005. PMID: 16218733.

- [36] Viktor Myroshnychenko, Jessica Rodriguez-Fernandez, Isabel Pastoriza-Santos, Alison M. Funston, Carolina Novo, Paul Mulvaney, Luis M. Liz-Marzan, and F. Javier Garcia de Abajo. Modelling the optical response of gold nanoparticles. *Chem. Soc. Rev.*, 37:1792–1805, 2008.
- [37] Hitoshi Kuwata, Hiroharu Tamaru, Kunio Esumi, and Kenjiro Miyano. Resonant light scattering from metal nanoparticles: Practical analysis beyond rayleigh approximation. *Applied Physics Letters*, 83(22):4625–4627, 2003.
- [38] Encai Hao and George C. Schatz. Electromagnetic fields around silver nanoparticles and dimers. *The Journal of Chemical Physics*, 120(1):357–366, 2004.
- [39] I. H. El-Sayed, X. Huang, and M. A. El-Sayed. Surface plasmon resonance scattering and absorption of anti-egfr antibody conjugated gold nanoparticles in cancer diagnostics: applications in oral cancer. *Nano Letters*, 5(5):829–834, 2005. PMID: 15884879.
- [40] K. Prashant, K. S. L. Jain, I. H. El-Sayed, and M. A. El-Sayed. Calculated absorption and scattering properties of gold nanoparticles of different size, shape, and composition: Applications in biological imaging and biomedicine. *The Journal of Physical Chemistry B*, 110(14):7238–7248, 2006. PMID: 16599493.
- [41] Xiaohua Huang, Ivan H. El-Sayed, Wei Qian, , and Mostafa A. El-Sayed*. Cancer cell imaging and photothermal therapy in the near-infrared region by using gold nanorods. *Journal of the American Chemical Society*, 128(6):2115–2120, 2006. PMID: 16464114.
- [42] Xiaohua Huang and Mostafa A. El-Sayed. Gold nanoparticles: Optical properties and implementations in cancer diagnosis and photothermal therapy. *Journal of Advanced Research*, 1(1):13–28, 2010.
- [43] Sameh Kessentini and Dominique Barchiesi. Quantitative comparison of optimized nanorods, nanoshells and hollow nanospheres for photothermal therapy. *Biomed. Opt. Express*, 3(3):590–604, Mar 2012.
- [44] Emilie Ringe, Mark R. Langille, Kwonnam Sohn, Jian Zhang, Jiaying Huang, Chad A. Mirkin, Richard P. Van Duyne, and Laurence D. Marks. Plasmon length: A universal parameter to describe size effects in gold nanoparticles. *The Journal of Physical Chemistry Letters*, 3(11):1479–1483, 2012. PMID: 26285624.
- [45] G.W. Ford and W.H. Weber. Electromagnetic interactions of molecules with metal surfaces. *Physics Reports*, 113(4):195 – 287, 1984.

- [46] T. Klar, M. Perner, S. Grosse, G. von Plessen, W. Spirkel, and J. Feldmann. Surface-plasmon resonances in single metallic nanoparticles. *Phys. Rev. Lett.*, 80:4249–4252, May 1998.
- [47] W. L. Barnes. Fluorescence near interfaces: The role of photonic mode density. *Journal of Modern Optics*, 45(4):661–699, 1998.
- [48] J. J. Mock, M. Barbic, D. R. Smith, D. A. Schultz, and S. Schultz. Shape effects in plasmon resonance of individual colloidal silver nanoparticles. *The Journal of Chemical Physics*, 116(15):6755–6759, 2002.
- [49] Stefan A. Maier and Harry A. Atwater. Plasmonics: Localization and guiding of electromagnetic energy in metal/dielectric structures. *Journal of Applied Physics*, 98(1), 2005.
- [50] P. Mhlschlegel, H.-J. Eisler, O. J. F. Martin, B. Hecht, and D. W. Pohl. Resonant optical antennas. *Science*, 308(5728):1607–1609, 2005.
- [51] A. V. Akimov, A. Mukherjee, C. L. Yu, D. E. Chang, A. S. Zibrov, P. R. Hemmer, H. Park, and M. D. Lukin. Generation of single optical plasmons in metallic nanowires coupled to quantum dots. *Nature*, 450(7168):402–406, November 2007.
- [52] S. Maier. *Plasmonics: Fundamentals and Applications*. Springer Verlag, 2007.
- [53] Lukas Novotny and Niek van Hulst. Antennas for light. *Nat Photon*, 5(2):83–90, February 2011.
- [54] Shuming Nie and Steven R. Emory. Probing single molecules and single nanoparticles by surface-enhanced raman scattering. *Science*, 275(5303):1102–1106, 1997.
- [55] Jon P. Camden, Jon A. Dieringer, Yingmin Wang, David J. Masiello, Lawrence D. Marks, George C. Schatz, and Richard P. Van Duyne. Probing the structure of single-molecule surface-enhanced raman scattering hot spots. *Journal of the American Chemical Society*, 130(38):12616–12617, 2008. PMID: 18761451.
- [56] Eric C. Le Ru and Pablo G. Etchegoin. Preface. In Eric C. Le Ru and Pablo G. Etchegoin, editors, *Principles of Surface-Enhanced Raman Spectroscopy*, pages xvii – xix. Elsevier, Amsterdam, 2009.
- [57] Anika Kinkhabwala, Zongfu Yu, Shanhui Fan, Yuri Avlasevich, Klaus Mullen, and Moerner W. E. Large single-molecule fluorescence enhancements produced by a bowtie nanoantenna. *Nat Photon*, 3(11):654–657, November 2009.

- [58] Jon A. Schuller, Edward S. Barnard, Wenshan Cai, Young Chul Jun, Justin S. White, and Mark L. Brongersma. Plasmonics for extreme light concentration and manipulation. *Nat Mater*, 9(3):193–204, March 2010.
- [59] Niels Verellen, Pol Van Dorpe, Chengjun Huang, Kristof Lodewijks, Guy A. E. Vandenbosch, Liesbet Lagae, and Victor V. Moshchalkov. Plasmon line shaping using nanocrosses for high sensitivity localized surface plasmon resonance sensing. *Nano Letters*, 11(2):391–397, 2011. PMID: 21265553.
- [60] K. B. Crozier, A. Sundaramurthy, G. S. Kino, and C. F. Quate. Optical antennas: Resonators for local field enhancement. *Journal of Applied Physics*, 94(7):4632–4642, 2003.
- [61] David P. Fromm, Arvind Sundaramurthy, P. James Schuck, Gordon Kino, , and W. E. Moerner*. Gap-dependent optical coupling of single bowtie nanoantennas resonant in the visible. *Nano Letters*, 4(5):957–961, 2004.
- [62] J. N. Farahani, D. W. Pohl, H.-J. Eisler, and B. Hecht. Single quantum dot coupled to a scanning optical antenna: A tunable superemitter. *Phys. Rev. Lett.*, 95:017402, Jun 2005.
- [63] P. J. Schuck, D. P. Fromm, A. Sundaramurthy, G. S. Kino, and W. E. Moerner. Improving the mismatch between light and nanoscale objects with gold bowtie nanoantennas. *Phys. Rev. Lett.*, 94:017402, Jan 2005.
- [64] Gaëtan Lévêque and Olivier J.F. Martin. Tunable composite nanoparticle for plasmonics. *Opt. Lett.*, 31(18):2750–2752, Sep 2006.
- [65] K. H. Su, Q. H. Wei, and X. Zhang. Tunable and augmented plasmon resonances of Au nanodisks. *Applied Physics Letters*, 88(6), 2006.
- [66] Ertugrul Cubukcu, Eric A. Kort, Kenneth B. Crozier, and Federico Capasso. Plasmonic laser antenna. *Applied Physics Letters*, 89(9), 2006.
- [67] Jingjing Li, Alessandro Salandrino, and Nader Engheta. Shaping light beams in the nanometer scale: A yagi-uda nanoantenna in the optical domain. *Phys. Rev. B*, 76:245403, Dec 2007.
- [68] O. L. Muskens, V. Giannini, J. A. Sánchez-Gil, and J. Gómez Rivas. Optical scattering resonances of single and coupled dimer plasmonic nanoantennas. *Opt. Express*, 15(26):17736–17746, Dec 2007.

- [69] Reuben M. Bakker, Alexandra Boltasseva, Zhengtong Liu, Rasmus H. Pedersen, Samuel Gresillon, Alexander V. Kildishev, Vladimir P. Drachev, and Vladimir M. Shalaev. Near-field excitation of nanoantenna resonance. *Opt. Express*, 15(21):13682–13688, Oct 2007.
- [70] Holger Fischer and Olivier J. F. Martin. Engineering the optical response of plasmonic nanoantennas. *Opt. Express*, 16(12):9144–9154, Jun 2008.
- [71] Andrea Alu and Nader Engheta. Tuning the scattering response of optical nanoantennas with nanocircuit loads. *Nat Photon*, 2(5):307–310, May 2008.
- [72] Merle Jorg, Matthias Kahl, Annika Zuschlag, Alexander Sell, Andreas Halm, Johannes Boneberg, Paul Leiderer, Alfred Leitenstorfer, and Rudolf Bratschitsch. Nanomechanical control of an optical antenna. *Nat Photon*, 2(4):230–233, April 2008.
- [73] Schnell M., Garcia-Etxarri A., Huber A. J., Crozier K., Aizpurua J., and Hillenbrand R. Controlling the near-field oscillations of loaded plasmonic nanoantennas. *Nat Photon*, 3(5):287–291, May 2009.
- [74] Petru Ghenuche, Sudhir Cherukulappurath, Tim H. Taminiau, Niek F. van Hulst, and Romain Quidant. Spectroscopic mode mapping of resonant plasmon nanoantennas. *Phys. Rev. Lett.*, 101:116805, Sep 2008.
- [75] Robert D. Grober, Robert J. Schoelkopf, and Daniel E. Prober. Optical antenna: Towards a unity efficiency near-field optical probe. *Applied Physics Letters*, 70(11):1354–1356, 1997.
- [76] Arvind Sundaramurthy, K. B. Crozier, G. S. Kino, D. P. Fromm, P. J. Schuck, and W. E. Moerner. Field enhancement and gap-dependent resonance in a system of two opposing tip-to-tip Au nanotriangles. *Phys. Rev. B*, 72:165409, Oct 2005.
- [77] Z. Zhang, A. Weber-Bargioni, S. W. Wu, S. Dhuey, S. Cabrini, and P. J. Schuck. Manipulating nanoscale light fields with the asymmetric bowtie nano-colorsorter. *Nano Letters*, 9(12):4505–4509, 2009. PMID: 19899744.
- [78] I. A. Ibrahim, M. Mivelle, T. Grosjean, J.-T. Allegre, G. W. Burr, and F. I. Baida. Bowtie-shaped nanoaperture: a modal study. *Opt. Lett.*, 35(14):2448–2450, Jul 2010.
- [79] Kaspar D. Ko, Anil Kumar, Kin Hung Fung, Raghu Ambekar, Gang Logan Liu, Nicholas X. Fang, and Jr. Kimani C. Toussaint. Nonlinear optical response from arrays of Au bowtie nanoantennas. *Nano Letters*, 11(1):61–65, 2011. PMID: 21105719.

- [80] W. Zhong, Y. Wang, R. He, and X. Zhou. Investigation of plasmonics resonance infrared bowtie metal antenna. *Applied Physics B*, 105(2):231–237, 2011.
- [81] David A. Rosen and Andrea R. Tao. Modeling the optical properties of bowtie antenna generated by self-assembled ag triangular nanoprisms. *ACS Applied Materials & Interfaces*, 6(6):4134–4142, 2014. PMID: 24533909.
- [82] E. Hutter and J. H. Fendler. Exploitation of localized surface plasmon resonance. *Advanced Materials*, 16(19):1685–1706, 2004.
- [83] Surbhi Lal, Stephan Link, and Naomi J. Halas. Nano-optics from sensing to waveguiding. *Nat Photon*, 1(11):641–648, November 2007.
- [84] Eric F. Y. Kou and Theodor Tamir. Incidence angles for optimized atr excitation of surface plasmons. *Appl. Opt.*, 27(19):4098–4103, Oct 1988.
- [85] P. B. Johnson and R. W. Christy. Optical constants of the noble metals. *Phys. Rev. B*, 6:4370–4379, Dec 1972.
- [86] K. Yee. Numerical solution in initially boundary value problems involving Maxwell's equations in isotropic media. *IEEE Trans. Antennas Propag.*, 14:302–307, 1966.
- [87] D.M. Sullivan. *Electromagnetic Simulation Using the FDTD Method*. Wiley, IEEE Press, New York, 2000.
- [88] V. Demir A. Elsherbeni. *The Finite Difference Time Domain Method for Electromagnetics: With MATLAB Simulations*. SciTech, Rayleigh, NC, 2009.
- [89] T. Su Y. Liu X. Yang W. Yu, R. Mittra. *Parallel Finite-Difference Time-Domain Method*. Artech House, Norwood, MA, 2006.
- [90] F.I. Baida, D. Van Labeke, G. Granet, A. Moreau, and A. Belkhir. Origin of the super-enhanced light transmission through a 2-d metallic annular aperture array: a study of photonic bands. *Applied Physics B*, 79(1):1–8, 2004.
- [91] F. I. Baida, D. Van Labeke, G. Granet, A. Moreau, and A. Belkhir. Origin of the super-enhanced light transmission through a 2-d metallic annular aperture array: a study of photonic bands. *Appl. Phys. B*, 79:1–8, 2004.
- [92] F. I. Baida, M. Boutria, R. Oussaid, and D. Van Labeke. Enhanced-transmission metamaterials as anisotropic plates. *Phys. Rev. B*, 84:035107, Jul 2011.
- [93] F. I. Baida, A. Belkhir, O. Arar, E. Barakat, J. Dahdah, C. Chemrouk, D. Van Labeke, C. Diebold, N. Perry, and M.-P. Bernal. Enhanced optical transmission by light coaxing: Mechanism of the {TEM}-mode excitation. *Micron*, 41:742–745, 2010.

- [94] F.I. Baida, D. Van Labeke, and Y. Pagani. Body-of-revolution {FDTD} simulations of improved tip performance for scanning near-field optical microscopes. *Optics Communications*, 225(46):241 – 252, 2003.
- [95] R. Courant, K. Friedrich, and H. Lewy. On the partial differential equation of mathematical physics. 1967.
- [96] J. G. CHARNEY, R. FJORTOFT, and J. von NEUMANN. Numerical integration of the barotropic vorticity equation. *Aquarterly Journal of Geophysics*, 2, 1950.
- [97] Jean-Pierre Berenger. A perfectly matched layer for the absorption of electromagnetic waves. *Journal of Computational Physics*, 114(2):185–200, 1994.
- [98] Matthew C. Beard and Charles A. Schmuttenmaer. Using the finite-difference time-domain pulse propagation method to simulate time-resolved thz experiments. *The Journal of Chemical Physics*, 114(7):2903–2909, 2001.
- [99] F I Baida and A Blekhir. Split field-fdtd method for oblique incidence study of periodic dispersive metallic structures. *Optics letter*, 34:2453–2455, 2009.
- [100] F. L. Teixeira, Weng Cho Chew, M. Straka, M. L. Oristaglio, and T. Wang. Finite-difference time-domain simulation of ground penetrating radar on dispersive, inhomogeneous, and conductive soils. *IEEE Transactions on Geoscience and Remote Sensing*, 36(6):1928–1937, Nov 1998.
- [101] Stephen K. Gray and Teobald Kupka. Propagation of light in metallic nanowire arrays: Finite-difference time-domain studies of silver cylinders. *Phys. Rev. B*, 68:045415, Jul 2003.
- [102] Alexandre Vial, Anne-Sophie Grimault, Demetrio Macías, Dominique Barchiesi, and Marc Lamy de la Chapelle. Improved analytical fit of gold dispersion: Application to the modeling of extinction spectra with a finite-difference time-domain method. *Phys. Rev. B*, 71:085416, Feb 2005.
- [103] Alexandre Vial and Thierry Laroche. Description of dispersion properties of metals by means of the critical points model and application to the study of resonant structures using the fdtd method. *Journal of Physics D: Applied Physics*, 40(22):7152, 2007.
- [104] M Hamidi, F I Baida, A Belkhir, and O Lamrous. Implementation of the critical points model in a sfm-fdtd code working in oblique incidence. *Journal of Physics D: Applied Physics*, 44(24):245101, 2011.
- [105] C. Kittel. *Physcs of solid state*. Dunod, 2002.

- [106] P. Drude. To the electron theory of metals. *Annals of Physics*, 306:566–613, 1900.
- [107] Alexandre Vial. Implementation of the critical points model in the recursive convolution method for modelling dispersive media with the finite-difference time domain method. *Journal of Optics A: Pure and Applied Optics*, 9(7):745, 2007.
- [108] E.D. Palik. *Handbook of optical constants of solids*. Academic Press, 1985.
- [109] E.D. Palik. *Handbook of optical constants of solids III*. Academic Press, 2009.
- [110] D.E. Merewether, R. Fisher, and F.W. Smith. On implementing a numeric huygen’s source scheme in a finite difference program to illuminate scattering bodies. *Nuclear Science, IEEE Transactions on*, 27(6):1829–1833, Dec 1980.
- [111] Robert Lee Le Wei Li Neelakantam V. Venkatarayalu, Yeow Beng Gan. Application of hybrid fctd-fdtd method in the modeling and analysis of antennas. *IEEE Transactions on Antennas and Propagation*, 56:3068–3072, 2008.
- [112] Nectaria Diamanti and Antonios Giannopoulos. Implementation of adi-fdtd subgrids in ground penetrating radar {FDTD} models. *Journal of Applied Geophysics*, 67(4):309 – 317, 2009. Advanced Applications, Systems and Modelling for {GPR}.
- [113] S. Dey and R. Mittra. A locally conformal finite-difference time-domain {FDTD} algorithm for modeling three-dimensional perfectly conducting objects. *Microwave and Guided Wave Letters, IEEE*, 7:273–275, 1997.
- [114] S. Dey and R. Mittra. A locally conformal finite difference time domain technique for modeling arbitrary shaped objects. *Antennas and Propagation Society International Symposium, 1998. IEEE*, 1:584–587, 1998.
- [115] Wenhua Yu and Raj Mittra. A conformal fdtd algorithm for modeling perfectly conducting objects with curve-shaped surfaces and edges. *Microwave and Optical Technology Letters*, 27(2):136–138, 2000.
- [116] U. Schröter and D. Heitmann. Surface-plasmon-enhanced transmission through metallic gratings. *Phys. Rev. B*, 58:15419–15421, Dec 1998.
- [117] H. F. Ghaemi, Tineke Thio, D. E. Grupp, T. W. Ebbesen, and H. J. Lezec. Surface plasmons enhance optical transmission through subwavelength holes. *Phys. Rev. B*, 58:6779–6782, Sep 1998.
- [118] J. A. Porto, F. J. García-Vidal, and J. B. Pendry. Transmission resonances on metallic gratings with very narrow slits. *Phys. Rev. Lett.*, 83:2845–2848, Oct 1999.

- [119] Michaël Sarrazin, Jean-Pol Vigneron, and Jean-Marie Vigoureux. Role of wood anomalies in optical properties of thin metallic films with a bidimensional array of subwavelength holes. *Phys. Rev. B*, 67:085415, Feb 2003.
- [120] E. Popov, M. Nevière, S. Enoch, and R. Reinisch. Theory of light transmission through subwavelength periodic hole arrays. *Phys. Rev. B*, 62:16100–16108, Dec 2000.
- [121] A Krishnan, T Thio, T.J Kim, H.J Lezec, T.W Ebbesen, P.A Wolff, J Pendry, L Martín-Moreno, and F.J Garcia-Vidal. Evanescently coupled resonance in surface plasmon enhanced transmission. *Optics Communications*, 200(16):1 – 7, 2001.
- [122] L. Martín-Moreno, F. J. García-Vidal, H. J. Lezec, K. M. Pellerin, T. Thio, J. B. Pendry, and T. W. Ebbesen. Theory of extraordinary optical transmission through subwavelength hole arrays. *Phys. Rev. Lett.*, 86:1114–1117, Feb 2001.
- [123] Laurent Salomon, Frédéric Grillot, Anatoly V. Zayats, and Frédérique de Fornel. Near-field distribution of optical transmission of periodic subwavelength holes in a metal film. *Phys. Rev. Lett.*, 86:1110–1113, Feb 2001.
- [124] T. López-Rios, D. Mendoza, F. J. García-Vidal, J. Sánchez-Dehesa, and B. Panetier. Surface shape resonances in lamellar metallic gratings. *Phys. Rev. Lett.*, 81:665–668, Jul 1998.
- [125] Ph Lalanne, J P Hugonin, S Astilean, M Palamaru, and K D Möller. One-mode model and airy-like formulae for one-dimensional metallic gratings. *Journal of Optics A: Pure and Applied Optics*, 2(1):48, 2000.
- [126] S Astilean, Ph Lalanne, and M Palamaru. Light transmission through metallic channels much smaller than the wavelength. *Optics Communications*, 175(46):265 – 273, 2000.
- [127] J.M. Vigoureux. Analysis of the ebbesen experiment in the light of evanescent short range diffraction. *Optics Communications*, 198(46):257 – 263, 2001.
- [128] Te-Kao Wu and Shung-Wu Lee. Multiband frequency selective surface with multiring patch elements. *Antennas and Propagation, IEEE Transactions on*, 42(11):1484–1490, Nov 1994.
- [129] Carsten Winnewisser, Frank Lewen, Jochen Weinzierl, and Hanspeter Helm. Transmission features of frequency-selective components in the far infrared determined by terahertz time-domain spectroscopy. *Appl. Opt.*, 38(18):3961–3967, Jun 1999.

- [130] F. J. García de Abajo. *Colloquium* : Light scattering by particle and hole arrays. *Rev. Mod. Phys.*, 79:1267–1290, Oct 2007.
- [131] Peter B. Catrysse and Shanhui Fan. Propagating plasmonic mode in nanoscale apertures and its implications for extraordinary transmission. *Journal of Nanophotonics*, 2(1):021790–021790, 2008.
- [132] R. Gordon, A.G. Brolo, D. Sinton, and K.L. Kavanagh. Resonant optical transmission through hole-arrays in metal films: physics and applications. *Laser & Photonics Reviews*, 4(2):311–335, 2010.
- [133] Carl Schlockermann Michael I. Haftel and Girsh Blumberg. Role of cylindrical surface plasmons in enhanced transmission. *Appl. Phys. Lett.*, 88:193104, 2006.
- [134] Yannick P. Salvi J. Van Labeke D. Baida, F. I. and Guizal B. Extraordinary transmission beyond the cut-off through sub-annular aperture arrays. *Opt. Commun.*, 282:1463–1466, 2009.
- [135] F. I. Baida. Enhanced transmission through subwavelength metallic coaxial apertures by excitation of the {TEM} mode. *Appl. Phys. B*, 89:145–149, 2007.
- [136] A. Moreau, G. Granet, F. I. Baida, and D. Van Labeke. Light transmission by subwavelength square coaxial aperture arrays in metallic films. *Opt. Express*, 11:1131–1136, 2003.
- [137] F.I. Baida, Y. Poujet, B. Guizal, and D. Van Labeke. New design for enhanced transmission and polarization control through near-field optical microscopy probes. *Optics Commun.*, 256:190–195, 2005.
- [138] S. M. Orbons, M. I. Haftel, C. Schlockermann, D. Freeman, M. Milicevic, T. J. Davis, B. Luther-Davies, D. N. Jamieson, and A. Roberts. Dual resonance mechanisms facilitating enhanced optical transmission in coaxial waveguide arrays. *Opt. Lett.*, 33:821–823, 2008.
- [139] Abdoulaye Ndao. *Métamatériaux métalliques à transmission exaltée à base d'ouvertures annulaires sub-longueur d'ondes : Excitation du mode TEM*. PhD thesis, Ecole doctorale SPIM, Université de Franche-Comté, 2013.
- [140] F. I. Baida, D. Van Labeke, and B. Guizal. Enhanced confined light transmission by single subwavelength apertures in metallic films. *Appl. Opt.*, 42:6811–6815, 2002.
- [141] Y. Poujet, J. Salvi, and F. I. Baida. 90% extraordinary optical transmission in the visible range through annular aperture metallic arrays. *Opt. Lett.*, 32:2942–2944, 2007.

- [142] Peter B. Catrysse and Shanhui Fan. Understanding the dispersion of coaxial plasmonic structures through a connection with the planar metal-insulator-metal geometry. *Applied Physics Letters*, 94(23), 2009.
- [143] C. T. Chan, Q. L. Yu, and K. M. Ho. Order- N spectral method for electromagnetic waves. *Phys. Rev. B*, 51:16635–16642, Jun 1995.
- [144] Belkhir Abderrahmane. *Extension de la modélisation par FDTD en nano-optique*. PhD thesis, Université de Franche-Comté, Ecole Doctorale SPIM, 2008.
- [145] M. Hamidi, C. Chemrouk, A. Belkhir, Z. Kebci, A. Ndao, O. Lamrous, and F. I. Baida. {SFM-FDTD} analysis of triangular-lattice AAA structure: Parametric study of the {TEM} mode. *Opt. Commun.*, 318:47–52, 2014.
- [146] Hocheol Shin, Peter B. Catrysse, and Shanhui Fan. Effect of the plasmonic dispersion relation on the transmission properties of subwavelength cylindrical holes. *Phys. Rev. B*, 72:085436, Aug 2005.
- [147] Bo Hou, Jun Mei, Manzhu Ke, Weijia Wen, Zhengyou Liu, Jing Shi, and Ping Sheng. Tuning fabry-perot resonances via diffraction evanescent waves. *Phys. Rev. B*, 76:054303, Aug 2007.
- [148] N. Ashcroft and N. D. Mermin. *Solid of physics*. EDP Sciences, Les Ulis,, 2002.
- [149] A. Belkhir, O. Arar, S. S. Benabbes, O. Lamrous, and F. I. Baida. Implementation of dispersion models in the split-field–finite-difference-time-domain algorithm for the study of metallic periodic structures at oblique incidence. *Phys. Rev. E*, 81:046705, Apr 2010.
- [150] A. Belkhir and F. I. Baida. Three-dimensional finite-difference time-domain algorithm for oblique incidence with adaptation of perfectly matched layers and nonuniform meshing: Application to the study of a radar dome. *Phys. Rev. E*, 77:056701, 2008.
- [151] Elsie Barakat, Maria-Pilar Bernal, and Fadi Issam Baida. Doubly resonant Ag-LiNbO₃ embedded coaxial nanostructure for high second-order nonlinear conversion. *J. Opt. Soc. Am. B*, 30(7):1975–1980, Jul 2013.
- [152] S. Nosal. *Electromagnetic modeling of periodic structures and artificial materials. Application to the design of a bandpass radome*. PhD thesis, Ecole Centrale Paris, 2009.
- [153] A. Ndao, A. Belkhir, R. Salut, and F. I. Baida. Slanted annular aperture arrays as enhanced-transmission metamaterials: Excitation of the plasmonic transverse electromagnetic guided mode. *Appl. Phys. Lett.*, 103:211901, 2013.

BIBLIOGRAPHY

- [154] A.-L. Fehrembach, D. Maystre, and A. Sentenac. Phenomenological theory of filtering by resonant dielectric gratings. *J. Opt. Soc. Am. A*, 19:1136–1144, 2002.
- [155] E. Popov, L. Mashev, and D. Maystre. Theoretical study of the anomalies of coated dielectric gratings. *Opt. Acta*, 33(5):607–619, 1986.
- [156] A.-L. Fehrembach and A. Sentenac. Study of waveguide grating eigenmodes for unpolarized filtering applications. *J. Opt. Soc. Am. A*, 20:481–488, 2003.
- [157] A.-L. Fehrembach, K. Chan Shin Yu, A. Monmayrant, P. Arguel, A. Sentenac, and O. Gauthier-Lafaye. Tunable, polarization independent, narrow-band filtering with one-dimensional crossed resonant gratings. *Opt. Lett.*, 36:1662–1664, 2011.

LIST OF FIGURES

2.1	Absorption efficiency by capped cylinder and hollow nanosphere in (a) VIS range and (b) NIR range. The DDA method is used to get the spectra of capped cylinder and Mie theory is used to get spectra of hollow nanosphere. Ref. [43].	9
2.2	(a) Calculated absorption (solid lines) and scattering (dashed lines) efficiencies for a cubic (blue) and a ring (green) shaped silver NP. The particles have similar dimensions, both the side of the cube and the diameter of the ring are 50 nm. (b) Experimental measurement of scattering spectra of silver nanobars. (c) Electric field intensity enhancement corresponding to the three lowest longitudinal LSPRs. Note that, the color map of the field amplitude scale from 0.1 (blue) to 100 (red). The bottom sketches depict the instantaneous charge distributions for three plasmonic resonances. Ref. [14].	10
2.3	Plasmonic resonance in diabolo nanoantenna and its near-field enhancement. The hot spot is due the strong magnetic field. Ref. [18].	12
2.4	Schematic illustration of the two types of plasmonic nanostructures. (a) The excitation of free electrons leads to create a propagating surface plasmon (PSP). This mode propagate along the surface of the metal nanostructure. (b) The surface charges are locally oscillated around the metal nanoparticles. This is known as a localized surface plasmon resonance (LSPR). Refs. [82, 83, 52].	15
2.5	Real (blue curve) and imaginary (red curve) parts of the permittivity of gold in the optical region. The experimental data taken from Ref. [85].	20
2.6	Extinction, absorption and scattering cross sections of a sphere made of gold with a radius of (a) 10 nm, (b) 30 nm. In both cases, the refractive index of the environment is 1.5. The dielectric function database are taken from [85].	20

LIST OF FIGURES

2.7 An example of windows of FDTD calculation and regular mesh. 22

2.8 Yee cell in three dimensions. Note that the six components of electric and magnetic fields are represented in this cell. 24

2.9 Temporal discretization into the Yees scheme. 25

2.10 (a) Impedance matching principle. (b) Sketch of the PML principle. 28

2.11 Palik data of gold [108] (blue square) and comparison with the fitted permittivities using Drude (solid red curve), DL (dashed green curve) and DCP (solid black curve) models (a) real part (b) imaginary part. 32

2.12 Palik data of silver [108] (blue square) and comparison with the fitted permittivities using Drude (solid red curve), DL (dashed green curve) and DC (solid black curve) models (a) real part (b) imaginary part. 33

2.13 Schematic represents the FDTD computational domain including two distinct TF and SF zones in the case of 1D. 34

2.14 Sketch of the simulation for (a) a plan wave hitting a scatterer. The field scattering from the structure is the solitary field in region SF and hit the PML (b) The lower left corner of the FDTD problem space showing the position of nodes for 2D TM_z problem. Note that the bold E and H components indicate the nodes that need to modify the update equations. 36

2.15 E_z field in a computational domain using a TF/SF technique. The modulus of the electric field in xOy plane are taken at time-steps (a) 120, (b) 180, and (c) 270. Note that the $dt = 4.0028 \times 10^{-17}$ s. 39

2.16 E_z field with dielectric cylinder ($n_s = 2$ in a computational domain using a TF/SF technique. The modulus of the electric field in xOy plane are taken at time-steps (a) 180, (b) 240, and (c) 360. $dt = 4.0028 \times 10^{-17}$ 40

2.17 3 – D computational domain which contains a TF/SF boundary ($\mathbf{i}_a, \mathbf{j}_a, \mathbf{k}_a, \mathbf{i}_b, \mathbf{j}_b$ and \mathbf{k}_b) and the nodes that are used in the corrections. 41

2.18 Sketch showing an arbitrary particle illuminated with plane wave, a part of incident light is scattered by the particle. Note that electromagnetic fields E_{tot}, H_{tot} decompose of incident and scattered components. 43

LIST OF FIGURES

2.19 Computational domain in the case of a metal sphere which contains a TF/SF boundary 45

2.20 Scattering efficiency of aluminum nanosphere with radius ($R = 60 \text{ nm}$) and grid size ($\Delta = 5 \text{ nm}$) is calculated with FDTD (solid blue curve) and Mie (solid red curve). The target is illuminated by plane wave in a vacuum. . . . 46

2.21 (a) Scheme illustrates the defects resulting from using a uniform structured mesh in the case of a sphere. (b) Zoom for a $2D$ cell Yee in (b) shows the principle of the CPT. 48

2.22 Meshing of a 2D nano-cylinder made of glass placed in air (a) staircase, (b) CPT. 49

2.23 Scattering efficiency of nanosphere made in aluminum with radius ($R = 60 \text{ nm}$) is calculated using (a) Classic FDTD code for two values of mesh size $\Delta = 5 \text{ nm}$ (solid green curve) and $\Delta = 2 \text{ nm}$ (solid red curve). (b) CPT-FDTD (dashed red curve) compared with Mie (solid blue curve). The target is illuminated by a plane wave in a vacuum. 50

2.24 Relative error on the scattering efficiency calculated by both FDTD and Mie. The FDTD calculation without CPT technique has two values of mesh size $\Delta = 5 \text{ nm}$ (solid green curve) and $\Delta = 2 \text{ nm}$ (solid red curve). The solid blue curve represents CPT one. 51

2.25 Schema showing 3D view of two different nanoantenna configurations (a) bowtie nanoantenna and (b) diabolo nanoantenna under study having the same values of geometric parameters, thickness t , gap g and length D . For both NAs, we consider an incident field with a polarization along its long axis. Note that both NAs are immersed in water. 52

2.26 (a) Calculated extinction (solid curves), scattering (dashed curves) and absorption (dotted curves) efficiencies for two different NAs: bowtie (blue curves) and diabolo nanoantenna (red curves). The two NAs have the same values of metal thickness $t = 25 \text{ nm}$, gap $g = 25 \text{ nm}$ and length $D = 135 \text{ nm}$ and both NAs are immersed in water. (b) and (c) calculated square root of the electric and magnetic amplitude distribution respectively in the xOy plane in the vicinity of BNA. (d) and (e) the same as in (b,c) but for DA. Note that the intensity distribution is calculated in the total field region. 54

2.27 The energy flow distribution (in color map) passing through the middle of Diabolo NA in a vertical xOz plane. Yellow arrows correspond the tangential Poynting vector. Dimensions of the diabolo NA are: thickness $t = 20 \text{ nm}$, gap $g = 25 \text{ nm}$ and length $D = 135 \text{ nm}$. The incident field with a polarization along its long axis. 55

2.28 Optical responses (extinction (solid curves), scattering (dashed curves) and absorptions (dotted curves) of diabolo nanoantenna made of gold (black curves), silver (red curves) and aluminum (blue curves), with $D = 135 \text{ nm}$, $g = 25 \text{ nm}$ and $t = 25 \text{ nm}$. Note that the diabolo NA is placed in water medium. 56

2.29 Sensitivity of the scattering responses to the refractive index of the surrounding medium for a silver daibolo nanoantenna with $D = 135 \text{ nm}$, $g = 25 \text{ nm}$ and $t = 25 \text{ nm}$, blue (in air), green (in water), red (in oil). 58

2.30 Evolution of the scattering efficiency with length of silver DA, g and t are 25 nm . Note that the diabolo NA is placed in water medium. 59

2.31 Scattering efficiency with the gap size of DA made in silver, D and t are 135 nm and 25 nm respectively. The water is considered as a medium. . . . 59

2.32 Dependency of the scattering efficiency on the thickness t of DA made in silver, D and g are 135 nm and 25 nm respectively. The diabolo NA is placed in water medium. 60

3.1 Zero-order transmission spectra of an Ag array (period (a_o) = 900 nm , diameter= 150 nm and thickness= 200 nm). Ref. [26]. 64

3.2 Theoretical and experimental transmission spectra of extraordinary optical transmission EOT structures based on cylindrical holes engraved into opaque metallic layer. (a) Experimental zero-order transmission spectra of Au film on a quartz substrate, the film thickness is $h = 250 \text{ nm}$, the hole radius is $b = 100 \text{ nm}$ and the lattice constant is $a_o = 600 \text{ nm}$. Ref. [121] (b) Experimental (solid curve) and analytical model (dotted curve) of zero-order power transmittance at normal incidence for a square array of holes ($a_o = 750 \text{ nm}$ and $b = 140 \text{ nm}$) in a free standing Ag film $h = 320 \text{ nm}$. Ref. [122] 66

3.3 Theoretical study of extraordinary optical transmission EOT in AAAs structure. (a) Transmission spectra of a square array of coaxial cylinders, spaced at $d = 555 \text{ nm}$ and for various inner radii (Au cylinders) R_1 and metal thickness L . Note that the outer radii (silica cylinder) is fixed to $R_2 = 100 \text{ nm}$. The arrows indicate the theoretical $m = 0$ and $m = 1$ cylindrical surface plasmon (CSP) resonance peaks. The top panel includes the cases of a perfectly conducting (PC) and a periodicity of $d = 888 \text{ nm}$ (which has the same predicted resonance positions as the $R_1 = 50 \text{ nm}$, $L = 290 \text{ nm}$ case in the second panel). Ref. [133]. (b) Transmission spectrum through a silver layer perforated with annular apertures arranged into a square array. The period is $p = 350 \text{ nm}$, the inner and the outer radii of the coaxial cavities are $R_i = 75 \text{ nm}$ and $R_o = 100 \text{ nm}$, respectively. The metal thickness is set to $h = 100 \text{ nm}$ and the structure is illuminated by a linearly polarized plane wave at normal incidence. Ref. [134]. 67

3.4 Three different kinds of waveguide made in perfectly electric conductor (PEC) with their cutoff wavelengths of the first guided modes. 70

3.5 Different kinds of the guided modes and their cutoff wavelengths in the case of cylindrical and coaxial nano-waveguides made in a perfect conductor (gray) and in silver (blue). Cylindrical radius is set to $R = 100 \text{ nm}$ and corresponds to the outer radius R_o of the coaxial structure whereas the inner radius of this latter is set to $R_i = 50 \text{ nm}$. Note that the $\Delta\lambda$ represents the difference between the two cutoff positions of the two fundamental modes. This value, estimated here as $2R$, can be used to quantify the gain due to the coaxial structure. This figure is reproduced from Ref. [29] 71

3.6 Dispersion diagrams of guided modes of an coaxial waveguide made in silver (red curves) and PEC (blue curves). The inner and outer radius are fixed to $R_i = 50 \text{ nm}$ and $R_o = 150 \text{ nm}$ respectively. 72

3.7 Distribution of the intensity light for the first three-guided modes of a coaxial waveguide made in silver with: $R_o = 75 \text{ nm}$ and $R_i = 50 \text{ nm}$ 73

3.8 (a) Transmission spectra of AAA structure made in a perfect conductor their geometric parameters have been adjusted by setting the inner and outer radius to $R_i = p/4$ and $R_o = p/3$ respectively, p being the period of the AAA structure. The structure is illuminated by a TM polarized plan wave at angle of incidence of $\theta = 40^\circ$. Note that the spectral response presents extra peaks denoted by the point A due to the excitation of TEM guided mode inside each coaxial aperture. Modulus of the radial (b) and azimuthal (c) electric field components calculated at $p/2$ from exit side of the structure for the parameter of point A in (a). These two quantities are normalized according to the maximum of the radial component. Ref. [135] . 74

3.9 Schematic of a conventional Annular Apertures Array (AAA) structure. R_o and R_i are the outer and inner radius respectively, p the period and θ is the angle of incidence at the substrate-metal interface and β is the angle of incidence in the superstrate. 77

3.10 Theoretical transmission spectra for different outer radius R_o . The inner radius R_i is fixed to 50 nm , the period $p = 400\text{ nm}$, the silver thickness is set to $h = 200\text{ nm}$ and the incidence angle $\theta = 20^\circ$ (i.e. $\beta = 30^\circ$). The red arrow indicates the transmission spectra of the chosen parametric. 80

3.11 Zero-order theoretical transmission spectra trough an AAA structure versus the height h of silver for a transverse magnetic (TM) polarization illuminated at $\theta = 20^\circ$ (i.e. $\beta = 30^\circ$). The other geometrical parameters are $R_i = 50\text{ nm}$, $R_o = 150\text{ nm}$, $h = 200\text{ nm}$ and $p = 400\text{ nm}$ 81

3.12 Theoretical transmission spectra for different period p values. The inner radius R_i is fixed to 50 nm , $R_o = 150\text{ nm}$, $h = 200\text{ nm}$ and the incidence angle $\theta = 20^\circ$ (i.e. $\beta = 30^\circ$). 82

3.13 (a) SEM top view image of the studied AAA (30×30 apertures) engraved in silver film. (b) zoom-in over 6×9 patterns. (c) 52° titled zoom-in over 4×4 apertures. (d) Vertical cross-section made on the structure after it was filled in with platinum. Ref. [139] 84

3.14	Experimental (solid line) and theoretical (dashed line) transmission spectra at $\theta = 20^\circ$ (i.e. $\beta = 30^\circ$) through an AAA made in silver for both (a) TM and (b) TE polarizations. Numerical simulations are performed with the geometrical parameters : $R_i = 50nm$, $R_o = 145nm$ and $h = 190nm$. The vertical arrows show surface plasmons resonance (SPR) positions and the colored area marks the position of the peak due to the excitation of the <i>TEM</i> guided mode. The <i>TEM</i> mode is only excited with a TM polarization: no peak appears around 900 nm in TE polarization.	86
4.1	(a) Schematic of one annular aperture section in the xOy plan giving the geometrical parameters (outer radius $R_o = 150\text{ nm}$, inner radius $R_i = 50\text{ nm}$). (b) Schema of the xOz and yOz sections showing the metallic film with thickness $h = 190\text{ nm}$ perforated with SAAA. Note that the tilted angle $\alpha = 30^\circ$ of the aperture axis belongs to the xOz plan. (c) Sketch of the whole sample with SAAA structure and the reference zone used to normalize the transmitted signal. Ref. [153].	90
4.2	(Top) Study of the influence of the inner radius in perfect conductor (a) and real metal (silver) (b). The outer radius is fixed to $R_o = 150\text{ nm}$. (Bottom) Study of the influence of the outer radius in perfect conductor (c) and real metal (silver) (d). The inner radius is fixed to $R_i = 50\text{ nm}$. Note that The structure is illuminated by a linearly TM polarized plane wave at normal incidence with an angle of inclinations $\alpha = 30^\circ$ and the period equal to $p = 400\text{ nm}$. Ref. [139].	92
4.3	(a) Schematic of the infinite coaxial waveguide considered for the determination of the real and imaginary part of the effective index and the dispersion diagram of the TE_{11} and the <i>TEM</i> guided modes. (b) Dispersion curves for waveguides made in gold (red lines) or silver (blue lines) when $R_i = 50\text{ nm}$ and $R_o = 150\text{ nm}$. (c) Real part (black curves: Ag in dashed and Au in solid lines) and imaginary part (green curves: Ag in dashed and Au in solid lines) of the effective index of the TE_{11} mode calculated from (b). (d) corresponding curves as in (c) for the <i>TEM</i> mode. Ref. [153].	93
4.4	Top view SEM image of the studied SAAA matrix engraved in silver film. (b) is a zoom-in made over 3×3 patterns imaged in the Oy direction to point out the slanted apertures. (c) is a zoom-in made over 3×2 apertures in the Ox direction. Ref. [153].	94

- 4.5 Zero-order (a) experimental and (b) theoretical transmission spectra of the SAAA structure as a function of wavelength for the two cases of polarization: $E_{inc} // Ox$ (solid blue line) and $E_{inc} // Oy$ (dashed red line). The *TEM* guided mode is only excited when the incident electric field has a non-zero component along the aperture axis (here TM polarization). Ref. [153]. . . . 95
- 4.6 (a) 3D view of the Slanted Annular Aperture Array (SAAA) structure under consideration. (b) Schema showing the different geometrical parameters used to assign the incident wave-vector position (in the plane formed by the Oz axis at an angle ϕ from the Ox axis) and direction (incidence angle θ counted from the Oz axis). The aperture axis is tilted by an angle α from the vertical direction (Oz) in a plane also located at an angle β from the Ox axis). The horizontal section of on aperture has then outer (inner) ellipses with minor half axis R_o (R_i) and major $R_o / \cos \alpha$ ($R_i / \cos \alpha$). 97
- 4.7 Calculated transmission spectra for two different configurations (a) having the same metal thickness $h = 2p/3$ where p is the period along Ox and Oy directions. (b) The red curve represents the transmission through the SAAA structure at normal incidence while the blue one corresponds to the transmission through the AAA structure. For both structures, we consider a TM polarized incident plane wave with $\phi = \beta = 0^\circ$ (see Fig. 4.6) but $\theta = 0^\circ$ and $\alpha = 30^\circ$ for the SAAA structure and $\theta = 30^\circ$ in the case of the AAA structure. For the two configurations, we fixed the radii values to $R_o = p/3$ and $R_i = p/6$ 98
- 4.8 (a) Transmission spectra in color level versus the tilt angle α of a SAAA with metal thickness $h = 2p/3$ (p is the period of the grating along the Ox and Oy directions), the inner and outer radii of the coaxial cavities are $R_i = p/6$ and $R_o = p/3$ respectively. The structure is illuminated by a TM polarized plane wave at normal incidence with $\phi = \beta = 0^\circ$. (b) The solid blue curve is the spectral position of the *TEM*-based transmission peak function of $1 / \cos(\alpha)$. The dashed red curve corresponds to the asymptotic linear behavior when we consider ϕ_r constant. 99

4.9 (a) Calculated transmission spectra in color level versus the angle of incidence. Inset of (a) presents the illumination direction with respect to the tilt angle. Two Rayleigh anomalies can be seen in the figure and are indicated by the value of the (m, l) corresponding to diffracted order (m along x and l along y axis). (b) two cross-sections made on (a) and illustrating the transmission spectra for two angles of incidence $\theta = 40^\circ$ in solid blue line and $\theta = -40^\circ$ in dashed red line. Note that the up- and down-arrows indicate the position of TEM -based transmission peak and the Rayleigh anomaly respectively whereas the value of the tilt angle is fixed to $\alpha = 35^\circ$. The inset of (b) shows the residual numerical signal ($\Delta = |T(\theta = 40^\circ) - T(\theta = -40^\circ)|$) corresponding to the difference between the two spectra only in the sub- λ regime. 100

4.10 (a) Calculated transmission spectra in the case of TE polarization in color level versus the angle of incidence. Two Rayleigh anomalies can be seen in the figure and are indicated by the value of the (m, l) corresponding to diffracted order (m along x and l along y axis). (b) two cross-sections made on (a) and illustrating the transmission spectra for two angles of incidence $\theta = 40^\circ$ in solid blue line and $\theta = -40^\circ$ in dashed red line. Note that the up- and down-arrows indicate the position of the Rayleigh anomaly respectively whereas the value of the tilt angle is fixed to $\alpha = 35^\circ$ 101

4.11 (Top) Calculated transmission spectra in color level in both TM (a) and TE (b) polarizations versus the angle of incidence. Two Rayleigh anomalies can be seen in the figure and are indicated by the value of the (m, l) corresponding to diffracted order (m along x and l along y axis). (Bottom) two cross-sections in both TM (c) and TE (d) polarizations made on (a) and (b) respectively, illustrating the transmission spectra for two angles of incidence $\theta = 40^\circ$ in solid blue line and $\theta = -40^\circ$ in dashed red line. Note that the up- and down-arrows indicate the position of the Rayleigh anomaly respectively whereas the value of the tilt angle is fixed to $\alpha = 35^\circ$ and for an arbitrary azimuthal angle $\phi = 35^\circ$ 102

4.12 Transmission spectra for different azimuthal angles ϕ values in both TM (a) and TE (b) polarizations for an angle of incidence of $\theta = 30^\circ$. (c) Cross-sections made over (a) and (b) at $\phi = 37.5^\circ$. (d) Transmission efficiencies at λ_{TEM} of the two polarization states (TM in dashed red line and TE in solid blue line) and their sum (green horizontal line) as a function of the azimuthal angle ϕ 103

4.13 Transmission spectra for different angles of incidence in both TE (a) and TM (b) polarizations obtained for an arbitrary azimuthal angle $\phi = 30^\circ$. (c) Cross-sections made over (a) and (b) at $\theta = 37.5^\circ$. (d) Transmission efficiencies at λ_{TEM} of the two polarization states (TM in dashed red line and TE in solid blue line) and their sum (green horizontal line) as a function of the angle of incidence θ 104

4.14 Transmission spectra of an arbitrary SAAA structure where $\beta = 25^\circ$, $R_o = p/3$, $R_i = p/6$, $h = 2p/3$ illuminated by a linearly polarized plane wave with $\phi = 65^\circ$ and $\theta = -35^\circ$. (a) The solid blue line corresponds to the case of a TM polarization while the dashed red one fits the case of a TE polarization. The dotted black line presents the transmission of an unpolarized incident beam. (b) Transmission spectra for the two polarization states (P_{max}, P_{min} that correspond to the two eigenvalues of the matrix $T_1^* T_1$). Note that the polarization states P_{max} and P_{min} vary with the wavelength. The dotted black line is the same as in (a) because it equals to $(P_{max} + P_{min})/2 = (TE + TM)/2$ 106

4.15 Transmission spectra for an angle of incidence $\theta = 75^\circ$ in (a) and $\theta = -75^\circ$ in (b) for the same SAAA structure of Fig. 4.7. (c) Square root of the electric field amplitude distributions (in color map) around the nano-structured metallic film in a vertical plane containing the aperture axis for an illumination at $\theta = 75^\circ$. White arrows correspond the tangential Poynting vector. (d) Same as (c) for $\theta = -75^\circ$ 107

B.1 General scheme of a structure exhibiting a central symmetry in (a) and the reciprocal configuration in (b). 146

LIST OF TABLES

2.1	Permittivities of gold for Drude, DL and DCP models are optimized using Δ function over 300 – 2000 <i>nm</i> wavelength range	31
2.2	Permittivities of silver for Drude, DL and DCP models are optimized using Δ function over 300 – 2000 <i>nm</i> wavelength range	32
2.3	The accuracy of both CPT-FDTD and classic FDTD used in the calculation of the scattering efficiency with different values of mesh size.	51
2.4	Permittivity of aluminum for DCP model is optimized using Δ function presented previously in section 2.8.4 over 300 – 2000 <i>nm</i> wavelength range . .	56



APPENDICES

A

A.1/ DISSIPATION OF ENERGY

The Poynting vector is defined as:

$$\vec{P} = \vec{E} \wedge \vec{H} \quad (\text{A.1})$$

where \vec{E} and \vec{H} are the electric and magnetic field vectors respectively. The energy flux going outside an enclosed volume (V) delimited by a surface (S):

$$\Phi = \int \int_S \vec{P} \cdot d\vec{s} \quad (\text{A.2})$$

where $\int \int_S$ is a surface integral over the surface S and $d\vec{s}$ denotes the differential vector element of surface area S , normal to surface. The time-average energy collected by a conventional detector (having integration time larger than the light period) is given by:

$$\langle \Phi \rangle = \frac{1}{\tau} \int_0^\tau \left(\int \int_S \vec{P} \cdot d\vec{s} \right) d\tau \quad (\text{A.3})$$

therefore the relation energy loss Λ is defined as:

$$\Lambda = -\langle \Phi \rangle \quad (\text{A.4})$$

By using of Ostrogradsky theorem, one can write Λ as:

$$\Lambda = -1/\tau \int \int \int \text{div}(\vec{P}) dV \quad (\text{A.5})$$

Since the energy is real, we must consider real notations for all the electromagnetic

A.1. DISSIPATION OF ENERGY

fields. Keeping the complex values of these fields, one can express their real part as:

$$\vec{E} = \frac{1}{2}(\vec{E}e^{-i\omega t} + \vec{E}^*e^{i\omega t}), \quad (\text{A.6})$$

$$\vec{D} = \frac{1}{2}(\vec{D}e^{-i\omega t} + \vec{D}^*e^{i\omega t}), \quad (\text{A.7})$$

$$\vec{H} = \frac{1}{2}(\vec{H}e^{-i\omega t} + \vec{H}^*e^{i\omega t}), \quad (\text{A.8})$$

$$\vec{B} = \frac{1}{2}(\vec{B}e^{-i\omega t} + \vec{B}^*e^{i\omega t}), \quad (\text{A.9})$$

To evaluate the energy loss Λ , we will use the Poynting theorem (conservation of energy for EM field) that is given by:

$$-\nabla \cdot \vec{P} = \vec{J} \cdot \vec{E} + \vec{E} \cdot \frac{\partial \vec{D}}{\partial t} + \vec{H} \cdot \frac{\partial \vec{B}}{\partial t} \quad (\text{A.10})$$

where $\nabla \cdot \vec{P}$ is the divergence of the Poynting vector and J is the free current density corresponding to the motion of charges, therefore, the time derivative of the \vec{D} and \vec{E} writes from Eq. A.7 as:

$$\frac{\partial \vec{D}}{\partial t} = \frac{1}{2}(-i\omega \vec{D}e^{-i\omega t} + i\omega \vec{D}^*e^{i\omega t}) \quad (\text{A.11})$$

By using the constitutive relation $\vec{D} = \epsilon \vec{E}$ one gets:

$$\frac{\partial \vec{D}}{\partial t} = \frac{1}{2}(-i\omega \epsilon \vec{E}e^{-i\omega t} + i\omega \epsilon^* \vec{E}^*e^{i\omega t}) \quad (\text{A.12})$$

After multiplying Eq. A.12 by Eq. A.6, one obtains:

$$\vec{E} \cdot \frac{\partial \vec{D}}{\partial t} = \frac{1}{4} \left[-i\omega \epsilon \vec{E} \cdot \vec{E}e^{-2i\omega t} + i\omega \epsilon^* \vec{E}^* \cdot \vec{E}^*e^{2i\omega t} + i\omega \epsilon^* \vec{E} \cdot \vec{E}^* - i\omega \epsilon \vec{E}^* \cdot \vec{E} \right] \quad (\text{A.13})$$

Now, due to the time-averaging in eq. A.13, the terms $\vec{E} \cdot \vec{E}$ and $\vec{E}^* \cdot \vec{E}^*$ will not contribute to the energy value due to the fact they still oscillate in time (because these terms still oscillate in time as $e^{\mp 2i\omega t}$). Only the $\vec{E} \cdot \vec{E}^*$ and $\vec{E}^* \cdot \vec{E}$ terms (two last terms of Eq. A.13) are involved through:

$$\frac{1}{\tau} \int_0^\tau (\vec{E} \cdot \frac{\partial \vec{D}}{\partial t}) d\tau = \frac{1}{4} i\omega (\epsilon^* - \epsilon) \vec{E} \cdot \vec{E}^* \quad (\text{A.14})$$

By the same way, one obtains:

$$\frac{1}{\tau} \int_0^\tau (\vec{H} \cdot \frac{\partial \vec{B}}{\partial t}) d\tau = \frac{1}{4} i\omega (\mu^* - \mu) \vec{E} \cdot \vec{E}^* \quad (\text{A.15})$$

In addition, the conductivity σ of metals is assumed to be real, and links the J vector to the electric field through the relation: $J = \sigma E$, then:

$$\Lambda = -\langle \Phi \rangle = -\frac{1}{\tau} \int_0^\tau d\tau \left[\int \int \int_v \nabla \vec{P} \cdot dV \right] \quad (\text{A.16})$$

$$= \int \int \int_v dV \left[\frac{1}{2} \sigma |\vec{E}|^2 + \frac{1}{2} \omega \varepsilon_o \varepsilon'' |\vec{E}|^2 + \frac{1}{2} \omega \mu_o \mu' |\vec{H}|^2 \right] \quad (\text{A.17})$$

the first, second and third term represent the called Joule effect, dielectric loss and magnetic loss respectively, with $(\varepsilon^* - \varepsilon) = 2i\varepsilon''$. If we put $\varepsilon_{r\text{ eff}} = \varepsilon_r - \frac{\sigma}{i\varepsilon_o\omega}$, we can find the two terms (Joule effect and dielectric loss) as:

$$\Lambda = \int \int \int_v dV \left[\frac{1}{2} \omega \varepsilon_o \varepsilon'_{r\text{ eff}} |\vec{E}|^2 + \frac{1}{2} \omega \mu_o \mu' |\vec{H}|^2 \right] \quad (\text{A.18})$$

in the visible range $\mu = \mu_o$ whatever the medium, therefore, there is no magnetic loss:

$$\Lambda = \frac{1}{2} \int \int \int_v \left[\omega \varepsilon_o \varepsilon'_{r\text{ eff}} |\vec{E}|^2 dV \right] \quad (\text{A.19})$$

B.1/

We consider a periodic structure composed of lossless materials which presents only one propagating diffraction order (the zero order). From the study of the scattering matrix of the structure, we will derive some properties of its transmittivity. This appendix is an extension of the works published in [155] and [154], and similar properties could be derived for the reflectivity.

In the following, we will first show that the eigenvalues of the transmittivity matrix for the energy, denoted $T_1^* T_1$ hereafter, are the limits of the variation of the transmittivity when the incident polarization takes all possible states, and that they are obtained for orthogonal polarizations (given by the eigenvectors). Thus, these eigenvalues are the key variables to understand the behavior of a sub-wavelength grating with respect to the incident polarization. This is true especially in the case where the eigenvectors are not simply the *TE* and *TM* vectors, which occurs in conical incidence or when particular eigenmodes are excited.

Second, using only the reciprocity theorem and the energy balance, and with no hypothesis on the symmetry of the structure, we will show that the eigenvalues of $T_1^* T_1$ are unchanged when the angle of incidence is changed in its opposite, hence generalizing a property that is well known for gratings illuminated in classical incidence (plane of incidence perpendicular to the grating grooves). This is a new result that was not published in [154].

Third, we consider structures having a central symmetry (examples are shown in Figs. 4.6 and B.1). This kind of symmetry was discussed in [155] which focused on gratings illuminated under classical incidence (plane of incidence containing a direction of periodicity) for which there is no polarization conversion, but it was not discussed in

[154]. We show that when one mode is excited, one eigenvalue of $T_1^* T_1$ reaches 100% at resonance. This means that the transmittivity is equal to 100% at the resonance wavelength when the incident polarization corresponds to that of the eigenvector associated with this eigenvalue, while the transmittivity is equal to the transmittivity of the structure out of resonance for the orthogonal polarization.

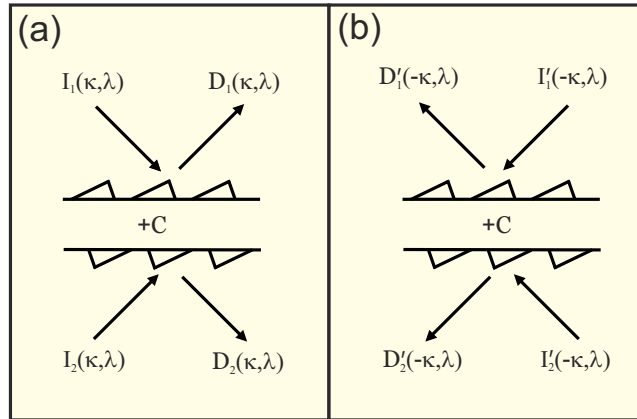


Figure B.1: General scheme of a structure exhibiting a central symmetry in (a) and the reciprocal configuration in (b).

B.1.1/ FROM THE SCATTERING MATRIX TO THE TRANSMITTIVITY

We start from the scattering matrix $S(\kappa, \lambda)$ relating the incoming field (from the substrate and the superstrate), with wavelength λ and wave-vector with in-plane component κ (lying in the xy -plane in Fig. B.1), to the field diffracted by the structure in the zero order of diffraction. The reader can refer to [154] (sections 2 and 3) for a full definition of the scattering matrix and of the TE and TM vectors associated to each incident and diffracted field (in the superstrate and the substrate). This 4×4 matrix is composed with 4 blocks:

$$S(\kappa, \lambda) = \begin{pmatrix} R_1(\kappa, \lambda) & T_2(\kappa, \lambda) \\ T_1(\kappa, \lambda) & R_2(\kappa, \lambda) \end{pmatrix}. \quad (\text{A1})$$

The reflection and transmission matrices R_j and T_j , where the subscript $j = 1$ (resp. $j = 2$) is used when the incident field comes from the superstrate (resp. substrate), are 2×2 matrix. They contain the reflection and transmission conversion coefficients of a TE or TM polarized field to a TE or TM polarized field. For example, T_1 writes as

$$T_1 = \begin{pmatrix} t_1^{SS} & t_1^{SP} \\ t_1^{PS} & t_1^{PP} \end{pmatrix}. \quad (\text{A2})$$

From the definition of the scattering matrix it follows that the energy τ transmitted in the substrate when the incident field comes from the superstrate only can be written as:

$$\tau = l_a^{T_1^* T_1} \left| \left\langle I_1 | V_a^{T_1^* T_1} \right\rangle \right|^2 + l_b^{T_1^* T_1} \left| \left\langle I_1 | V_b^{T_1^* T_1} \right\rangle \right|^2, \quad (\text{A3})$$

where $l_a^{T_1^* T_1}$ and $l_b^{T_1^* T_1}$, are the eigenvalues and $V_a^{T_1^* T_1}$ and $V_b^{T_1^* T_1}$ the eigenvectors of the matrix $T_1^* T_1$, and I_1 is a two-elements vector containing the *TE* and *TM* components of the amplitude of the incident field vector.

It is important to note that $T_1^* T_1$ is a hermitian matrix, thus its eigenvectors are orthogonal (in the sense of hermitian scalar product) to each other and its eigenvalues are real and positive. Hence, from Eq. A3, it follows that $l_a^{T_1^* T_1}$ and $l_b^{T_1^* T_1}$ are the limits of the variation of the transmittivity when the incident field takes all possible states of polarization (even non linear). These limits are obtained for two orthogonal polarizations. Moreover, for any two incident orthogonal polarizations, the sum of the transmittivity is equal to the sum of the eigenvalues.

B.1.2/ PROPERTIES OF THE SCATTERING MATRIX

Several properties of the scattering matrix can be deduced from the energy balance and the reciprocity theorem. Again, the demonstration is given in [154] (section 3 and 5), and only the results will be reported here. Note that in the following, we will need to consider the scattering matrix for complex wavelengths. Hence, we use an expression of the energy balance suitable for a complex variable λ with complex conjugate $\bar{\lambda}$:

$$R_1^*(\kappa, \bar{\lambda}) R_1(\kappa, \lambda) + T_1^*(\kappa, \bar{\lambda}) T_1(\kappa, \lambda) = \mathbf{1} \quad (\text{A4})$$

$$R_2^*(\kappa, \bar{\lambda}) R_2(\kappa, \lambda) + T_2^*(\kappa, \bar{\lambda}) T_2(\kappa, \lambda) = \mathbf{1} \quad (\text{A5})$$

$$R_1^*(\kappa, \bar{\lambda}) T_2(\kappa, \lambda) + T_1^*(\kappa, \bar{\lambda}) R_2(\kappa, \lambda) = \mathbf{0} \quad (\text{A6})$$

$$T_2^*(\kappa, \bar{\lambda}) R_1(\kappa, \lambda) + R_2^*(\kappa, \bar{\lambda}) T_1(\kappa, \lambda) = \mathbf{0} \quad (\text{A7})$$

where $\mathbf{1}$ stands for the unit diagonal matrix of size 2x2.

The reciprocity theorem entails that $S(-\boldsymbol{\kappa}, \lambda) = t(S(\boldsymbol{\kappa}, \lambda))$ (where $t(S)$ is the transpose of S) which can be written as:

$$R_1(-\boldsymbol{\kappa}, \lambda) = t(R_1(\boldsymbol{\kappa}, \lambda)) \quad (\text{A8})$$

$$R_2(-\boldsymbol{\kappa}, \lambda) = t(R_2(\boldsymbol{\kappa}, \lambda)) \quad (\text{A9})$$

$$T_2(-\boldsymbol{\kappa}, \lambda) = t(T_1(\boldsymbol{\kappa}, \lambda)). \quad (\text{A10})$$

Now, we shall demonstrate a property related to the symmetry of the structure with respect to a symmetry center C. We consider two configurations, as depicted in Fig. B.1. In the first configuration Fig. B.1(a) $I_1(\boldsymbol{\kappa}, \lambda)$ and $I_2(\boldsymbol{\kappa}, \lambda)$ are two elements vectors containing the amplitudes, in *TE* and *TM* polarizations, of the incident field coming from the superstrate and the substrate respectively, and $D_1(\boldsymbol{\kappa}, \lambda)$, $D_2(\boldsymbol{\kappa}, \lambda)$ stand for the diffracted field. In the second configuration Fig. B.1(b), the structure is illuminated with $I'_1(-\boldsymbol{\kappa}, \lambda)$ and $I'_2(-\boldsymbol{\kappa}, \lambda)$ in such a way that $I'_2(-\boldsymbol{\kappa}, \lambda)$ is the symmetric of $I_1(\boldsymbol{\kappa}, \lambda)$ with respect to the center of symmetry C, and $I'_1(-\boldsymbol{\kappa}, \lambda)$ is the symmetric of $I_2(\boldsymbol{\kappa}, \lambda)$:

$$\begin{aligned} I'_1(-\boldsymbol{\kappa}, \lambda) &= I_2(\boldsymbol{\kappa}, \lambda) \\ I'_2(-\boldsymbol{\kappa}, \lambda) &= I_1(\boldsymbol{\kappa}, \lambda). \end{aligned} \quad (\text{A11})$$

Because the structure is symmetric with respect to C, the two configurations are physically equivalent, and we can say that the same equality is verified for the diffracted field:

$$\begin{aligned} D'_1(-\boldsymbol{\kappa}, \lambda) &= D_2(\boldsymbol{\kappa}, \lambda) \\ D'_2(-\boldsymbol{\kappa}, \lambda) &= D_1(\boldsymbol{\kappa}, \lambda). \end{aligned} \quad (\text{A12})$$

From the definition of the scattering matrix, we write:

$$\begin{pmatrix} D'_1(-\boldsymbol{\kappa}, \lambda) \\ D'_2(-\boldsymbol{\kappa}, \lambda) \end{pmatrix} = \begin{pmatrix} R_1(-\boldsymbol{\kappa}, \lambda) & T_2(-\boldsymbol{\kappa}, \lambda) \\ T_1(-\boldsymbol{\kappa}, \lambda) & R_2(-\boldsymbol{\kappa}, \lambda) \end{pmatrix} \begin{pmatrix} I'_1(-\boldsymbol{\kappa}, \lambda) \\ I'_2(-\boldsymbol{\kappa}, \lambda) \end{pmatrix}, \quad (\text{A13})$$

and, on the other hand:

$$\begin{pmatrix} D_1(\boldsymbol{\kappa}, \lambda) \\ D_2(\boldsymbol{\kappa}, \lambda) \end{pmatrix} = \begin{pmatrix} R_1(\boldsymbol{\kappa}, \lambda) & T_2(\boldsymbol{\kappa}, \lambda) \\ T_1(\boldsymbol{\kappa}, \lambda) & R_2(\boldsymbol{\kappa}, \lambda) \end{pmatrix} \begin{pmatrix} I_1(\boldsymbol{\kappa}, \lambda) \\ I_2(\boldsymbol{\kappa}, \lambda) \end{pmatrix}. \quad (\text{A14})$$

From Eqs. A13 and A14 using Eqs. A11 and A12, we deduce that

$$\begin{aligned} R_1(-\boldsymbol{\kappa}, \lambda) &= R_2(\boldsymbol{\kappa}, \lambda) \\ T_1(-\boldsymbol{\kappa}, \lambda) &= T_2(\boldsymbol{\kappa}, \lambda). \end{aligned} \quad (\text{A15})$$

Finally, using the reciprocity theorem Eqs. A8, A9 and A10, it follows that

$$\begin{aligned} R_1(\boldsymbol{\kappa}, \lambda) &= t(R_2(\boldsymbol{\kappa}, \lambda)) \\ T_1(\boldsymbol{\kappa}, \lambda) &= t(T_1(\boldsymbol{\kappa}, \lambda)) \\ T_2(\boldsymbol{\kappa}, \lambda) &= t(T_2(\boldsymbol{\kappa}, \lambda)). \end{aligned} \quad (\text{A16})$$

B.1.3/ PROPERTIES OF THE EIGENVALUES

Let us now consider the energy transfer transmission and reflection matrices $T_j^*T_j$ and $R_j^*R_j$, with $j = 1$ or 2 . We shall demonstrate that their eigenvalues are unchanged when the polar angle is changed in its opposite. The two eigenvalues for each of the matrices are denoted as $l_k^{T_j^*T_j}$ and $l_k^{R_j^*R_j}$ (with $k = a$ or b), and $V_k^{T_j^*T_j}$ and $V_k^{R_j^*R_j}$ stand for the associated eigenvectors.

The first property comes from the energy balance. Multiplying Eq.A4 (resp. Eq.A5), with $V_k^{T_1^*T_1}$ (resp. $V_k^{T_2^*T_2}$), it is easy to show that

$$\begin{aligned} l_k^{R_1^*R_1} &= 1 - l_k^{T_1^*T_1}, \quad \text{and} \quad V_k^{R_1^*R_1} = V_k^{T_1^*T_1}, \\ (\text{resp. } l_k^{R_2^*R_2} &= 1 - l_k^{T_2^*T_2}, \quad \text{and} \quad V_k^{R_2^*R_2} = V_k^{T_2^*T_2}). \end{aligned} \quad (\text{A17})$$

The second property comes from the reciprocity theorem. Considering a given real $\boldsymbol{\kappa}$, and from the definition of the eigenvalue of $T_1^*(\boldsymbol{\kappa}, \lambda)T_1(\boldsymbol{\kappa}, \lambda)$, we have $T_1^*(\boldsymbol{\kappa}, \lambda)T_1(\boldsymbol{\kappa}, \lambda)V_k^{T_1^*T_1}(\boldsymbol{\kappa}, \lambda) = l_k^{T_1^*T_1}(\boldsymbol{\kappa}, \lambda)V_k^{T_1^*T_1}(\boldsymbol{\kappa}, \lambda)$. Using the relation between $T_1(\boldsymbol{\kappa}, \lambda)$ and $T_2(-\boldsymbol{\kappa}, \lambda)$ coming from the reciprocity theorem (Eq. A8), we obtain

$$\begin{aligned} \overline{T_2(-\boldsymbol{\kappa}, \lambda)}t(T_2(-\boldsymbol{\kappa}, \lambda))V_k^{T_1^*T_1}(\boldsymbol{\kappa}, \lambda) \\ = l_k^{T_1^*T_1}(\boldsymbol{\kappa}, \lambda)V_k^{T_1^*T_1}(\boldsymbol{\kappa}, \lambda). \end{aligned} \quad (\text{A18})$$

Taking the complex conjugate and multiplying the two sides of Eq. A18 with

$T_2^*(-\boldsymbol{\kappa}, \lambda)$, we obtain that

$$\begin{aligned} T_2^*(-\boldsymbol{\kappa}, \lambda)T_2(-\boldsymbol{\kappa}, \lambda)[T_2^*(-\boldsymbol{\kappa}, \lambda)\overline{V_k^{T_1^*T_1}(\boldsymbol{\kappa}, \lambda)}] \\ = \overline{l_k^{T_1^*T_1}(\boldsymbol{\kappa}, \lambda)}[T_2^*(-\boldsymbol{\kappa}, \lambda)\overline{V_k^{T_1^*T_1}(\boldsymbol{\kappa}, \lambda)}]. \end{aligned} \quad (\text{A19})$$

This means that

$$\begin{aligned} l_k^{T_2^*T_2}(-\boldsymbol{\kappa}, \lambda) &= l_k^{T_1^*T_1}(\boldsymbol{\kappa}, \lambda) \quad \text{and} \quad V_k^{T_2^*T_2}(-\boldsymbol{\kappa}, \lambda) \\ &= T_2^*(-\boldsymbol{\kappa}, \lambda)\overline{V_k^{T_1^*T_1}(\boldsymbol{\kappa}, \lambda)}. \end{aligned} \quad (\text{A20})$$

A similar demonstration using the definition of the eigenvalues of $R_j^*(\boldsymbol{\kappa}, \lambda)R_j(\boldsymbol{\kappa}, \lambda)$ (for $j = 1$ or 2) and the Eqs. A9 and A10 leads to

$$\begin{aligned} l_k^{R_j^*R_j}(-\boldsymbol{\kappa}, \lambda) &= l_k^{R_j^*R_j}(\boldsymbol{\kappa}, \lambda) \quad \text{and} \quad V_k^{R_j^*R_j}(-\boldsymbol{\kappa}, \lambda) \\ &= R_j^*(-\boldsymbol{\kappa}, \lambda)\overline{V_k^{R_j^*R_j}(\boldsymbol{\kappa}, \lambda)}, \end{aligned} \quad (\text{A21})$$

for $k = a$ and b (the two eigenvalues), and $j = 1$ or 2 (the two reflectivity matrices).

Finally, applying both the energy balance and the reciprocity theorem, we obtain the following relation for the eigenvalues ($k = a$ or b):

$$l_k^{T_1^*T_1}(\boldsymbol{\kappa}, \lambda) = l_k^{T_2^*T_2}(\boldsymbol{\kappa}, \lambda) = l_k^{T_1^*T_1}(-\boldsymbol{\kappa}, \lambda) = l_k^{T_2^*T_2}(-\boldsymbol{\kappa}, \lambda), \quad (\text{A22})$$

$$l_k^{R_1^*R_1}(\boldsymbol{\kappa}, \lambda) = l_k^{R_2^*R_2}(\boldsymbol{\kappa}, \lambda) = l_k^{R_1^*R_1}(-\boldsymbol{\kappa}, \lambda) = l_k^{R_2^*R_2}(-\boldsymbol{\kappa}, \lambda). \quad (\text{A23})$$

In other words, the energy balance and the reciprocity theorem entail that the two reflectivity (resp. transmittivity) matrices for the energy have the same eigenvalues, and that these eigenvalues are symmetrical with respect to the polar angle of incidence. This last property is the vectorial analog of the property which is well known for 1D blazed gratings illuminated in classical incidence (plane of incidence perpendicular to the grating grooves). Note that the eigenvectors of the reflectivity (resp. transmittivity) matrices for the energy do change when the polar angle is changed in its opposite, which means that in case of polarization conversion, the reflected and transmitted energy are not symmetric with respect to the polar angle of incidence for any state of polarization.

B.1.4/ RESONANT BEHAVIOR OF THE EIGENVALUES

In this paragraph, we shall demonstrate that one eigenvalue of the energy transmittivity matrix $T_1^*T_1$ reaches 100% if the structure has a central symmetry. From now, we consider a configuration for a given real κ where only one eigenmode of the structure can be excited. This means that the equation $\det(S^{-1}(\kappa, \lambda)) = 0$ has one complex solution $\lambda = \lambda_p(\kappa)$ where $\lambda_p(\kappa)$ stands for the dispersion relation of the eigenmode. We introduce the eigenvalues $l_a^{R_1}(\kappa, \lambda)$ and $l_b^{R_1}(\kappa, \lambda)$ and eigenvectors $V_a^{R_1}(\kappa, \lambda)$ and $V_b^{R_1}(\kappa, \lambda)$ of the matrix R_1 . We suppose that only one of the two eigenvalues of R_1 shows a resonant behavior, the other remaining a slowly varying function. We have checked numerically the validity of this hypothesis for the configuration under study. Following the arguments given in ref [154] (end of section 4), for λ in the vicinity of $\lambda_p(\kappa)$ we write the resonant eigenvalue, say $l_a^{R_1}$, as

$$l_a^{R_1}(\kappa, \lambda) = u(\kappa, \lambda) \frac{\lambda - \lambda_z^{R_1}(\kappa)}{\lambda - \lambda_p(\kappa)}, \quad (\text{A24})$$

where $u(\kappa, \lambda)$ is a function with neither roots nor poles, and $\lambda_z^{R_1}(\kappa)$ a complex number. The unicity of the root of $l_a^{R_1}(\kappa, \lambda)$, which is due to the fact that only one mode is excited, is an important property that will be used at the end of the proof.

When $\lambda = \lambda_z^{R_1}(\kappa)$, we obtain that $R_1(\kappa, \lambda_z^{R_1})V_a^{R_1}(\kappa, \lambda_z^{R_1}) = 0$. Introducing this in Eq. A4, where the two sides have been multiplied with $V_a^{R_1}(\kappa, \lambda_z^{R_1})$, we obtain

$$T_1^*(\kappa, \overline{\lambda_z^{R_1}})T_1(\kappa, \lambda_z^{R_1})V_a^{R_1}(\kappa, \lambda_z^{R_1}) = V_a^{R_1}(\kappa, \lambda_z^{R_1}) \quad (\text{A25})$$

which is nothing but the eigenvector equation for $T_1^*T_1$. This means that for $\lambda = \lambda_z^{R_1}(\kappa)$, one eigenvalue of $T_1^*T_1$, say $l_a^{T_1^*T_1}(\kappa, \lambda_z^{R_1})$ is equal to unity. Its eigenvector is $V_a^{T_1^*T_1}(\kappa, \lambda_z^{R_1}) = V_a^{R_1}(\kappa, \lambda_z^{R_1})$. In other words, and not surprisingly, for $\lambda = \lambda_z^{R_1}(\kappa)$, the maximum of transmittivity is obtained when the incident configuration leads to a zero reflected field.

We shall now prove that the symmetry of the structure with respect to a symmetry center entails the fact that $\lambda_z^{R_1}(\kappa)$ is real, meaning that the transmittivity can reach 100% for a real wavelength value. Multiplying the two sides of Eq. A7 with $V_a^{R_1}(\kappa, \lambda_z^{R_1})$ and taking $\lambda = \lambda_z^{R_1}(\kappa)$ leads to

$$R_2^*(\kappa, \overline{\lambda_z^{R_1}})T_1(\kappa, \lambda_z^{R_1})V_a(\kappa, \lambda_z^{R_1}) = 0. \quad (\text{A26})$$

Using Eq. A16, we obtain

$$R_1(\kappa, \lambda_z^{R_1})\overline{T_1}(\kappa, \lambda_z^{R_1})\overline{V_a}(\kappa, \lambda_z^{R_1}) = 0. \quad (\text{A27})$$

As $T_1(\kappa, \lambda_z^{R_1})V_a(\kappa, \lambda_z^{R_1})$ can not be null (otherwise from Eq. A25, $V_a(\kappa, \lambda_z^{R_1})$ would be null),

B.1.

we deduce that $\overline{T_1}(\kappa, \lambda_z^{R_1}) \overline{V_a}(\kappa, \lambda_z^{R_1})$ is the eigenvector of R_1 associated with an eigenvalue which is null for $\lambda = \overline{\lambda_z^{R_1}}$. As $l_a^{R_1}(\kappa, \lambda)$ has only one root and $l_b^{R_1}(\kappa, \lambda)$ has no root, we conclude that $\lambda_z^{R_1}(\kappa)$ is real. Hence, we have shown that there exists one real wavelength for which one eigenvalue of the matrix $T_1^* T_1$ is equal to 100%.

Abstract :

The release of the first report by Faraday in 1857 set the foundation of the production of metal nanoparticles and their unexpected optical properties (coloring). More recently, controlling and guiding light via plasmonic resonance in nanostructures enable a lot of applications affecting everyday life that involves light. Plasmon resonance of metallic structures is a key phenomenon that allows unique optical properties through the interaction of light with the free electrons of the metal. The excitation of Localized Surface Plasmon Resonance (LSPR) leads to turn-on large local enhancements of electromagnetic energy as within antennas or to route light as waveguide to desired region with high transmission through the excitation of Propagating Surface Plasmon (PSP). During this thesis, we have developed an existing algorithm in order to calculate the optical response of NPs of any shape. We have especially determined the localized energy enhancement factor in term of optical response of nano-antenna. This anisotropic (polarization dependent) NPs type can feature, at plasmon resonance, scattering efficiency factor higher than 25. Moreover, an important systematic study has been performed in order to optimize design of such NPs.

Concerning the PSP that are involved in the enhanced transmission through Annular Aperture Arrays (AAAs), we systematically study the properties of the excitation of the peculiar Transverse ElectroMagnetic (TEM) guided mode inside such nano-apertures. A complete numerical study is performed to correctly design the structure before it is experimentally characterized. For reasons associated to fabrication constraints and efficiency, a slanted AAA made in perfectly conducting metal is proposed and studied. We numerically and analytically demonstrate some intrinsic properties of the structure showing a transmission coefficient of at least 50% of an un-polarized incident beam independently of the illumination configuration (polarization, angle, and plane of incidence). At the TEM peak transmission, the laminar flow of the energy through the structure can exhibit giant deviation over very small distances ($< \lambda$). The results presented in this thesis could be considered as an important contribution to the understanding of the enhanced transmission phenomenon based on the excitation of guided modes.

Keywords: Localized surface plasmon, Optical nanoantenna, Propagating surface plasmons, Waveguides, Enhanced transmission, Metamaterials.

Résumé :

L'intérêt des nano-particules pour le domaine de l'optique visible a été suscité lors du premier rapport rédigé par Faraday en 1857 et qui a initié les bases de la production de nanoparticules métalliques en vue de leur propriété optiques inattendues (coloration des solutions). Plus récemment, le contrôle et le guidage de la lumière basés sur l'excitation de résonance plasmon dans les nanostructures a permis beaucoup d'applications liées à la vie quotidienne et impliquant la lumière. La résonance plasmonique de structures métalliques est un phénomène essentiel qui conduit à des propriétés optiques uniques à travers l'interaction de la lumière avec les électrons libres du métal. L'excitation de la résonance plasmon localisé (LSPR) permet d'exalter localement l'énergie électromagnétique comme dans le cas des nano-antennes mais aussi d'acheminer la lumière à travers des canaux de dimensions $\text{sub-}\lambda$ sur de grandes distances grâce à l'excitation du Plasmon de Surface Propagatif (PSP). Au cours de cette thèse, nous avons étendu un algorithme existant afin de calculer la réponse optique (sections efficaces de diffusion et d'absorption) de NPs ayant une forme géométrie quelconque. Ce type de NP anisotrope (vis-à-vis de la polarisation incidente) peut présenter à la résonance plasmonique une section efficace de diffusion 25 fois supérieure à celle géométrique. De plus, une étude systématique importante a été effectuée afin d'optimiser la géométrie de tels Nps.

En ce qui concerne la PSP qui est impliqué dans la transmission exaltée à travers les matrices d'ouvertures annulaires AAA, nous avons entrepris une étude systématique des propriétés de l'excitation du mode particulier sans coupure de ces nano - guides. Il s'agit du mode Transverse Electrique et Magnétique (TEM). Une étude numérique complète est alors effectuée pour correctement concevoir la structure avant qu'elle ne soit expérimentalement fabriquée et caractérisée. Pour palier certaines contraintes expérimentale, une structure inclinée est proposée et étudiée dans le cas d'un métal parfaitement conducteur. Nous avons démontrée numériquement et analytiquement certaines propriétés intrinsèques de la structure montrant un coefficient de d'au moins 50% d'un faisceau incident non polarisé indépendamment des conditions d'éclairage (polarisation, angle et plan d'incidence). Lorsque le mode TEM est excité, le flux laminaire de l'énergie à travers la structure présente une déviation géante sur de très petites distances inférieures à la longueur d'onde. Les résultats présentés dans cette thèse pourraient être considérés comme une contribution importante à la compréhension du phénomène de transmission exaltée basé sur l'excitation de ce type de mode guidé.

Mots-clés : Plasmon de surface localisée, Nanoantenne optique, Plasmon de surface localisés, Guides d'onde, Transmission exaltée, Métamatériaux.

The logo for SPIM (École doctorale SPIM) features a stylized white 'S' on a yellow background, followed by the letters 'PIM' in a large, white, sans-serif font.